DEPARTMENT OF THE AIR FORCE
AIR UNIVERSITY
AIR FORCE INSTITUTE OF TECHNOLOGY

Wright-Patterson Air Force Base, Ohio

AFIT/GSO/ENP/96D-02

ESTIMATION OF SATELLITE ORIENTATION
FROM SPACE SURVEILLANCE IMAGERY
MEASURED WITH AN
ADAPTIVE OPTICS TELESCOPE

THESIS
Gregory E. Wood
Lieutenant, USAF

AFIT/GSO/ENP/96D-02

19970210 036

Approved for public release; distribution unlimited

ESTIMATION OF SATELLITE ORIENTATION FROM SPACE SURVEILLANCE IMAGERY MEASURED WITH AN ADAPTIVE OPTICS TELESCOPE

THESIS

Presented to the Faculty of the School of Engineering

of the Air Force Institute of Technology

Air University

In Partial Fulfillment of the

Requirements for the Degree of

Master of Science

Gregory E. Wood, B.S.

Lieutenant, USAF

December, 1996

Acknowledgements

I would like to express my appreciation to my research sponsor, Phillips Laboratory OL-YY, for allowing my involvement in this research. This applies equally to Major Michael Roggemann, Ph.D., my thesis advisor, for his guidance. This thesis is representative to his efforts to guide a student with a minimal optics background and raise him to a level where it was possible to conduct meaningful research. I am also indebted to Dr. Byron Welsh whose involvement as a committee member was essential to the success of these efforts. I am grateful to both Major Roggemann and Dr. Welsh for their "hands off" approach as advisors. Unlike many of my peers I was allowed to pursue this research effort in my own manner and was given the freedom to experiment with different approaches. They were always there, however, when I ran up against the inevitable "brick wall". Even more importantly than what I learned about adaptive optics, they taught me how to think.

Several of my peers also need to be recognized here. Captain David Gill from the National Air Intelligence Center, AFIT class GSO 94D, was instrumental to the success of this project. He openly gave his time and assistance in providing the satellite models used in this project. I would also like to thank the other members of my class, GSO 96D, for their sincere interest in this project and support throughout our experiences at AFIT. A special thanks goes to Captain Scott Maethner for sharing all of those late nights and non-existent weekends and holidays. Without our marathon study sessions, very little of what I achieved at AFIT could have been accomplished.

Above all, I wish to express the utmost in thanks to my wife, Gina, for her support throughout this research and the rest of my work at AFIT. Without her patience and understanding, none of this work would have been possible.

Gregory E. Wood

ii

Table of Contents

iv

List of Figures

List of Tables

AFIT/GSO/ENP/96D-02

Abstract

The use of the matched filter to automatically estimate the pose of a Low Earth Orbiting satellite from imagery taken with an adaptive optics telescope is explored. This work represents the first effort to solve the satellite pose estimation problem while considering the broad range of atmospheric turbulence levels and target visual magnitudes that are encountered in ground based space surveillance operations. Several algorithms are examined in an effort to determine the performance bounds on the matched filter for this application. Results are given over an extremely wide range of seeing conditions. These results are weighted based on historical data obtained from the Air Force Maui Optical Station (AMOS) to show that, under normal imaging conditions, the matched filter approach proposed in this thesis can be expected to yield correct pose estimations in over eighty percent of the trials considered. Additionally, it is shown that a significant portion of errors are between two poses that are very similar in appearance, such as views of the target about an axis of symmetry. A correlation value is defined such that a value between 0.0 and 1.0 is assigned for each trial. This correlation value is a quantitative measure of the similarity between the predicted pose and the actual pose being imaged, with a value of 1.0 being representative of a correct pose estimation. When weighted according to actual seeing conditions, the algorithm developed in this study provides an average correlation value in excess of 0.98. A dependable algorithm is defined that will function efficiently under a wide range of seeing conditions that are encountered in ground based space surveillance operations.

ESTIMATION OF SATELLITE ORIENTATION FROM SPACE SURVEILLANCE IMAGERY MEASURED WITH AN ADAPTIVE OPTICS TELESCOPE

I. Introduction

1.1 Motivation

The motivation for this research is to solve a practical problem in space operations by combining the science of remote sensing with the techniques of Fourier optics. There are several potential uses for a simple, reliable method to estimate the pose of an orbiting satellite. Throughout this thesis, the term "pose" refers to the three dimensional orientation of an orbiting satellite. Primarily, however, this could be a useful tool in determining the attitude of a satellite if regular telemetry data is not available due to a satellite malfunction or when imaging foreign spacecraft.

For instance, a satellite may not properly deploy once its booster has placed it into orbit. This was the case with AeroAstro Corporation's Alexis program in 1993(28). A Pegasus booster placed the satellite into orbit. However, one of the solar panels did not properly deploy. A critical piece of the attitude determination subsystem was located on the axis of that panel. As a result, the satellite was never able to place itself in proper alignment with the sun. Because it was not able to generate power, the satellite entered a safe mode. The payload was unharmed and would have functioned if it was possible to align the solar panels, but ground controllers were unable to determine the satellite's pose. If this data had been available, the situation could have been quickly corrected from the ground. Instead, ground teams were forced to wait nearly two months before they could evaluate what had gone wrong with the satellite. Using small bursts of data that were transmitted from

1

the vehicle as its solar cells occasionally aligned with the sun long enough to provide a partial charge to the batteries, ground teams were eventually able to determine the satellite's pose. Once this was accomplished, the satellite was repositioned and became fully operational. However, two months of scientific data was lost.

1.2 Background

Ground based telescopes can be used to assess payloads, missions, and threats of orbiting satellites. Limitations due to the physics of orbital mechanics prohibit gathering this type of data in a timely manner from space based platforms (5:169). The required orbital plane changes are very expensive in terms of the limited fuel supply on an orbiting satellite (13:148).

There are, however, several complications associated with the imaging of earth orbiting objects from ground based observatories (23). Atmospheric turbulence dramatically decreases the resolution that can be achieved. Differential heating of large segments of the earth's surface yields an inhomogeneous temperature distribution within the air. This causes the air to move and dissipate heat into smaller turbulent eddies. Each of these turbulent eddies has its own temperature distribution which causes changes in the index of refraction. This results in random spatial and temporal distributions of the index of refraction. Hence, light received from the target satellite at the telescope is retarded at different rates, yielding a blurred image. The resolution of even the largest uncompensated telescopes is limited by atmospheric effects to a much greater extent than by the telescope diameter (22:451). This study utilizes a simulated adaptive optics (AO) telescope to partially compensate for atmospheric turbulence effects.

Light collected by a telescope from the satellite being imaged, referred to throughout this thesis as the target, can only be a combination of reflected sunlight and emitted blackbody radiation. As a result, the objects are extremely dim. Additionally, the satellite must be in terminator mode, where the target is illumi-

2

nated by the sun and the observatory is in darkness. Typical low earth orbiting satellites have maximum linear dimensions on the order of two to ten meters and orbital altitudes of 200 to 750 kilometers (13:337). It is rare for a satellite to pass directly over a ground based observatory. As a result, slant ranges can be much greater. Current limitations due to aperture size and radiometric throughput limit the slant range at which useful observations can be made to about 1000 kilometers (23). Beyond this range the detection of satellites is possible, but the image resolution is poor. The combined effect of the low light levels, slant range, target size, and atmospheric turbulence make it extremely difficult to gather high quality imaging data.

A typical target for ground based space surveillance operations is a satellite which is, in its most elementary form, a collection of rectangular and cylindrical components. For passive thermal control, most satellites are designed with a highly reflective coating, such as Optical Solar Reflectors (OSR's) or silver coated Teflon (13:428). Some sunlight will almost always be reflected toward the observatory. Large, dark surfaces such as solar panels, however, might be completely invisible to a ground observer depending upon the satellite's orientation with respect to the sun. This combination of structures and materials results in a unique image pattern for each observed pose of a satellite.

Because of this, the problem of satellite pose estimation is closely related to the field of pattern recognition (11:246). The matched filter has been used successfully in many applications in this field. The pose estimation problem is very similar to that of pattern recognition, with one exception. Even with the use of adaptive optics to partially compensate for turbulence in real time, the images received are aberrated due to atmospheric turbulence. This turbulence tends to blur the images, making the problem of pose estimation quite difficult. Research done in this field has been minimal due to the lack of a database of accurate representations of satellites

imaged through atmospheric turbulence with photon noise considerations taken into account.

1.3 Current Knowledge

The problem of pose estimation has been of interest in the fields of machine vision and robotics for several years. Most of this research has been based on the use of geometric, CAD models of objects. Cyganski (7:17) asserts that nearly all current pose estimation routines are based on the idea of searching a large database of images and determining which has the greatest correlation with the unknown target image. In most cases, a sum of squared difference methodology is used to determine the required correlation values. This is especially common in machine vision for template matching, establishing correspondence in binocular stereo, and feature tracking in motion estimation (19:12).

Murase and Nayer acknowledged that the appearance of an object is the combined effect of its shape, reflectance properties, pose in the scene, and illumination conditions (19:6). Their study of "appearance matching" rather than shape matching in the pose estimation problem is unique in that it is the first work that takes into account lighting conditions as a variable in the problem. Previously, some effort had been invested in using the Karhunen-Louve technique utilizing the eigenvectors associated with an image to determine the correlation between images with Principle Component Analysis (PCA) algorithms. PCA techniques have been successfully applied to pose estimation problems involving written character recognition and human face recognition. Murase and Nayer successfully applied these PCA techniques to determine the pose of three dimensional objects imaged under different lighting conditions (19:8)

The work of Murase and Nayer, however, deviates from the problem at hand because their pose estimation routine does not account for the adverse effects of atmospheric turbulence. In July 1995, Chang and Hoepner from the Texas Instruments

4

Incorporated Defense Systems & Electronics Group issued a status report which outlined a technique for satellite pose estimation (6). This pose estimation routine is based almost entirely on a method proposed by Cyganski (7:17). Cyganski's method deviates from the more customary database search. It involves the use of an object model composed of a set of basis images. The basis images are developed in a manner such that the projection of an acquired image onto the basis yields samples of a complex exponential plane wave. The direction cosines of the plane wave act as a transformation between the object and the model. Direction of Arrival (DOA) techniques are applied to estimate the target's pose.

Unlike Murase and Nayer, the Texas Instruments study does not consider the effects of lighting conditions on pose estimation. Their effort is, however, the first to address atmospheric turbulence as a variable in a pose estimation algorithm. The report discusses the fact that the imagery they were provided was blurred due to turbulence, without discussion of the turbulence levels considered or their overall effect on the pose estimation algorithm (6:4). Additionally, the report states that their algorithm takes advantage of "the low noise inherent in satellite imagery" (6:4). In Chapter II of this thesis, the signal to noise ratio is shown to be proportional to the square root of the photon flux. This implies that the Texas Instruments study considered imagery at relatively high light levels.

1.4 Problem Statement

This thesis investigates the utility of the use of a matched filter algorithm to estimate the pose of Low Earth Orbiting (LEO) satellites through varying levels of atmospheric turbulence and light levels from partially compensated adaptive optics imagery. It investigates several derivatives of the matched filter to determine the bounds on their application. By performing this study over a known range of seeing conditions, a pose estimation algorithm is defined that has a high utility in the operational environment. Because this thesis represents the first major effort to

5

include the effects of target lighting conditions and atmospheric turbulence levels, it establishes a benchmark in performance against which future studies can be weighed.

1.5 Research Objectives

The objectives of this thesis effort were as follows:

- Develop a database that can be made available to fellow researchers consisting of multiple unclassified views of three different satellite systems as seen through an adaptive optics telescope under a series of atmospheric turbulence conditions and light levels.

- Study the utility of using the matched filter for addressing the satellite pose estimation problem.

- Examine several derivatives of the basic matched filter to determine which is the most useful in the pose estimation problem over the wide range of seeing conditions normally encountered in ground based space imaging.

- Determine the limits of the matched filter for this application, thus providing a benchmark for future research efforts that pursue other approaches to the pose estimation problem.

1.6 Approach

These objectives were attained using a systematic approach. First, a set of images of satellite models at known poses was generated. From these, a database of accurate representations of the satellites at these poses under various atmospheric turbulence and lighting conditions through an adaptive optics telescope was created using AO simulation software. The matched filter, and its derivatives, were applied to these simulated target images using a database of known images as a reference. These tests were repeated at several light conditions and atmospheric turbulence levels. Finally, the results of these tests were used to quantify the effectiveness of

6

the different matched filter algorithms and determine the bounds on their use for pose estimation.

1.7 Scope

This thesis is intended to provide a benchmark for future work in this area. It evaluates several matched filter algorithms for their utility in the pose estimation problem. By examining several derivatives of the basic matched filter, this thesis determines the algorithm with the highest likelihood of correct pose estimation over a variety of light levels and atmospheric turbulence levels. In doing this, the practical bounds on the application of the matched filter to the pose estimation problem are defined.

Unlike more traditional pose estimation research efforts, this thesis does not focus on the precision of the pose estimation that can be achieved under one specific set of seeing conditions. Precision on the order of one degree is advertised by algorithms such as that proposed by Chang and Hoepner (6:19). For most practical applications, such as determining if a satellite is being maneuvered to a new orbital plane, this type of precision may not be necessary. Plane changes are usually performed as a series of several maneuvers to conserve fuel. As a result, plane changes occur over a period of several orbits, with successive passes over a ground station showing significant changes in attitude (13:149).

Instead, this thesis focuses on the development of a pose estimation algorithm that is effective over the wide range of seeing conditions that are normally encountered during ground based space surveillance operations. The precision that is possible is not explicitly explored in this research. It is hypothesized that this will be a function of the seeing conditions under which imagery is attained. At the early stages of development of the pose estimation algorithm presented here, it was deemed more important to be able to operate under a wide range of conditions. Future research

can be dedicated to examining and possibly improving the precision that can be attained by using the algorithm developed in this study.

1.8 Key Results

This thesis shows that the matched filter can be successfully applied to the satellite pose estimation problem. Of the algorithms considered in this study, the best results are achieved by utilizing deconvolution techniques followed by the application of a Sobel edge map before applying the target image to the matched filter.

Results are given over an extremely wide range of seeing conditions. These results are weighted based on historical data obtained from the Air Force Maui Optical Station (AMOS) to show that, under normal imaging conditions, the matched filter approach described above can be expected to yield correct pose estimations in over eighty percent of the trials considered in this thesis. Additionally, it is shown that a significant portion of errors are between two poses that are very similar in appearance, such as views of the target about an axis of symmetry. A correlation value is defined such that a value between 0.0 and 1.0 is assigned for each trial. This correlation value is a quantitative measure of the similarity between the predicted pose and the actual pose being imaged, with a value of 1.0 being representative of a correct pose estimation. When weighted according to the actual occurrence rates of the seeing conditions, the algorithm developed in this study provides an average correlation value in excess of 0.98.

Atmospheric turbulence is shown to be a contributor to the degradation of the matched filter approach. However, the utility of the matched filter is shown to be more highly dependent upon the light level associated with the target image.

1.9 Thesis Organization

This thesis is organized in the following manner: Chapter II discusses the theory pertinent to this problem, including the effects of atmospheric turbulence

and photon noise as they pertain to AO imagery. Additionally Chapter II discusses the theory of the matched filter as well as some of the post processing techniques that may be applied to improve the quality of the AO imagery before applying the matched filter. Chapter III outlines the methodology used in this research. The observations and data analysis are presented in Chapter IV. Conclusions drawn from this study and recommendations for further research are discussed in Chapter V.

1.10 Summary

In order to assess the utility of the application of the matched filter to the satellite pose estimation problem, a series of test images are created under multiple seeing conditions for an adaptive optics telescope. The basic matched filter, and several derivatives, are applied to these images both with and without postprocessing techniques to determine the pose of the satellite from a database of known images. This thesis determines the most reliable matched filter algorithm for this problem across a wide range of seeing conditions and define the bounds for its practical application.

II. Theory

In Chapter I, the problem of satellite pose estimation using an adaptive optics telescope was clearly defined. The approach taken for this problem is based on the concept of the matched filter. This research represents an extension of the theory behind the use of the matched filter for pattern recognition. The effect of noise on matched filter performance is not generally treated in textbooks on this subject. However, the matched filter cannot be applied to the satellite pose estimation problem without a firm understanding of noise and atmospheric effects on the target image. This chapter introduces the key concepts needed to understand these effects. It describes the matched filter and its application in pattern recognition. The theory behind this research effort is represented by the union of the studies of pattern recognition and imaging through atmospheric turbulence.

2.1   The Concept of the Matched Filter

Originally, the matched filter was used as a means of signal detection. The filtering process usually involves searching through the received signal to find an approximate match to one of many known signals. In order to detect a known signal obscured by white noise, the matched filter provides a linear operation to maximize the power signal to noise ratio (11:246). The one dimensional matched filter is widely used in signal detection applications such as radar and digital communications (20:653).

A two dimensional matched filter can be applied to image processing. The most recent uses for the matched filter lie in the field of pattern recognition. In this field, the input patterns are assumed to be noiseless. The matched filter is used to determine if a particular pattern is present in an input signal.

A matched filter is a spatial filter that provides a measure of the level of correlation between an input image and a known image. By sequentially measuring

the correlation between an input image and a database of known images, it is possible to classify the input properly.

A linear shift invariant (LSI) system is matched to an unknown signal $s(x,y)$ when its impulse response, $h(x,y)$, is given by (11:246)

$$h(x,y) = s^*(-x,-y). \tag{1}$$

The asterisk represents the complex conjugate of the function. For a given input, $g(x,y)$, the output is given by (11:246)

$$v(x,y) = \iint_{-\infty}^{\infty} g(\xi,\eta)s^*(\xi-x,\eta-y)d\xi d\eta. \tag{2}$$

This function is the cross correlation between $g(x,y)$ and $s(x,y)$.

2.1.1   Use of the Matched Filter for Character Recognition.   For the pattern recognition problem, the input $g(x,y)$ is compared to a database of N possible patterns. These patterns are denoted by s_1, s_2, s_3,...s_N. Pratt (20) discusses an important limitation of the matched filter in pattern recognition. Often, the correlation determined by the matched filter is highly dependent upon the relative energies of the target image and the known image. Both the input signal and the set of possible patterns must be energy normalized in order to account for this energy dependency. For any image, $g(x,y)$, this energy normalization is accomplished by

$$g'(x,y) = \frac{g(x,y)}{\sqrt{\int\int |g(x,y)|^2 dx dy}}. \tag{3}$$

The energy normalized input signal is sequentially applied to the filters S_1^*, S_2^*, S_3^*,...S_N^*, which correspond to the N possible patterns. In this document, S_i represents the Fourier transform of the pattern defined spatially by s_i. The largest

output represents the highest correlation with the input image. The use of the basic matched filter for pattern recognition is described in Figure 1 (11:248).

Outputs

$$\frac{g(x,y)}{\sqrt{\int\int |g(x,y)|^2 d\xi d\eta}}$$

Input

s_1^* ÷ v_1

$\sqrt{\int\int |s_1|^2 d\xi d\eta}$

s_2^* ÷ v_2

$\sqrt{\int\int |s_2|^2 d\xi d\eta}$

s_k^* ÷ v_k

$\sqrt{\int\int |s_k|^2 d\xi d\eta}$

s_N^* ÷ v_N

$\sqrt{\int\int |s_N|^2 d\xi d\eta}$
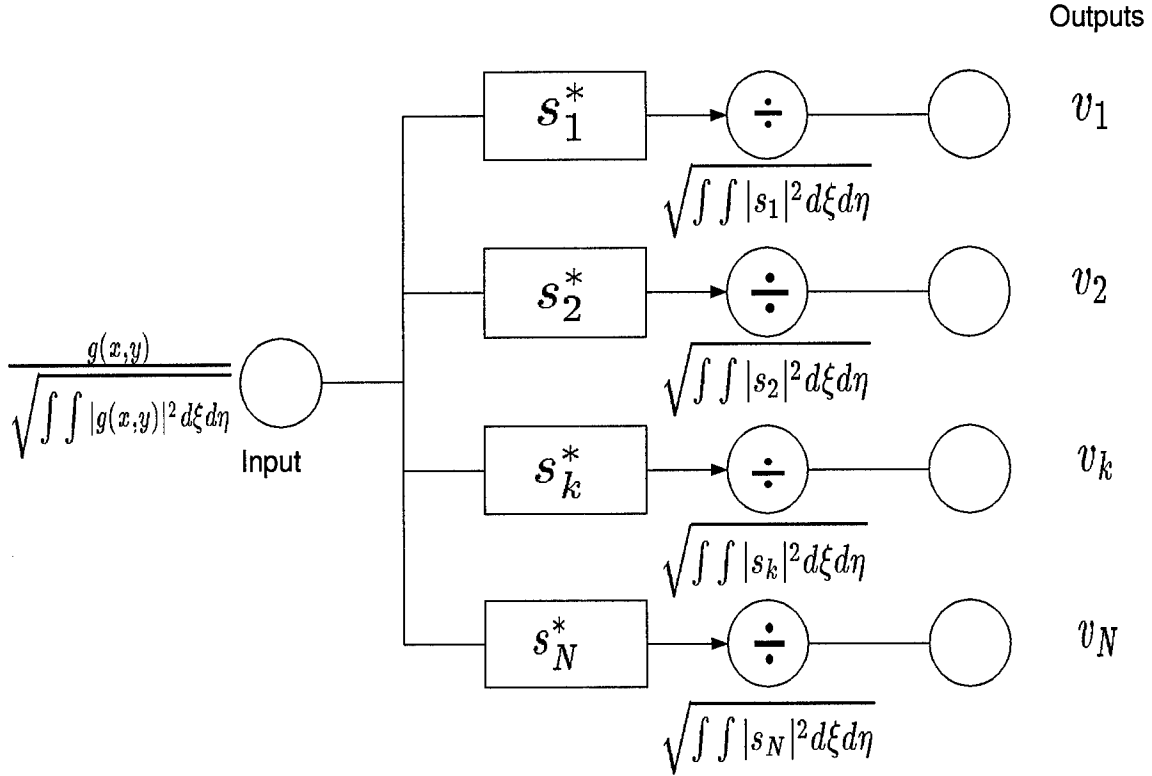
Figure 1. Block Diagram Representation of the Matched Filter as Applied to the Pattern Recognition Problem

2.1.1.1 Justification of the Choice of Using a Matched Filter for Satellite Pose Estimation.   A common method for comparing images in the spatial domain is to measure the difference between them using a normalized mean-square error method (20:685). This is the basis for template matching techniques described by Pratt (20:651). The normalized mean square error technique is described mathematically by Equation 4.

$$\varepsilon_{NMSE} = \frac{|F(j,k) - \hat{F}(j,k)|^2}{|F(j,k)|^2} \tag{4}$$

$F(j,k)$ and $\hat{F}(j,k)$ represent two images to be compared.

From Equation 4, it is apparent that this is a pixel by pixel determination of the difference between the two images. This requires both images to be of the same scale size and be centered at the same point in the pixel array. From an operational point of view, the scaling can be accounted for by methods described in Section 2.1.2.3. However, the location of the target within the image plane is extremely difficult to control given that the target is not stationary when imaging LEO satellites (15:1-2). As a result, pixel by pixel differencing is not a feasible alternative.

Pratt (20:656) demonstrates a key property of the matched filter which makes it ideally suited for image classification from remotely sensed data. The matched filter is shift invariant. Under ordinary circumstances, the matched filter is defined such that the origin of the output plane becomes the point of no translational offset between the known reference signal and the input signal.

For the case where the target image consists of an object from the known image database, offset by distances Δx and Δy, it is described by a modified input function of the form

$$g(x, y) = s(x + \Delta x, y + \Delta y). \tag{5}$$

The output of the matched filter for this target/reference pair is given by

$$v(x, y) = \int\int_{-\infty}^{\infty} g(\xi + \Delta x, \eta + \Delta y)s^*(\xi - x, \eta - y)d\xi d\eta. \tag{6}$$

From this, a correlation peak occurs when $x = \Delta x$ and $y = \Delta y$ in the output plane (20:656). This indicates the translation of the input image relative to the reference image.

For the study of satellite pose estimation from space surveillance imagery, the magnitude of this shift is not important. It is merely the result of the pointing accuracy of the imaging device. The shift invariance is, however, the key benefit gained from the application of the matched filter to this problem. The translation invariance of the matched filter makes it ideally suited for this application.

2.1.2 Deficiencies of the Matched Filter Approach for Pattern Recognition.
Energy dependency is one of three key deficiencies that are encountered when applying the matched filter to the classical pattern recognition problem. Goodman (11:251) demonstrates that the matched filter is also extremely sensitive to both rotation and scale size.

2.1.2.1 Sensitivity to Energy Content. As mentioned in Section 2.1.1, Pratt points out that the matched filter can be inefficient at discriminating between objects of similar size, but with different energy content and shape. In his text, he provides the example of a white hexagon and a white circle, both on a black background. Even after energy normalizing both signals, he asserts that the normal matched filter may not be able to reliably distinguish between the two. The proposed solution to this problem is the use of a variation of the basic matched filter. Basically, this consists of utilizing an edge enhancement routine before applying the matched filter.

In 1970, Sobel introduced one of the most widely utilized edge enhancement techniques (25:125). Sobel's approach draws from the Roberts Cross operator that was introduced in 1965. The Sobel operator is based upon the gradient operation defined by Equation 7.

$$grad(f) = \frac{\partial f}{\partial x}\hat{x} + \frac{\partial f}{\partial y}\hat{y} \qquad (7)$$

The value of the modulus of the gradient, $|grad(f)|$, is locally maximized at edges in the image. Therefore, by establishing an appropriate tolerance value, it is possible to use the Sobel technique to define the edges while masking all other features in an image. The Sobel operator is especially well suited for the pose estimation problem because its edge enhancing capabilities are not direction dependent. The application of the Sobel edge map to the target image and known image before applying the matched filter will greatly improve the results that can be obtained in the noiseless pattern recognition problem (20).

-1	0	1		-1	-2	-1
-2	0	2		0	0	0
-1	0	1		1	2	1

Figure 2. Sobel Operator Masks

m1	m2	m3
m4	m5	m6
m7	m8	m9

Figure 3. Generalized Spatial Filtering Mask

In practice, the Sobel operation can be thought of in terms of sequentially sliding two 3 × 3 pixel masks over the image. These masks are defined by Figure 2 (15:2-16). A generalized form of a spatial filtering mask is defined in Figure 3. If this mask is applied to a set of pixels within an image, $p_1, p_2, \ldots, p_9$, the center pixel is replaced according to Equation 8 (15:2-15).

$$p_{5,new} = \sum_{n=1}^{9} (m_n \times p_n) \tag{8}$$

The results of this thesis are based on the Sobel edge map routine that is built into the MATLAB Image Processing Toolbox (26).

The difficulty in discrimination between two similar objects as described in the circle-hexagon example above is of vital importance in the satellite pose estimation problem. In images against the black background of space, the highly reflective surfaces of a satellite can be very similar to the idealized white geometric shapes in Pratt's example. Many satellites share similar features such as cylindrical bod-

ies and large, rectangular solar panels. Additionally, there are size limitations on satellite design that are imposed by the shroud size of the particular booster used in the launch segment of the mission (13:674). The maximum linear dimension of most satellites is on the order of two to ten meters. This, combined with the symmetry inherent in many satellite designs, can result in exactly the same kind of complications encountered in Pratt's example.

It is worth noting that research is ongoing in the arena of edge detection. Law, Ito, and Seki have noted that edges are often distorted in imagery, making fundamental algorithms, such as that of Sobel, difficult to apply. In real world applications they assert that edges may be (14:483):

- Gradual in transition

- Between areas of non-uniform intensity

- Between areas of similar intensity

- Noisy

- Any combination of the above

For strong deviations from the ideal case, they propose using "fuzzy reasoning" techniques to mimic the edge detection capability of the human "eye-brain" system (14:482).

Additionally, Qian and Huang have proposed an edge detection scheme based on a Laplacian of Gaussian methodology (12:1215). They show their algorithm to be optimal in terms of both signal to noise ratio (SNR) and edge localization accuracy. The advantage of their technique is that it detects edges based on edge segments rather than edge points. This significantly reduces the effects of random noise on the results (14:1220).

For this study, only the Sobel edge map is utilized. This thesis is intended to represent a baseline study with easily reproducible results. The Sobel edge map is a time proven method that is easily implemented.

2.1.2.2 Sensitivity to Rotation of the Input. The rotational sensitivity of the matched filter is an important consideration in the pattern recognition field. When the input image is rotated, its response to the correct matched filter is greatly reduced. The degree of error due to rotation is largely dependent upon the structure of the target. As an example, the rotation of the letter "O" has a much less significant effect on a matched filter routine than a similar rotation of the letter "E". (20)

This rotation sensitivity is the key to the matched filter that is exploited in this thesis to solve the satellite pose estimation problem. The target's relative position to the observatory affects its apparent pose. The apparent pose is a result of the dynamics involved in the satellite's orbit and the kinematics defining its orientation relative to a non-rotating coordinate system with its origin at the satellite's center of mass. The ultimate goal of the pose estimation algorithm is to be able to determine the target's orientation with respect to some predefined, fixed coordinate system. For this reason, an algorithm must be developed to automatically relate the apparent pose as viewed from the observatory to the pose as it would be viewed from this fixed reference point. This requires a technique to separate the dynamic and kinematic components of the apparent pose as measured from the observatory. A comprehensive summary of the mathematics describing the motion of a satellite with respect to a ground station is provided in the Larson and Wertz text (13:114). For this study, it is assumed that this algorithm exists and is transparent to the user. This thesis focuses on the determination of the apparent pose as measured by the ground based observatory.

2.1.2.3 Sensitivity to Scale Size. The scale size sensitivity of the matched filter must be considered when applying it to the pose estimation problem. For a given telescope with fixed imaging parameters, the scale of the image is a function of the slant range to the target. This distance can be calculated from the satellite's ephemeris data and the geographic coordinates of the observatory (13:114).

Two major options exist that may be used to minimize the effects of scale sensitivity to the matched filter.

Goodman discusses the Mellin transform and its use for overcoming the scale sensitivity of the matched filter (11:252). The Mellin transform is described mathematically by

$$M(s) = \int_0^\infty g(\xi)\xi^{s-1}d\xi, \tag{9}$$

where s is a complex variable. If s is restricted to be given by $s = j2\pi f$, a basic relationship between the Fourier transform and the Mellin transform is given by

$$M(j2\pi f) = \int_{-\infty}^\infty g(e^{-x})e^{-j2\pi fx}dx. \tag{10}$$

This is clearly analogous to the one dimensional Fourier transform for a function $g(x)$ which is given by Equation 11 (9:111).

$$F(g(x)) = \int_{-\infty}^\infty g(x)e^{-j2\pi fx}dx \tag{11}$$

According to Goodman, the magnitude of the Mellin transform can be shown to be scale invariant (11:253). This, along with the fact that the Mellin transform can be performed as the Fourier transform of a stretched input, makes it an option for avoiding the sensitivity of the matched filter to scale size.

Computationally, the Mellin transform is more difficult than using the Fast Fourier Transform associated with the more conventional matched filter. Because there is very little existing data on the satellite pose estimation problem, it was decided that the simplest feasible method should be studied in order to provide a baseline for future studies. As a result, the Mellin transform method is beyond the scope of this thesis.

An alternative technique is to develop a large database of known images in different poses and with different scale factors. This approach allows for the direct

implementation of the computationally efficient Fast Fourier Transform (FFT) algorithm. For a given satellite, a database can easily be created using the telescope parameters and a range of possible slant ranges to the target. The actual slant range to a target can be determined from the ephemeris data. With this information, the appropriate subset of the target's matched filter database can be selected for testing in the pose estimation algorithm. The test cases examined in this thesis all assumed a 500 kilometer slant range and are representative of one such subset of this database.

2.2 Noise Considerations

The previous section provides insight into the deficiencies that are specific to the matched filter. Noise is inherent in any imaging system and must also be considered when using the matched filter for this application.

In its simplest form, the image of the target, $i(x, y)$, is described by

$$i(x, y) = \iint_{-\infty}^{\infty} o(\xi, \eta) s(x - \xi, y - \eta) d\xi d\eta, \tag{12}$$

where $o(\xi, \eta)$ and $s(\xi, \eta)$ represent the object and point spread function, respectively. By taking the Fourier transform of both sides of Equation 12, we obtain the spatial frequency domain representation given by

$$I(f_x, f_y) = S(f_x, f_y) O(f_x, f_y). \tag{13}$$

Using the frequency representation, the spectrum of the original object would be given by Equation 14 in the absence of noise.

$$\hat{O}(f_x, f_y) = \frac{I(f_x, f_y)}{S(f_x, f_y)} \tag{14}$$

This is clearly the same as passing the received image through a linear shift invariant filter of the form

$$H(f_x, f_y) = \frac{1}{S(f_x, f_y)}. \tag{15}$$

This rather simple filter is known as the inverse filter. The inverse filter, however, demonstrates a fundamental problem associated with signal processing. It fails to account for the fact that any received signal is inherently noisy. The inverse filter will actually tend to boost the effects from parts of the image with a low signal to noise ratio (SNR). The result is an output signal that is dominated by noise.

$S(f_x, f_y)$ represents the Optical Transfer Function (OTF). The OTF is essentially a low pass filter that attenuates the higher frequency components in the received signal. It should be noted that the OTF is a time dependent random variable in the problem of imaging through atmospheric turbulence (27:1-2). Because information about the edges of the target is contained in the high spatial frequencies, the image is inherently blurred. Ideally, it would be possible to use the inverse filter described above to remove these effects. However, frequencies associated with points where the OTF is zero are forever lost. This includes all frequencies above the OTF cutoff frequency. Additionally there exists an upper frequency limit due to noise amplification where the OTF correction begins to degrade the image. To minimize the effects of noise amplification, it is possible to modify the inverse OTF. By attenuating some of the higher spatial frequencies, some of the noise effects can be suppressed. However, since edge information is contained in the higher spatial frequencies, some of the image details are lost.

One common technique for overcoming these noise effects is to pass the output of the inverse filter through an additional filtering step (21:158). The new representation of the filter is shown by

$$O'(f) = \hat{O}(f) \cdot H'(f). \tag{16}$$

20
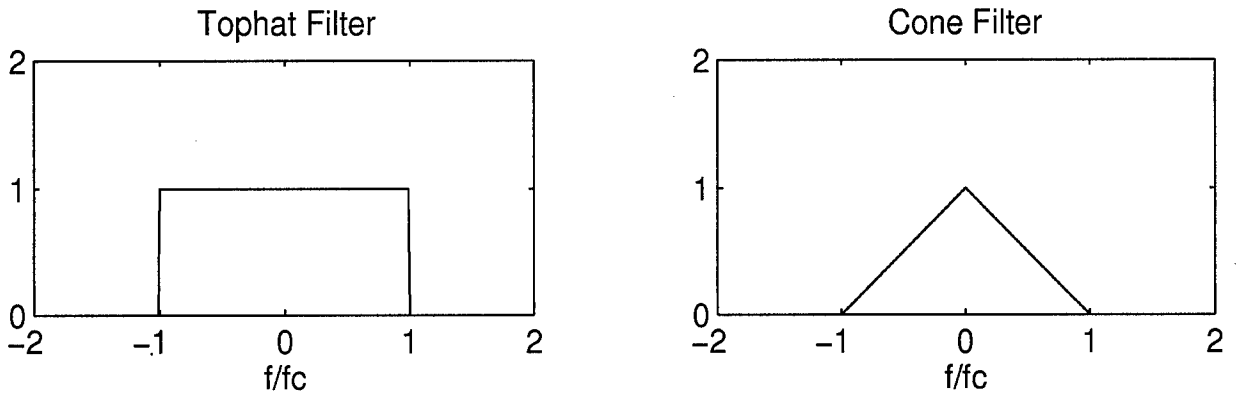
Figure 4. Basic Tophat and Cone Filters

Two commonly used forms for this filter are the cone filter and the tophat filter. The cone filter is defined by

$$H'_{cone}(f) = \begin{cases} 1 - |f|/f_c, & \text{if } |f| \leq f_c; \\ 0, & \text{otherwise} \end{cases} \tag{17}$$

while the tophat filter is simply a low pass filter described by

$$H'_{tophat}(f) = \begin{cases} 1, & \text{if } |f| \leq f_c; \\ 0, & \text{otherwise} \end{cases}. \tag{18}$$

The cone filter and tophat filter are depicted in Figure 4.

It is clear that a more realistic representation of the received image of the target is given by

$$i(x,y) = o(x,y) * s(x,y) + n(x,y), \tag{19}$$

where $n(x,y)$ represents the random noise in the image.

Assuming a known power spectral density for both the object and the noise, it is possible to create a Wiener filter. The Wiener filter is a linear restoration filter that minimizes the mean square error between the object and the received estimate of the object. The transfer function for the Wiener filter (11:259) can be shown to

be

$$H_W(f_x, f_y) = \frac{S^*(f_x, f_y)}{|S(f_x, f_y)|^2 + \frac{\Phi_n(f_x, f_y)}{\Phi_o(f_x, f_y)}}, \qquad (20)$$

where Φ_n and Φ_o represent the power spectral densities of the noise and the object, respectively. When the signal to noise ratio is high, this expression reduces to the inverse filter defined above. This provides a basic method for reducing noise effects in the image.

However, the Wiener filter has two key deficiencies for imaging through atmospheric turbulence. It is unlikely that the power spectral densities for the object and the noise will be known. Secondly, better performance could be achieved with a filter that is capable of adapting to the changing blur caused by the turbulence.

2.3 Imaging Through the Atmosphere

Imaging satellites through the atmosphere presents several new variables into the classical pattern recognition problem. This section introduces the effects of atmospheric turbulence and photon flux considerations. Additionally, it introduces techniques that can be used to overcome some of the image quality degradation caused by these effects.

2.3.1 Turbulence and Target Image Blurring. The primary source of degradation in any type of telescopic image is atmospheric turbulence. Atmospheric turbulence levels are quantified by the Fried parameter, r_o. The Fried parameter is the effective diameter of a diffraction limited telescope that would yield the equivalent resolution in the absence of atmospheric turbulence. The value of r_o is independent of the physical dimensions of the telescope (15:1-2). However, r_o is known to vary greatly with time and location. Figure 5 shows the range of r_o values that were measured at an observatory at Capella, United Kingdom over a 40 minute period on 26 December 1993 (4). Average values of r_o at the Air Force Maui Optical Station (AMOS) are 12 cm in the summer and 10 cm in the winter (3).
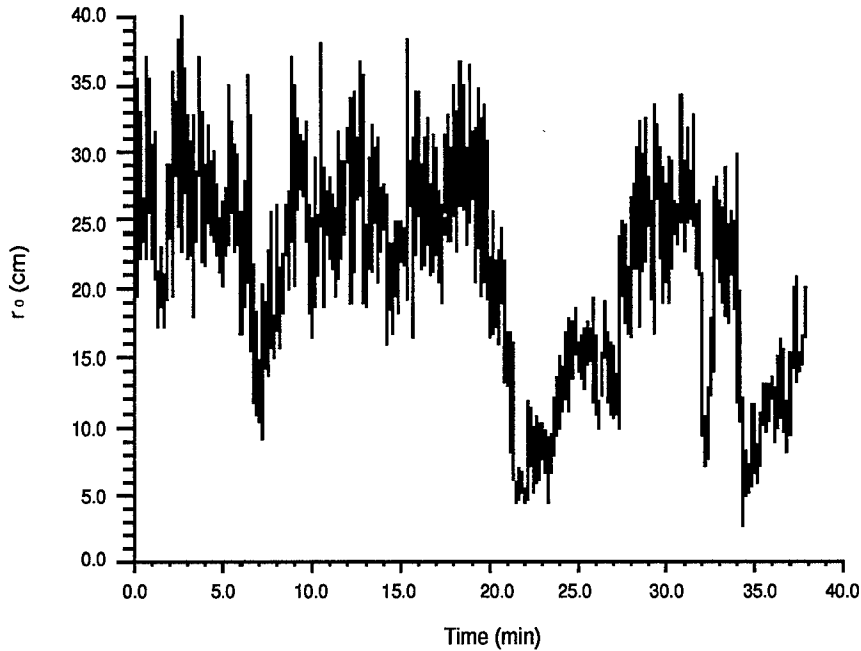
Figure 5. Temporal Variation of r_o at Capella, United Kingdom

An additional complication in imaging LEO satellites is that they are not stationary. The target is viewed through different parts of the atmosphere as it travels in its orbital plane. Each segment of the atmosphere varies statistically from other parts of the atmosphere, typically with different values of r_o. This, along with varying angles between the sun, satellite, and observatory results in a variation of the received image with time. As a result, the time duration of an exposure is limited. Multiple short exposure images must be measured and averaged for post-processing (15:1-3). Modern imaging systems create an image by averaging multiple frames. There is a practical upper bound to the number of frames which can be acquired. It is important, however, to note that SNR in the image is improved with multiple independent frames according to (24:4232)

$$SNR' = M^{\frac{1}{2}} \times SNR, \tag{21}$$

23

where SNR represents the single frame signal to noise ratio and M represents the number of frames. Because a typical LEO satellite's aspect relative to the telescope changes significantly on the order of every 3 to 10 seconds, there is a finite limit on the number of frames that can be obtained for averaging (27:1-1).

2.3.2 Adaptive Optics. In the early 1950's, the first short exposure images through the atmosphere of objects in space became available. These images were taken over a time frame on the order of milliseconds to essentially "freeze" the effects of atmospheric turbulence. These measurements yielded a series of "speckled" images. The original efforts to circumvent the effects of atmospheric turbulence focused solely on post processing techniques. This collection of techniques is now referred to as "speckle imaging" (21:123). Speckle imaging techniques suffer from poor SNR performance for small ensembles of images, such as those obtained during satellite surveillance operations.

The use of an adaptive optics (AO) telescope can greatly reduce the effects of atmospheric turbulence and overcome the SNR limitations inherent in speckle imaging. The goal of an AO system is to detect deformations in the incident wavefront and use a deformable mirror (DM) to make the appropriate compensation. A schematic of a typical AO system is shown in Figure 6 (21:9).

Early work in the field of adaptive optics focused only on tilt correction. Tilt correcting telescopes utilize a mirror that can be moved about two orthogonal axes to correct for a random tilt that is induced by the atmosphere (4). Eighty seven percent of the power of the wavefront fluctuations resides within this induced tilt (21:180). Tilt displaces the image within the observed image plane, but does not corrupt it in any other manner. In a modern AO system, tilt correction is generally used as the first phase in the correction. The tilt correction mechanism is responsible for "centroiding" the image (keeping it centered on the image plane) (15:1-4).

Distant
Object

Aberrated
Light

Telescope
Pupil

| Deformable mirror | Beam splitter | Imaging Sensor |

| Actuator command computer | Wavefront sensor |
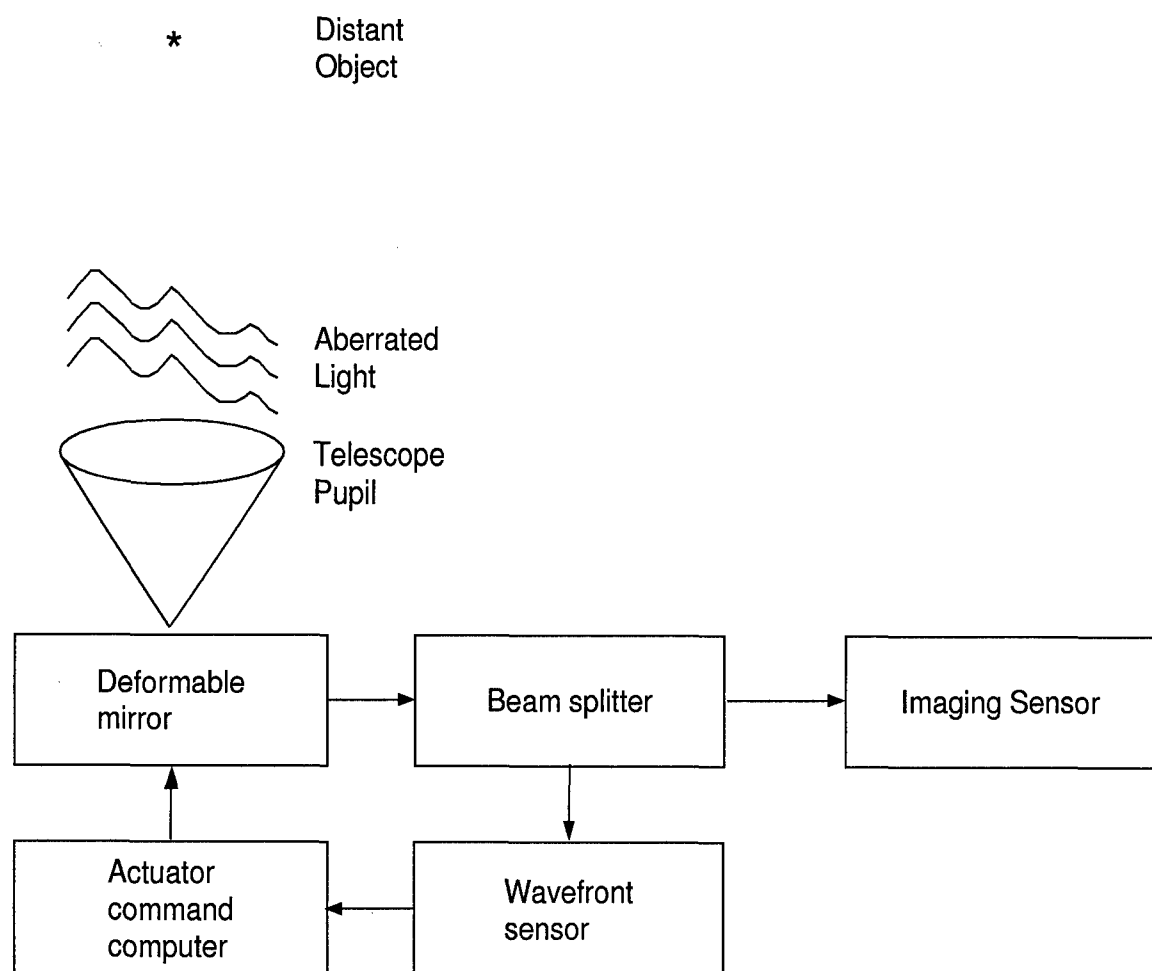
Figure 6. Schematic of a Typical Adaptive Optics System
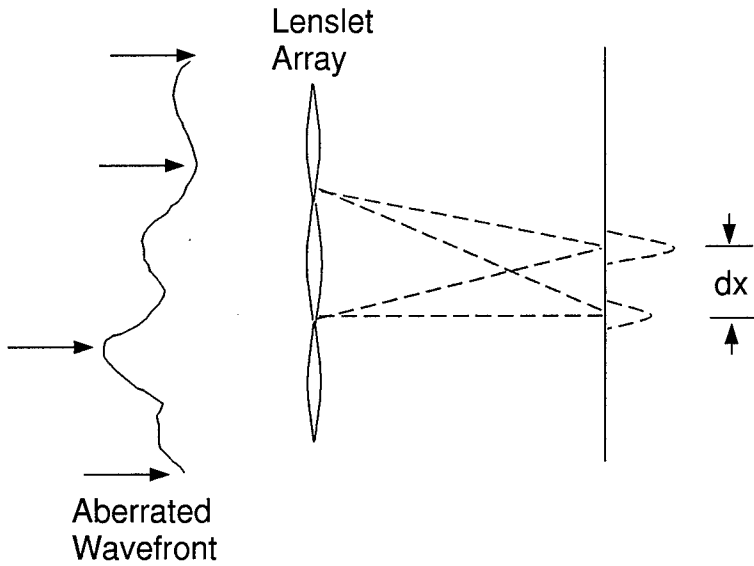
Figure 7. Schematic of a Shack Hartmann Wavefront Sensor

The turbulence corrupted wavefront enters the telescope and a sample of the wavefront is collected by a Wavefront Sensor (WFS). The WFS is used to sense the aberration at a high temporal frequency. One common type of WFS is the Shack Hartmann WFS shown in Figure 7 (4).

The Shack Hartmann WFS uses an array of microlenses to create a pattern of spots on a two dimensional detector array. The difference between the locations of these spots and those that would be present if the incident wave was planar and normally incident is proportional to the tilt in the corresponding subaperture (1).

The wavefront tilt is defined by Equation 22 (16).

$$\Theta_n = tan^{-1}\left(\frac{|dx|}{f_l}\right) \tag{22}$$

Θ_n is the tilt associated with the nth subaperture, dx is the spot location determined by the detecting the location on the subaperture detector with the highest intensity value, and f_l is the focal length of the WFS assembly.

The measurements made by the WFS outputs are used to determine the shape of the mirror that is required to counteract the effects of the turbulence. This position information is processed and the appropriate commands are sent to the actuators located behind the DM. The figure of the DM is adjusted to approximate the conjugate of the turbulence induced wavefront which is incident on the system (24:4227). By doing this, the resulting wavefront more closely represents what would be incident upon the system in the absence of atmospheric turbulence (21:178).

If an ideal adaptive optics system could be built, it would yield diffraction limited imagery. An imaging system may be defined to be diffraction limited if "a diverging spherical wave, emanating from a point source, is converted by the system into a new wave, again perfectly spherical, that converges toward an ideal point in the image plane, where the location of the ideal point is related to the location of the original object point through a simple scaling factor, a factor that must be the same for all points in the image field of interest if the system is to be ideal." (11:128)

In practice, diffraction limited performance is not realizable, even with the use of AO technology. For a real AO system the output phase is characterized as having a variance that is much smaller than that of the input phase. The result is a smaller aberration and improved image quality.

Clearly, neither the post processing techniques associated with speckled imaging nor the use of an AO telescope can completely negate the effects of imaging through a turbulent atmosphere. Speckle imaging is limited by the signal to noise ratio of the estimating routine used. AO systems face several key limitations due to factors such as the finite spatial sampling associated with the wavefront sensor, the limited degrees of freedom in the deformable mirror, and the finite time required for the system to respond to variations in the incident signal. The effectiveness of an AO system is also affected by errors and noise in the WFS measurements. These are especially significant at low light levels (15:1-5).

There is an economic and practical limit on the number of actuators that can be built into an AO system. A fully compensated AO system has approximately one WFS subaperture and one DM actuator per atmospheric coherence diameter, r_o (24:4227). Roggemann and Welsh (21:10) state that a 4 meter telescope operating with $r_o = 10$ cm would need approximately 1250 DM actuators and WFS subapertures to produce fully compensated imagery. This would utilize 10 cm spacing with the subapertures measuring 10 cm $\times$ 10 cm. Doubling these dimensions to 20 cm yields only partially compensated imagery, but requires only about 315 DM actuators and WFS subapertures.

2.3.3 Hybrid Imaging and Deconvolution. In an effort to combine the merits of both speckled imaging and AO technology, several hybrid imaging techniques have been developed. Deconvolution is one of the primary hybrid imaging techniques (21:247). A schematic of a typical hybrid imaging system is shown in Figure 8 (21:11).

Deconvolution relies heavily on the idea that high spatial frequency information with a good signal to noise ratio exists within a compensated image even though that image appears blurred. This occurs because the optical transfer function for the atmosphere/telescope interface is highly attenuated. Deconvolution may be used to reduce some of these effects and produce a sharper image. However, this approach has a signal to noise ratio induced limit on its effectiveness, above which noise effects are significantly amplified.

The foundation for this method lies in the expression for the signal to noise ratio of the detected image spectrum, $SNR_D(\vec{f})$, with a random OTF given by (21:271)

$$SNR_D(\vec{f}) = \frac{\bar{K} \left| E\{H(\vec{f})\} \right| \left| O_n(\vec{f}) \right|}{\sqrt{\bar{K} + (\bar{K})^2 \left| O_n(\vec{f}) \right|^2 var\{H(\vec{f})\} + P\sigma_n^2}}. \tag{23}$$

28
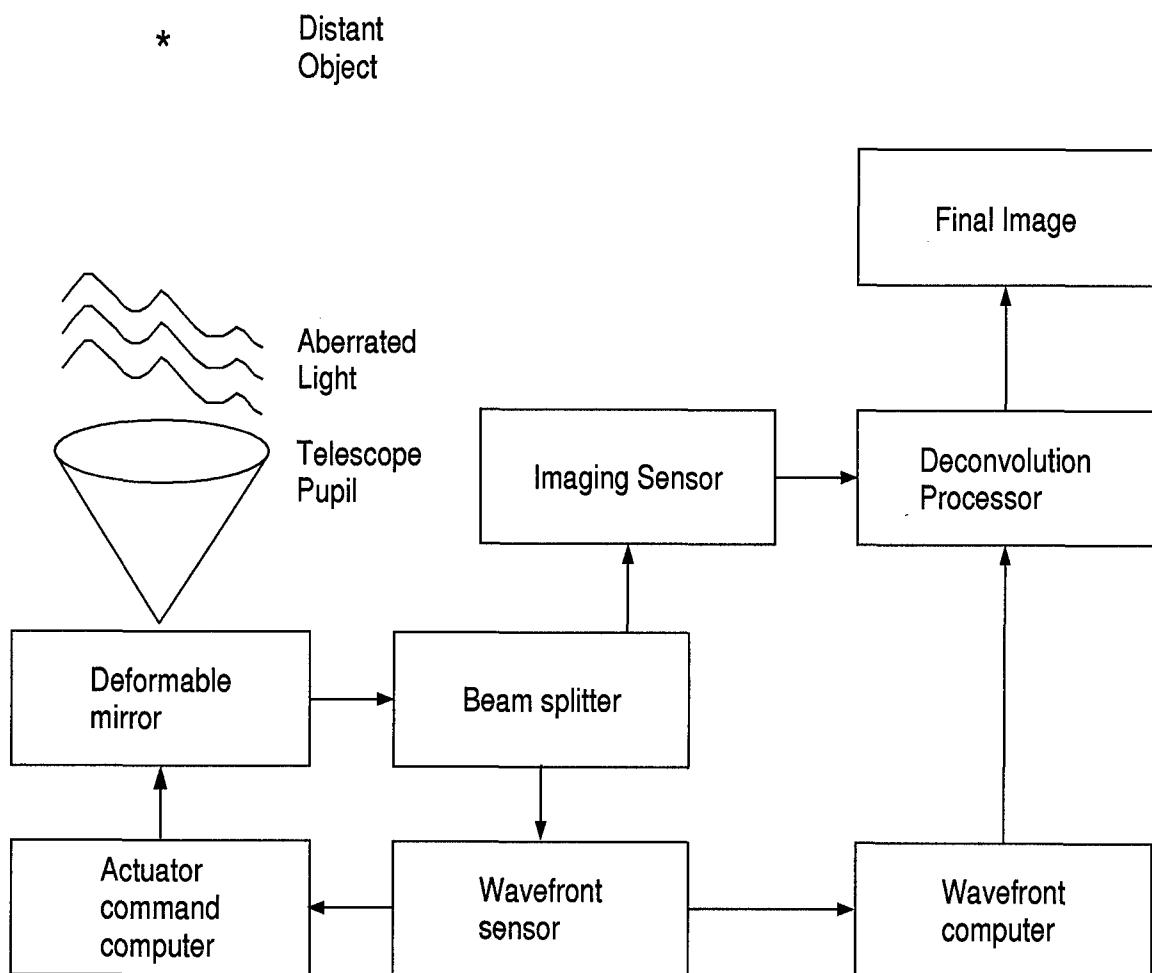
Figure 8. Schematic of a Typical Hybrid Imaging System

In this expression, $\bar{K}$ is the average number of photoevents per image, $O_n(\vec{f})$ is the normalized object spectrum such that it has a value of unity where $\vec{f} = 0$, P is the number of pixels in the image, and σ_n is the Root Mean Square (RMS) value of the additive noise in the detector pixels expressed as a number of photoevents. $H(\vec{f})$ is the system OTF. $E\{\cdot\}$ is the statistical operation of expected value and $var\{\cdot\}$ represents variance.

As $\bar{K}$ increases toward infinity, the value of $SNR_D(\vec{f})$ converges to the signal to noise ratio of the random OTF. If the exposure time is long enough so that the average OTF during the exposure time closely approximates the actual average OTF, the variance term in the expression above disappears, leaving

$$SNR_D(\vec{f}) = \frac{\bar{K} \left| E\{H(\vec{f})\} \right| \left| O_n(\vec{f}) \right|}{\sqrt{\bar{K} + P\sigma_n^2}}. \qquad (24)$$

Roggemann states that a sufficiently high signal to noise ratio at high frequencies allows for the deconvolution of images that are measured with highly attenuated OTF's (21:272). This provides the basis for the use of deconvolution for image reconstruction.

In practice, deconvolution is performed by simultaneously imaging the target and a reference star. In this thesis, a method described by Roggemann (24:4232) is used. The reference star is representative of an ideal point source. Of course, the target and the reference star are imaged through different portions of the atmosphere. However, these "slices" of the atmosphere are in the same vicinity, so the atmospheric effects in both are assumed to be very similar. The image of the reference star represents an approximation to the point spread function (PSF). The Fourier transform of the PSF is known as the Amplitude Transfer Function (ATF) (11:135). The OTF is simply the normalized autocorrelation function of the ATF (11:139). Both the target image and the image of the reference star are normalized

to have an integrated intensity of unity using

$$I'_{i,j} = \frac{I_{i,j}}{\sum_{i=1}^{256} \sum_{j=1}^{256} I_{i,j}}, \tag{25}$$

where I represents either the target image or the reference image. The Fast Fourier Transform is used to create the frequency representations of both images. Once these are normalized, the inverse filter is applied using

$$\hat{O}(\xi, \eta) = \frac{O(\xi, \eta)}{R(\xi, \eta)}, \tag{26}$$

where $O(\xi, \eta)$ and $R(\xi, \eta)$ are the frequency domain representations of the target image and the reference image, respectively.

As discussed in Section 2.2, noise effects will dominate $\hat{O}(\xi, \eta)$ in regions with a low signal noise ratio (SNR). To minimize these effects, a cone filter is applied to $\tilde{O}(\xi, \eta)$ with a cutoff frequency that is defined by the minimum SNR allowed. This minimum SNR is defined by the user. The establishment of this cutoff value for SNR represents a tradeoff between the reduction of noise effects and the maximum spatial frequency that is maintained in the image. Past experience has shown that a cutoff SNR value of 2 is suitable for this type of study. The determination of the appropriate Modulation Transfer Function (MTF) width using radially averaged SNR data is described by Figure 9.

The inverse Fourier transform of the result of this filter yields the deconvolved image of the target. A comparison of an original target image and a deconvolved image are shown in Figure 10. These images are simulations with $r_o = 10$ cm. Negative images are depicted for clarity.

Clearly, by using the atmospheric effects measured in the reference image to compensate for similar effects in the target image, it is possible to vastly improve the quality of the target image. This assumes that the SNR defined by Equation 24 is sufficiently high. Since SNR is approximately proportional to $\sqrt{\overline{K}}$, the effectiveness

31
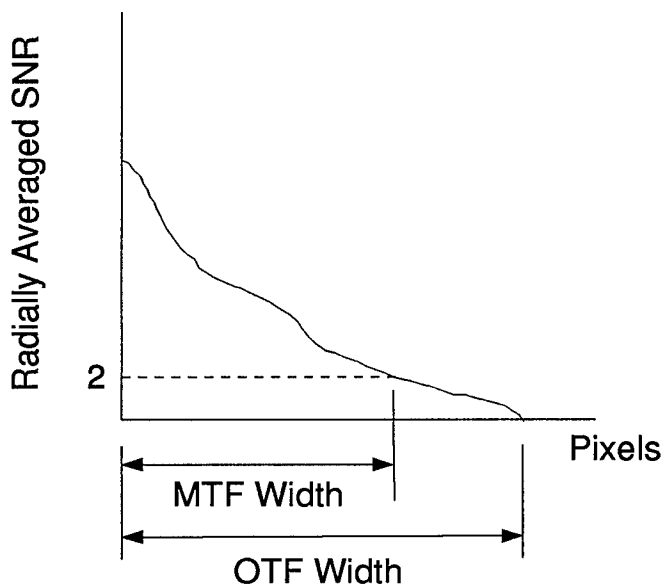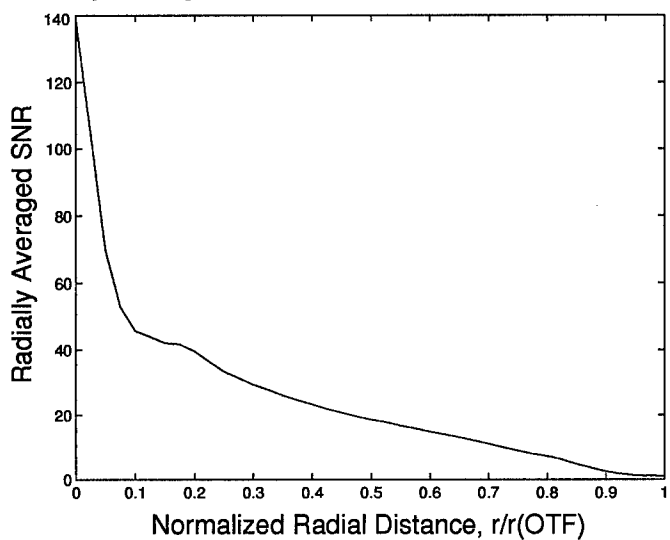
Figure 9. Determination of the Width of the MTF from Radially Averaged SNR Data

(a)   (b)
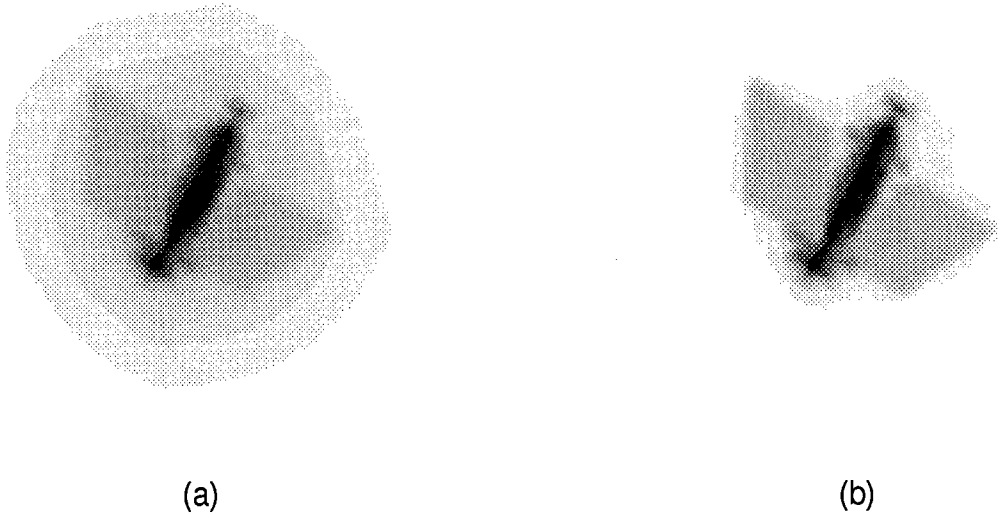
Figure 10.   Results of Utilizing Deconvolution Techniques on a Sample Image: (a)Measured Image (b)Deconvolved Image

of deconvolution is dependent upon the photon flux incident on the telescope from the target.

2.3.4   Visual Magnitude.   The photon flux from an orbiting satellite is generally quantified by its visual magnitude, M_v. M_v is a measurement of luminous flux density within the visible spectrum. Values for M_v vary from 0 upward, with 0 being the brightest. Visual magnitude is related to spectral irradiance on the ground, $E_{sat}(\lambda)$, by (23)

$$E_{sat}(\lambda) = E_{sun}(\lambda) \times (1.944 \times 10^{-11}) \times 10^{-0.4M_v} \text{ Watts/m}^2\mu\text{m}, \qquad (27)$$

where $E_{sun}(\lambda)$ is the spectral irradiance of the sun on the ground at the imaging wavelength. From this, the rate of photoevents per unit time, R, can be established. This rate is described mathematically by

$$R = \frac{E_{sat}S_R\Delta\lambda\tau_A\tau_o\eta}{\frac{hc}{\lambda_i}}, \qquad (28)$$

where $\Delta\lambda$ represents the imaging bandwidth, S_R represents the aperture area, τ_A and τ_o represent the transmission of the atmosphere and optics respectively, η is the quantum efficiency of the detector, h represents Plank's constant, c is the speed of light in a vacuum, and λ_i is the imaging wavelength. Given the integration time of the imaging system, this rate of photoevents can be converted to a photon count in the received image, $\bar{K}$.

2.4   Image Processing Techniques

Even with the application of hybrid imaging techniques, the target image is still obscured by noise and turbulence effects. Several image processing techniques can be utilized, dependent upon the purpose of the study. In this thesis, an emphasis is placed on the use of the Sobel edge map on the target image before applying it to the matched filter. The inherent blur in AO imagery taken through the atmosphere can greatly affect the edge determination. In the case of hybrid imaging, this blur can be a function of the degree of benefit gained by applying deconvolution. As described above, this is directly related to the photon flux dependent SNR in the received target image.

Signal to noise ratio decreases with increasing values of visual magnitude. As a result, the quality of the deconvolved images originating from these signals can still be poor. This dramatically limits the effectiveness of the Sobel edge map. Tukey developed a nonlinear image processing technique known as the median filter that is useful for noise suppression (20:294).

The median filter algorithm is performed by sliding a square mask composed of an odd number of pixels across the image. The center pixel is replaced by the median of the grayscale values covered by the mask. This is described mathematically for a 3×3 median filter by Equation 29.

$$P_{5,new} = median(m1, m2, \ldots m9) \tag{29}$$
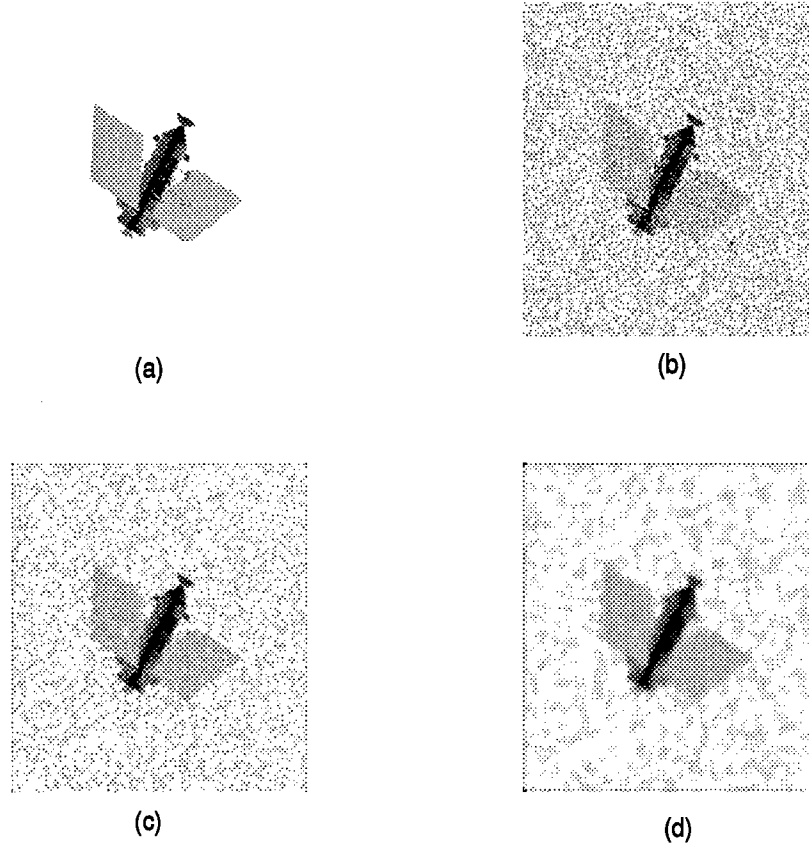
Figure 11.   Blurring Effects Due to the Application of a Median Filter: (a)Original
Image (b)Noisy Image (c)3x3 Median Filter (d)7x7 Median Filter

The values for m_i correspond to the values in the generalized spatial filter mask given in Figure 3. Each value in the mask defined by m takes on the grayscale value underneath it as it is moved across the original image.

The size of the mask is picked such that it is the minimal size necessary to provide the desired noise suppression while minimizing the associated blur. Larger masks tend to yield excessive blurring within the resulting image. This blurring is demonstrated in Figure 11. This figure shows a noise free image, the image with Gaussian noise added, and the results of applying a 3×3 median filter and a 7×7 median filter. Negative images are displayed for clarity.

This blur can result in a dilation of the image. For many applications, the extent of this dilation is negligible. This can, however, be a limitation for its utility with the matched filter because of the scale sensitivity described in Section 2.1.2.3. When the Sobel edge map algorithm is applied in conjunction with the matched filter, this can be treated in a manner applied by Pratt to the template matching problem (20:651). By thickening the resulting edges, effects due to dilation can be minimized.

2.5 Summary

This chapter included an introduction to the matched filter and its derivatives. It discussed the key deficiencies of the matched filter and ways in which they can be overcome. Additionally, this chapter provided an introduction to several techniques that can be used to improve the signal to noise ratio of a received image. Finally, it introduced the concept of the adaptive optics telescope and presented the basis for reconstructing an image using deconvolution. Several basic image processing techniques were also introduced. The following chapter demonstrates how these concepts were applied to the satellite pose estimation problem.

III. Methodology

3.1 Introduction

The theory presented in Chapter II provides a solid foundation for the matched filter techniques for satellite pose estimation. The present chapter discusses how this theory was used to obtain the results that are presented and analyzed in Chapter IV.

The following topics are discussed:

- Satellite Model Development

- Model of the Adaptive Optics Telescope

- Seeing Conditions

- Creation of the Test Image Database

- Test Procedures

The matched filter code and image processing techniques applied were written completely in MATLAB and the associated toolboxes except where noted. In order to yield reproducible and consistent results, only the default parameters were used as input to the built in MATLAB functions.

3.2 Satellite Model Development

A database consisting of models of three different satellites was developed. Unclassified computer models of the Defense Meteorological Satellite Program (DMSP), an ocean reconnaissance satellite (OCNR), and a fictitious satellite (Chucksat) were made available by the National Air Intelligence Center (NAIC).

Each vehicle's X, Y, and Z axes were defined within the pre-existing satellite models. For consistency, no attempt was made to develop a standard body fixed coordinate system with axes aligned along the velocity vector, earth pointing vector,

and pole vector. The goal for this study was to develop a database of images that are representative of the types of structures that are common on low earth orbiting satellites. So, this approach to model development was determined to be sufficient.

For each of the models, a constant X-axis rotation of 90 degrees was selected. Y-axis rotations were variable through 30 degrees, 45 degrees, and 60 degrees. The Z-axis rotations were varied from -150 degrees to +180 degrees at 30 degree increments. These rotation angles were selected to keep the number of test cases for this study reasonable for the allowed time frame while providing a sufficiently sized database to produce meaningful results. The X-axis and Y-axis rotations are somewhat arbitrary in nature. These were, however, determined to be sufficient for this study. The Z-axis approximates an axis of symmetry in the satellite designs considered in this study. As discussed in Section 2.1.2.1, the matched filter can easily confuse two objects of similar shape and size. This effect will, in general, be most important for satellite rotations about the axis of symmetry. Because of this, a full range of Z-axis rotations was considered.

The final product consisted of a database of 36 different poses for both Chucksat and DMSP. It should be noted that the 60 degree Y-axis rotation models of OCNR were cropped to varying extents with each Z-axis rotation. As a result, they were not considered to be realistic representations of satellite structures and were not used for this study. Only 24 poses of OCNR were considered.

3.2.1 Model Format. The satellite models were originally created using the SatAC Modeling Tool software package provided by the Air Force Phillips Laboratory Satellite Assessment Center (PL/WSA), Kirtland AFB, New Mexico. This software package provides a means to model a target in any desired three dimensional orientation. Additionally, the models are constructed to accurately represent the material composition of the actual satellite. This results in a higher fidelity

simulation of the target by providing the correct relative brightness of the satellite components under various conditions.

The models were developed at NAIC and were originally stored in Tagged Image File Format (TIFF). Each TIFF file was converted to a 256×256 pixel array of grayscale values. These arrays were then reshaped into $65,536 \times 1$ column matrices for use in the Hysim3 code. Hysim3 is a program developed at AFIT to simulate imaging through atmospheric turbulence.

3.2.2 Model Scaling. Hysim3 automatically scales the satellite models for a diffraction limited telescope. As a result, it is necessary to appropriately scale the non-aberrated images in order to use them as the known image database for matched filter approach. For this study, it was determined that all tests could be run at a fixed scale. In a practical application of this research, the target's ephemeris data would be available and would provide a highly accurate estimation of the slant range from the ground based observation point. For the purposes of this study, the following data was used to fix the scale factor:

Imaging Parameter	Value Used
Maximum number of subapertures across mirror, N_{sub}	10
Mirror diameter, d_{mirror}	1.0 m
Length of one side of the object array, L_{obj}	10 m
Range to Target, R_{tar}	500 km
Imaging wavelength, λ_i	0.7 μm

Table 1. Parameters Used to Determine the Appropriate Scale Factor

The diffraction limited cutoff frequency for the telescope is determined using

$$f_{max} = \frac{d_{mirror}}{\lambda_i \times R_{tar}}.$$

(30)

39

The spatial frequency sample spacing across the optical transfer function (OTF) array is given by

$$df = \frac{f_{max}}{R_{OTF}},$$ (31)

where R_{OTF} is the radius of the OTF measured in pixels, defined to be

$$R_{OTF} = (I_{space} - 1) \times N_{sub} + 1,$$ (32)

where I_{space} is a constant that internally sets the number of pixels across a subaperture in the Hysim3 routine. A value of 5 was shown in the Hysim3 documentation package to be sufficient for the 1.0 meter telescope considered in this study (8:14). The sample spacing in the object array is given by

$$dx = \frac{L_{obj}}{L_p},$$ (33)

where L_p is the number of pixels along one side of the object array. The spatial frequency sampling in the object Fast Fourier Transform array is then defined by

$$du = \frac{1.0}{dx \times L_p}.$$ (34)

The scale factor is then defined by

$$S_{fac} = \frac{df}{du}.$$ (35)

This results in a scale factor of 0.714286 for the images used. Hysim3 automatically generated the scaled image without noise and atmospheric effects for each satellite model. The scaled images then comprised the known image database used as a reference for the matched filter algorithm.

3.2.3 Model Storage. In order to minimize the computational time required for the matched filter tests, the matched filter associated with each known image

was created and stored rather than creating the filter each time a test was run. Because Pratt discusses the advantages of using edge maps with the matched filter, the matched filter associated with the Sobel edge map of each known image was also created and stored. The Sobel edge map was created using the default values for the tolerance that are included in the MATLAB Image Processing Toolbox (26). This was done so that the results of this research could be easily reproduced.

To reduce the memory requirements and computational time for the tests, the required data was written to a compact disk. The original 256 × 256 images, the scaled images, the matched filter associated with each of the scaled images, and the matched filter associated with the Sobel edge map of each scaled image were stored on a CD. This provided an efficient method to store and read this data without requiring a large amount of computer memory.

3.3 Model of the Adaptive Optics Telescope

For this study, an adaptive optics telescope with the following parameters was simulated.

Imaging Parameter	Value Used
Mirror diameter	1.0 meter
Number of Subapertures Across Mirror	10
Wavefront sensor wavelength, λ_w	0.6 μm
Imaging wavelength, λ_i	0.7μm
Number of independent frames	50

Table 2. Description of the Adaptive Optics Telescope Used in This Study

Tilt correction was utilized for all test cases examined. All satellite images were assumed to be of objects with a length of 10.0 meters. It was assumed that there was no delay between sensing an aberration and correcting for it with the AO system.

41
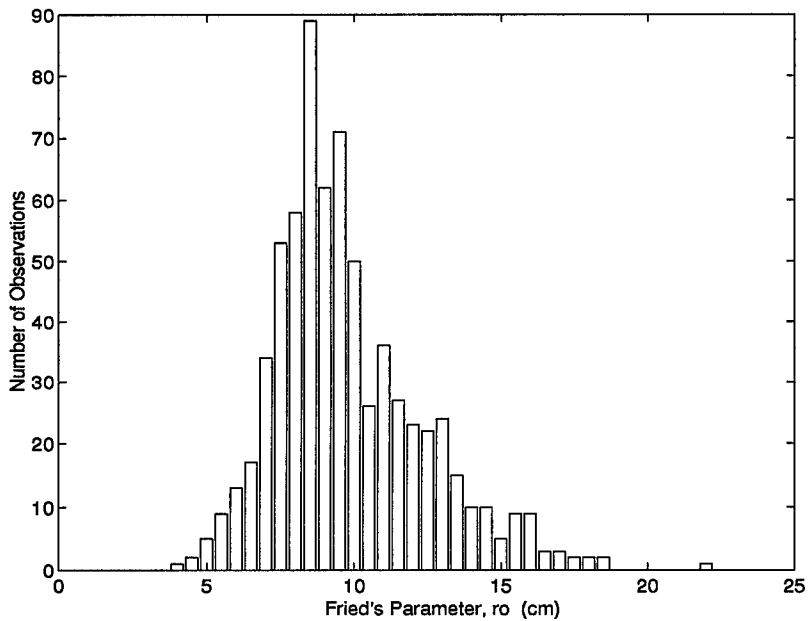
Figure 12. Historical Data for r_o Values Encountered When Imaging LEO Satellites at AMOS

3.4 Seeing Conditions

Seeing conditions are defined to be the combination of atmospheric turbulence levels and target illumination levels through which imagery is attained. A wide range of seeing conditions may be encountered in ground based space surveillance operations. This research attempts to examine pose estimation across a wide range of these conditions.

3.4.1 Turbulence Levels.
As previously discussed, the quality of the images received is largely dependent upon the level of atmospheric turbulence present during the observation. Typical values for Fried's parameter at Maui are in the range of five to eleven centimeters at a wavelength of 550μm (23). Historical data for r_o values encountered when imaging LEO satellites at AMOS was obtained and is presented in Figure 12 (2). For this study, r_o values of 7, 10, and 15 cm at an imaging wavelength of 500μm are considered.
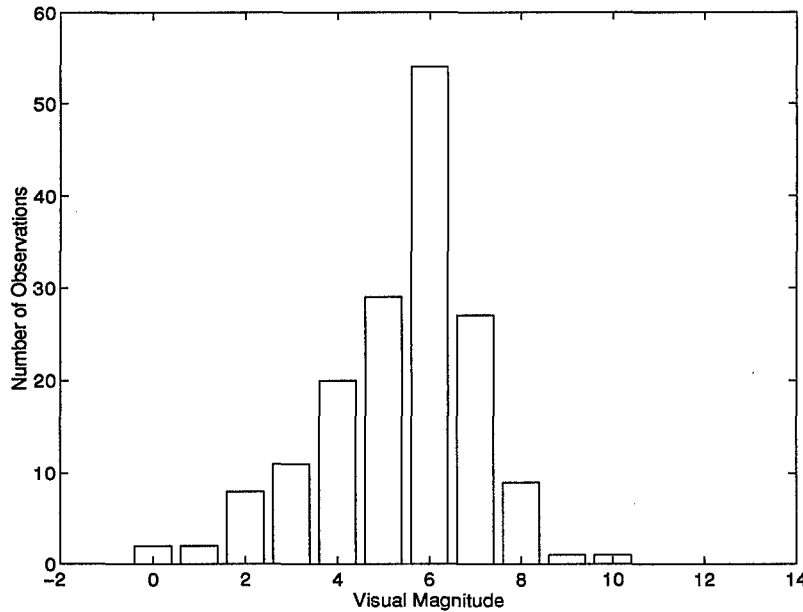
Figure 13. Historical Data for M_v Values Encountered When Imaging LEO Satellites at AMOS

3.4.2 Light Levels. Image quality also depends on the amount of light reflected by the target toward the observatory. Objects are classified by their brightness using visual magnitude, M_v. Typical values for M_v when imaging LEO satellites are in the range between 2 and 5. Geosynchronous Earth Orbiting (GEO) satellites typically have visual magnitudes on the order of 14 to 15 (23). At this low light level, detection is possible but very little usable shape information about the target can be attained because the resolution within the imagery is often greater than the satellite dimensions. Historical data on the visual magnitudes of LEO satellites imaged at AMOS was obtained and is presented in Figure 13 (2).

Visual magnitudes of 0, 4, 8, and 12 were considered in this study. Table 3 shows the parameters that were used to determine the photon flux for the light levels considered. The average number of photons per image and the number of photons per subaperture per integration time are shown in Table 4. These calculations were performed using Equation 28.

Parameter	Value
Spectral Irradiance of the Sun at λ_i	1430 Watts/m^2 μm
Spectral Irradiance of the Sun at λ_w	1750 Watts/m^2 μm
Imaging Bandwidth	0.07μm
Wavefront Sensor Bandwidth	0.12μm
Collecting Aperture Diameter	1.0 m
Length of One Side of the Square Wavefront Sensor	0.1 m
Combined Transmission, $\tau_a \tau_o \eta$	0.5
Integration Time	0.01 sec

Table 3. Parameters used for Light Level Calculations

Visual Magnitude	0	4	8	12
Average number of photons per image	26910117	675952	16979	426
Average number of photons per subaperture per integration time	616118	15476	389	10

Table 4. Incident Photon Flux as a Function of Visual Magnitude

3.5   Creation of the Test Image Database

The test image database was created using Hysim3. Hysim3 is a program that was created at the Air Force Institute of Technology to simulate the effects of atmospheric turbulence. It is capable of simulating both the imagery of a point source and an extended object. In the case of an extended object, the program automatically scales the image so that the frequency sampling of the Fast Fourier Transform of the object matches the frequency sampling of the Optical Transfer Function, as described by Equations 30 to 35. Based on the simulation parameters defined in the input file, Hysim3 simulates the user defined number of frame realizations. For this study, the number of frame realizations was set to 50 for all test cases. Since SNR is improved by a factor of the square root of the number of frames, this value was picked because it is representative of the maximum number of frames that can reasonably be attained for this type of imagery. The code calculates phase screens using a Gaussian random number generator. The Wavefront Sensor (WFS) model

44

determines the slopes in the wavefront across the WFS subapertures. It utilizes a least squares reconstructor to map the WFS phase difference measurements to the deformable mirror (DM) actuator commands. The least squares reconstructor minimizes the mean sum square of distances between actual slope sensor measurements and those which would result solely from a set of actuator commands (22:457). A summary of this method is given in the Hysim3 documentation package (8:19). The phase induced by the DM is subtracted from the phase screen generated by a Gaussian random number generator to create the compensated waveform. This wave front is used to compute the instantaneous OTF. Once the specified number of frames have been calculated for averaging, Hysim3 creates the simulated image.

Sample Hysim3 output images are shown in Figure 14. These images are of the DMSP satellite with a Y-axis rotation of 45 degrees and a Z-axis rotation of 30 degrees. Negative images are displayed for clarity. The quality of the images used in this study is affected by the fact that this work was accomplished at an unclassified level. Greater detail may be available at the classified level. Figure 24 shows three images from the known image database that are typical of those used as input to Hysim3.

Because the known image database consisted of 96 different satellite/pose combinations and the fact that the tests were run at twelve different lighting conditions, the initial set of images to be tested had to be defined early in the process. Ideally, all 96 original images would have been tested under each of the twelve lighting conditions. However, it was deemed that this was not a practical approach due to the time frame in which this study had to be conducted. The tests were conducted using one view of each satellite with 30, 45, and 60 degree Y-axis rotations. The Z-axis rotations selected were picked arbitrarily to serve as a valid representation of possible cases. The poses selected are described in Table 5.

Test images were created for each of these eight satellite poses using the twelve seeing conditions described in Table 6. Throughout the rest of this thesis, the target

(a)

(b)

(c)

(d)
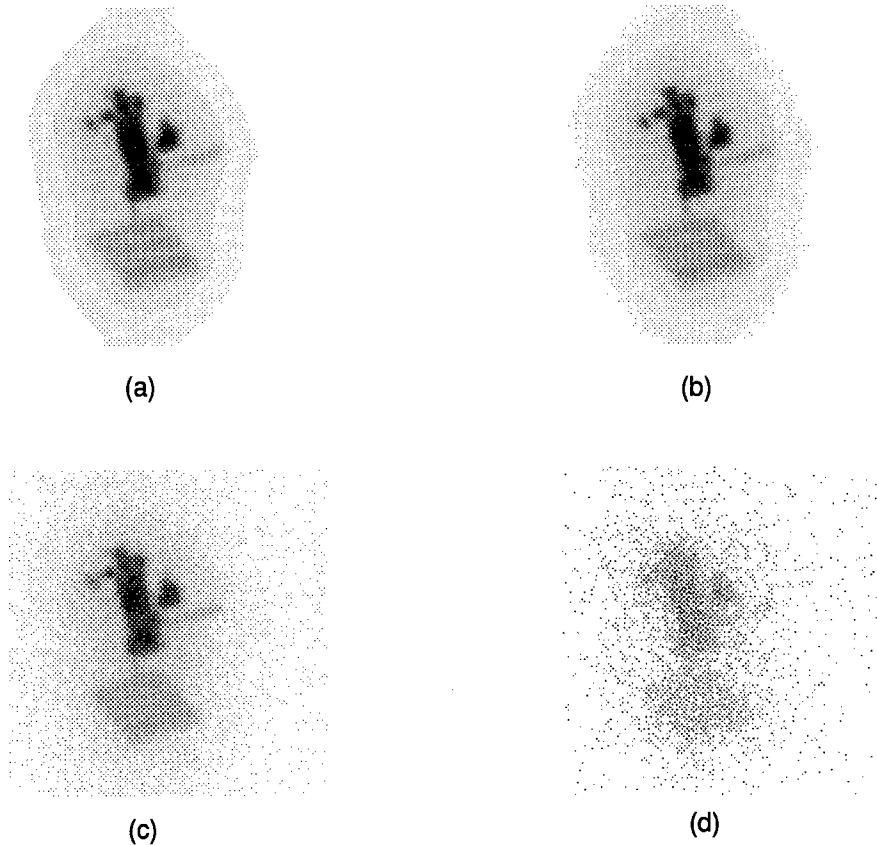
Figure 14. Sample Hysim3 Output Images for $r_o = 0$ and (a)$M_v = 0$ (b)$M_v = 4$ (c)$M_v = 8$ (d)$M_v = 12$

Satellite	Y-axis Rotation (degrees)	Z-axis Rotation (degrees)
CHUCKSAT	30	-150
CHUCKSAT	45	+0
CHUCKSAT	60	-120
DMSP	30	+120
DMSP	45	-30
DMSP	60	+180
OCNR	30	-60
OCNR	45	+90

Table 5. Satellite Orientations Used for the Matched Filter Tests

46

	$M_v = 0$	$M_v = 4$	$M_v = 8$	$M_v = 12$
$r_o = 7cm$	a	b	c	d
$r_o = 10cm$	e	f	g	h
$r_o = 15cm$	i	j	k	l

Table 6. Definition of Seeing Conditions Considered in This Study

satellites are named by the first letter of their names, the Y-axis rotation angle, a "p" or an "n" to represent positive or negative, followed by the Z-axis rotation angle. As an example, "c30n150" represents Chucksat with a 30 degree Y-axis rotation and a negative 150 degree Z-axis rotation. The seeing conditions examined in this study are referred to throughout this thesis by using the convention described by Table 6.

3.6   Test Procedures

The procedures followed for this research closely model the schematic shown in Figure 1 in Section 2.1.1. For the initial tests, the matched filter was applied to the original target images and their Sobel edge maps. These tests were then reaccomplished after applying deconvolution to the target images. Finally, it became apparent that the low SNR values associated with high visual magnitudes were yielding poor results for target images associated with low light levels. Image post processing techniques, including the use of the median filter, were examined in an attempt to improve results at high visual magnitudes.

3.6.1   The Methodology for the Matched Filter Tests.   The matched filter approach to satellite pose estimation was tested using each of the test images defined in Table 5. In a practical application of this research, the satellite type would be known. As a result each test image was classified by satellite type (DMSP, OCNR, or Chucksat) prior to the test.

The target image was energy normalized using the method defined by Equation 3 and the Fast Fourier Transform of the energy normalized test signal was calculated. The FFT of the test image was sequentially point multiplied by the matched filter

associated with an image in the known image database. The inverse Fourier transform of this product was calculated and the maximum value within the resulting matrix was established as the correlation value between the target image and the known image. This was repeated for the full range of known images in the database. The largest correlation value corresponded to the matched filter prediction of the target's pose.

In order to establish a solid baseline for this research, the code was initially tested using unaberrated images from the known image database as inputs to the matched filter routine. These tests of the matched filter were performed with multiple views of each of the three satellites studied. In every case, the code determined the correct pose for the input image. This allowed the experimental test cases to be run with a high degree of confidence that the code was working properly and had been completely debugged.

3.6.2 Matched Filter Algorithms. The basic matched filter and four variations were examined in this study. Throughout this thesis, the matched filter algorithms considered are named using the convention in Table 7. These are defined in more detail in the following sections.

Case Number	Description
1	Image Comparison, No Deconvolution
2	Sobel Edge Map, No Deconvolution
3	Image Comparison With Deconvolution
4	Sobel Edge Map, With Deconvolution
5	Median Filter, Edge Map, With Deconvolution

Table 7. Definition of Case Names

3.6.2.1 Case 1 and Case 2. The initial test cases, referred to as Case 1, were run using the aberrated test images, with no post processing techniques applied, as the input to the matched filter code. The Case 2 tests were simply the Case 1 tests repeated using the Sobel edge map of the target image. The target

48

edge map was applied to the matched filter associated with the Sobel edge map of the known image. Because of the degree of aberrations from atmospheric turbulence in the imagery, Case 1 and Case 2 were considered to be the "worst case" basis that would be used as a benchmark for variations on the matched filter approach. Schematics of the algorithms applied for Case 1 and Case 2 are shown in Figures 15 and 16, respectively.

The results of the tests are discussed in depth in Chapter IV. However, it should be noted here that turbulence induced blurring was determined to be the main cause for error in both Case 1 and Case 2. The matched filter tests using the Sobel edge map approach yielded a higher percentage of correct solutions to the pose estimation problem. The results were highly dependent upon seeing conditions. At lower light levels, the matched filter did not appear to be a viable tool for the pose estimation problem.

3.6.2.2 Case 3 and Case 4. In an attempt to improve upon these results, hybrid imaging techniques were applied to the target images before applying the matched filter. The first efforts to improve the results of the matched filter tests were based on the use of deconvolution.

Recon2 is a program provided by AFIT to deconvolve images from partially compensated measurements. It is based on a technique described by Roggemann (24:4232) which utilizes a reference image of a point source as seen under similar conditions as the target image to remove some of the inherent blur. A summary of this procedure is presented in Section 2.3.3.

Case 3 tests were the same as those performed in Case 1, except the AO imagery was deconvolved before applying it to the matched filter algorithm. Similarly, Case 4 tests were identical to Case 2, with the exception that the image was deconvolved before applying the Sobel operator. Schematics of the Case 3 and Case 4 algorithms are presented in Figures 17 and 18, respectively.
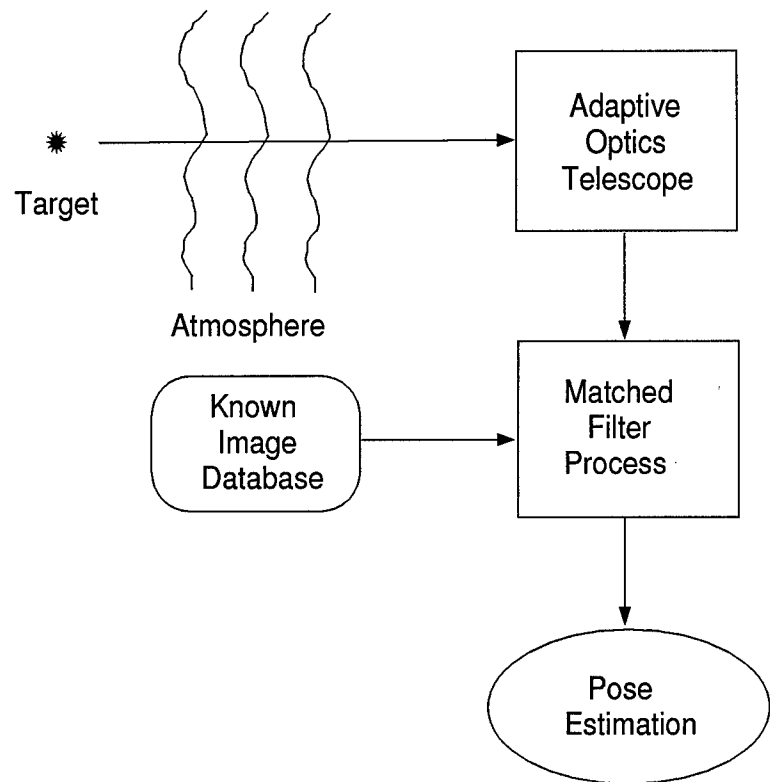
Figure 15. Schematic of Case 1
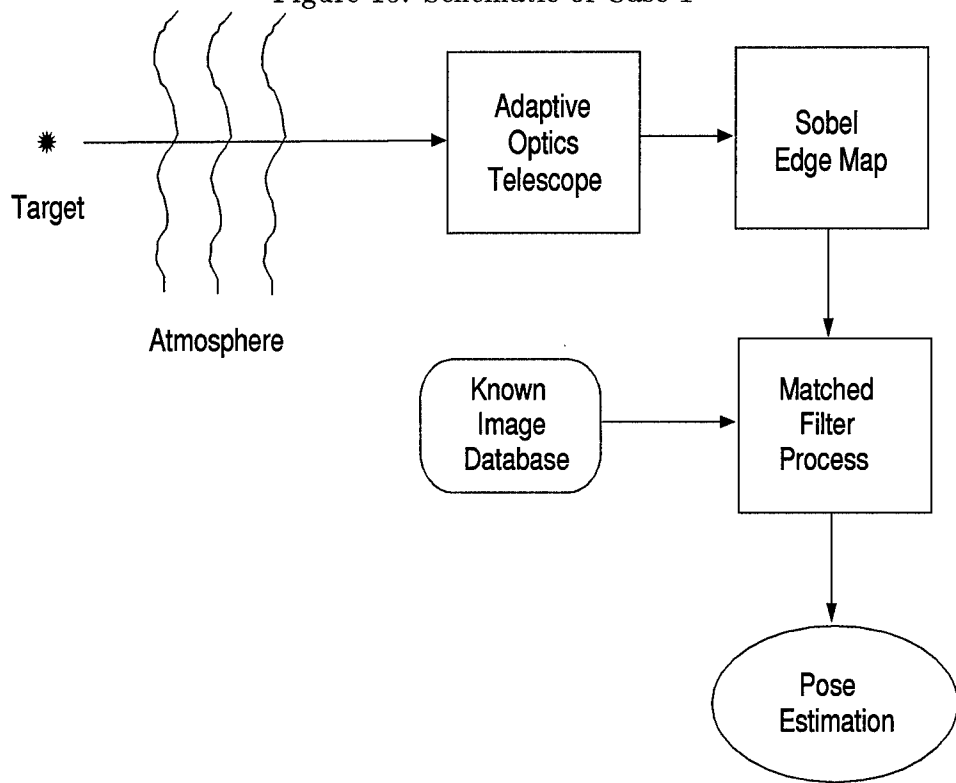
Figure 16. Schematic of Case 2
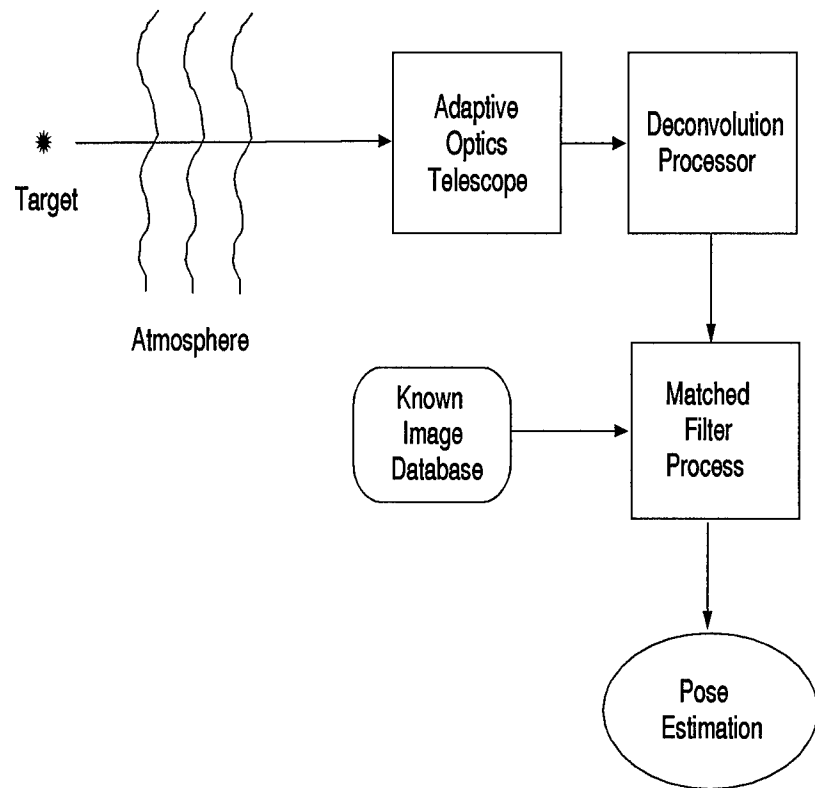
Figure 17. Schematic of Case 3
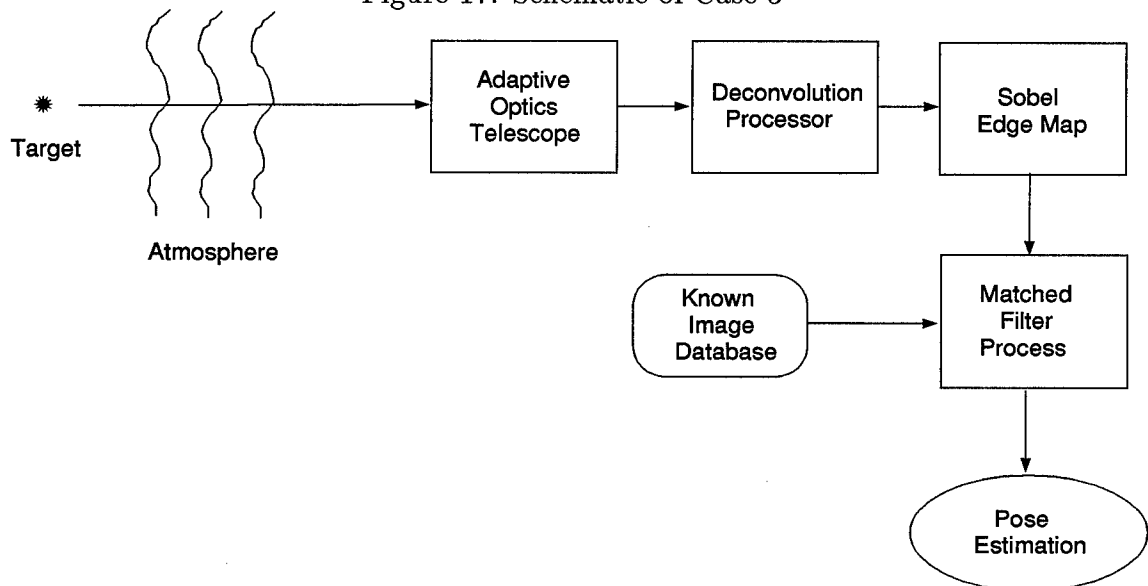
Figure 18. Schematic of Case 4

(a)   (b)
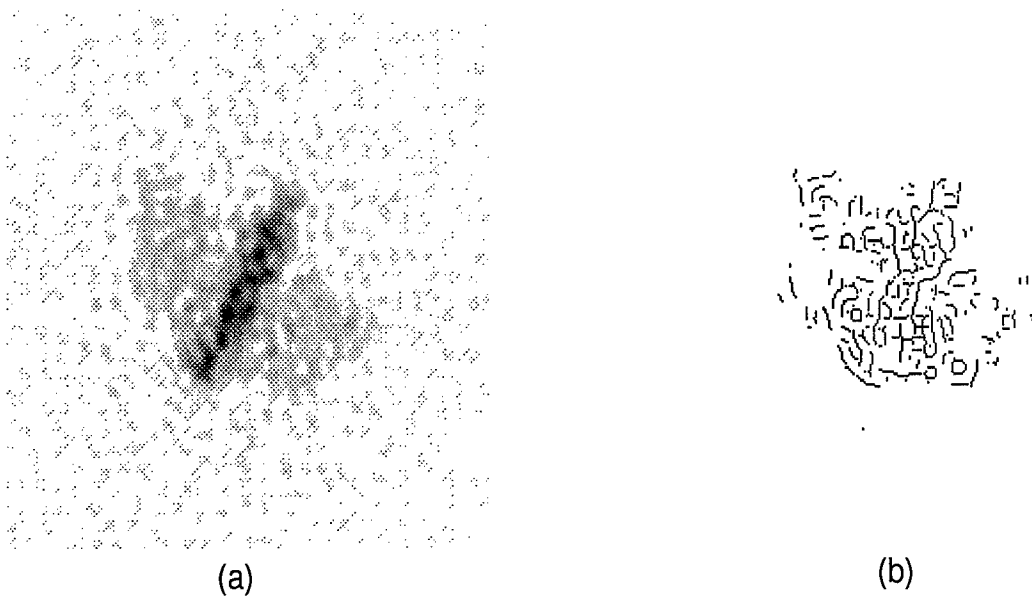
Figure 19.   Sobel Edge Map Demonstrating the False Edges Due to Deconvolution
at Low Light Levels; c30n150, $r_o = 10cm$, $M_v = 12$, (a)Deconvolved
Image (b)Sobel Edge Map of Deconvolved Image

3.6.2.3   Case 5.   The results of the matched filter tests using the
deconvolved images are discussed in detail in Chapter IV. The results are similar to
those achieved without deconvolution. The deconvolved images yielded a higher per-
centage of correct pose estimates, but similar problems were encountered for low light
levels. Again, the application of the Sobel edge map demonstrated a considerably
higher percentage of correct pose estimations.

A large portion of the errors encountered at low light levels using the Sobel
edge map algorithm were determined to be a result of the false edges demonstrated
in Figure 19. These were especially prominent within the Sobel edge maps of the
deconvolved images at low light levels. It was hypothesized that the pixels compris-
ing these false edges appear as parts of the target satellite to the matched filters
associated with the known image database. It became apparent that these effects
must be minimized in order to achieve more consistent results.

The median filter provides a method for reducing the apparent noise effects in
the target image. A 9×9 median filter was applied to the deconvolved images. This

52

(a)   (b)
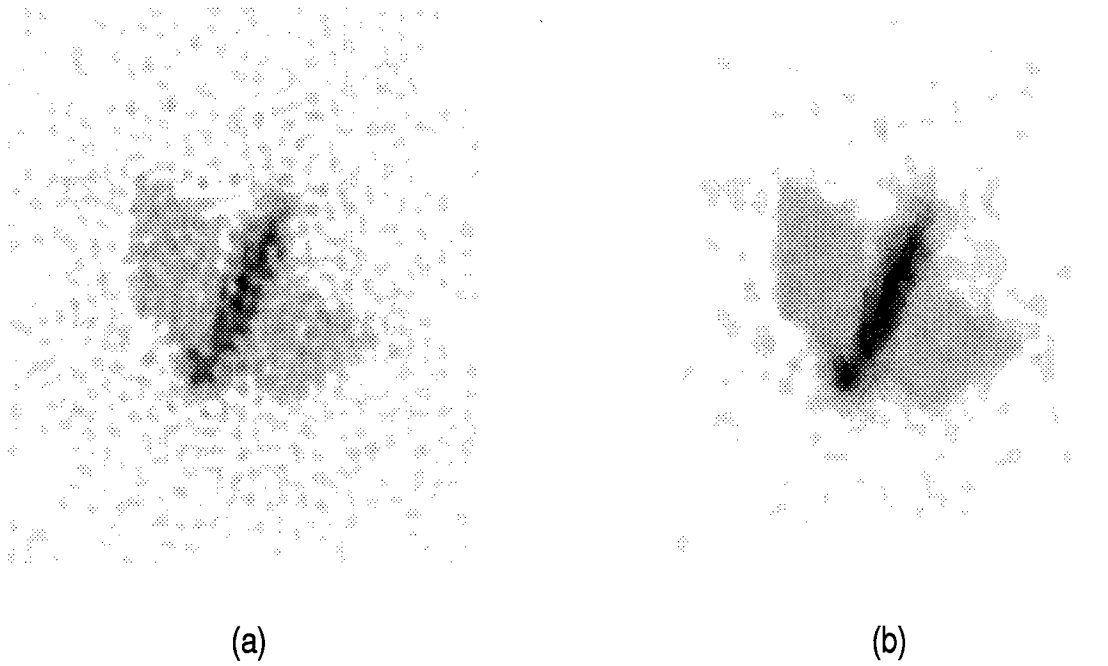
Figure 20.   Result of Applying a Median Filter to a Deconvolved Image:
(a)Deconvolved Image (b)Deconvolved Image After Application of a 9x9
Median Filter

filter successfully removed a significant portion of the false edges while trading off
contrast within the image. Figure 20 shows the deconvolved view of c30n150 with
the application of the median filter as seen using $r_o = 15$ cm and a visual magnitude,
$M_v = 12$. A negative image is shown for clarity.

Because of the blurring within the image due to the median filter, only the
Sobel edge map approach to the matched filter test was pursued. The median filter
has a tendency to distort the edges of the image, especially at low light levels. This
results in minor changes in the scale size of the image when the Sobel edge map is
applied.

As discussed in Section 2.1.2.3, the matched filter is extremely sensitive to
scale size. In order to overcome this, the lines of the binary image resulting from
the Sobel edge map were thickened using the default procedure in the MATLAB
Image Processing Toolbox (26). This is analogous to Pratt's discussion of template

53

Figure 21. Effects of Applying Line Thickening to the Sobel Edge Map of a Deconvolved Image Which Has Been Passed Through a 9 × 9 Median Filter; c30n150, $r_o = 10cm$, $M_v = 12$

matching techniques for image detection and registration (20:652). In the template matching algorithm, a replica of a target is compared to all of the objects in an image to determine its presence and location. The target template is edge thickened to provide a trade off between localization accuracy and scale size. Figure 21 shows the effects of this procedure on the Sobel edge map of the deconvolved image. A negative image is shown for clarity.

The Case 5 tests were an extension of those performed in Case 4. After the target image was deconvolved, a 9 × 9 median filter was applied to the image. The Sobel operator was then applied. To overcome the effects of dilation by the median filter, an edge thickening routine was used. At this point, the image was applied to the matched filters associated with the Sobel edge maps of the images in the known image database. A schematic of this algorithm is shown in Figure 22.
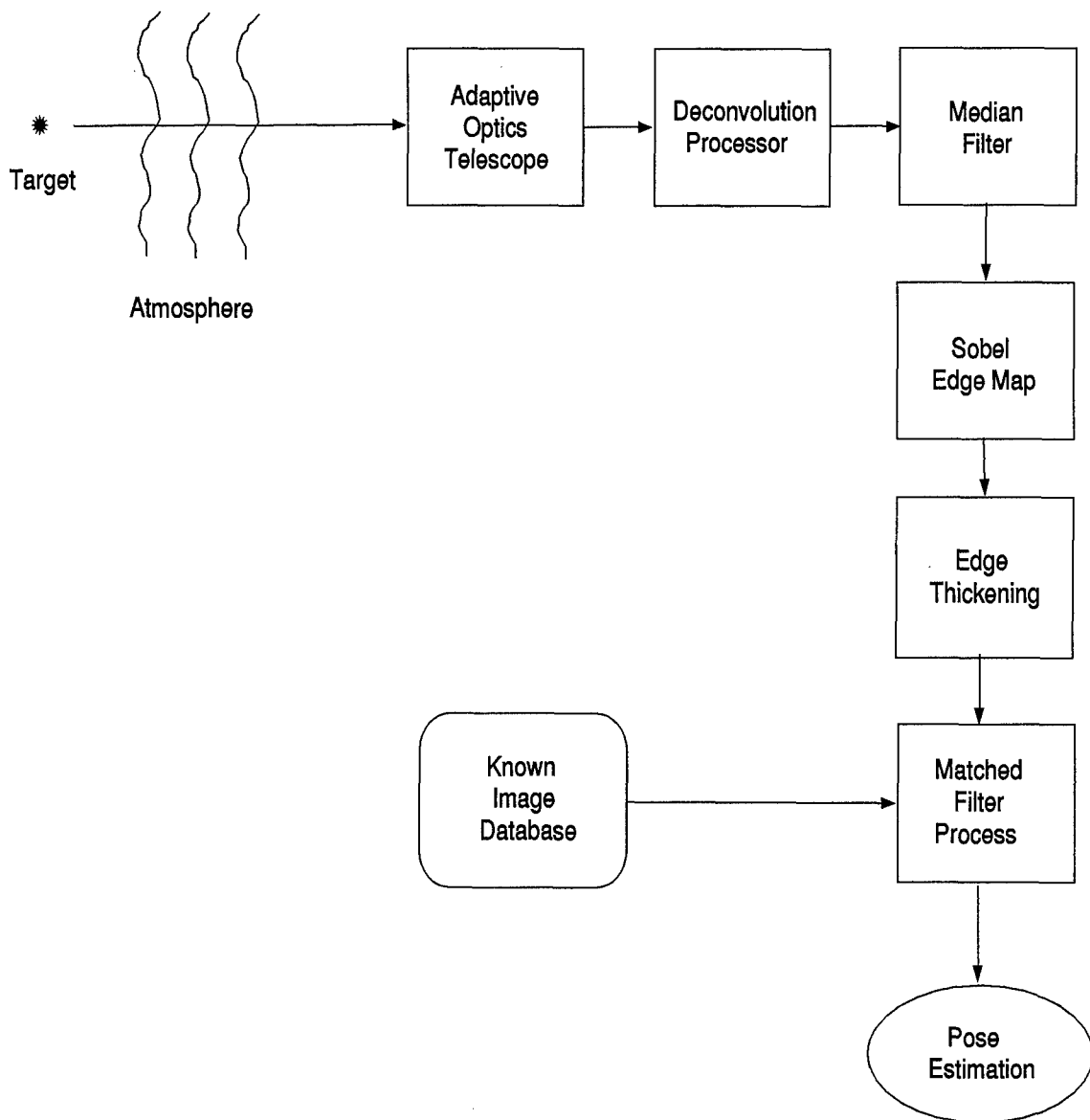
Figure 22. Schematic of Case 5

3.7 Summary

This chapter has given a thorough explanation of the methods used to test the application of the matched filter to the pose estimation problem. In the following chapter, the results of this work are presented. These results are analyzed to both determine the preferred method of applying the matched filter and draw conclusions regarding the limitations of this approach.

IV. Analysis of Results

To this point, the problem of satellite pose estimation has been summarized, the pertinent theory has been discussed, and the methodology used to implement the theory has been described. In this chapter, the results of the study are presented and analyzed.

4.1 Analysis of the Matched Filter Algorithms Examined in This Thesis

The most basic possible analysis of the results discussed above is to simply consider the number of correct pose estimations for each of the matched filter approaches that were examined. This was accomplished for the 96 satellite/seeing condition combinations in the test image database for each of the five matched filter algorithms. The results are summarized in Table 8. Complete tables of the results

Matched Filter Approach	Number of Correct Pose Estimations	Percentage of Correct Pose Estimations
Case 1	22	22.9 %
Case 2	47	49.0 %
Case 3	21	21.9 %
Case 4	70	72.9 %
Case 5	50	52.1 %

Table 8. Correct Pose Estimations for Each of the Matched Filter Algorithms

of these tests for all seeing conditions and filter algorithms considered are included in Appendix A. These tables show the pose that was determined by the matched filter under all 12 seeing conditions for each input. Separate tables are included for each matched filter algorithm.

The results in Table 8 appear to verify the hypothesis that the Sobel edge map techniques are superior to the basic matched filter for the pose estimation problem. However, it is also important to consider the correlation between the actual pose and the predicted pose for the cases where the matched filter yields an incorrect

57

estimation. To do this, it is necessary to develop a means of quantifying the incorrect outputs from the matched filter.

A common method used for the comparison of two images is the determination of a correlation value. According to Pratt(20:685), this is an especially useful tool if it is mathematically reproducible and corresponds well with visual image quality tests. Using a sum-square error approach, a matrix of spatial correlation values between each of the images in the known image database was developed. For each pair of images in the database, a normalized correlation value was calculated using

$$K_{i,j} = \frac{\sum_{m=1}^{256} \sum_{n=1}^{256} (Imagei_{m,n} \times Imagej_{m,n})}{\sqrt{\sum_{m=1}^{256} \sum_{n=1}^{256} Imagei_{m,n}{}^2 \times \sum_{m=1}^{256} \sum_{n=1}^{256} Imagej_{m,n}{}^2}}, \qquad (36)$$

where $Imagei$ and $Imagej$ represent the 256×256 arrays of grayscale values defining the two images. $K_{i,j}$ represents the spatial correlation between the two input images. $K_{i,j}$ is normalized so that a maximum value of unity is returned. This occurs only when $Imagei$ and $Imagej$ are identical. When the two input images are different, the correlation value lies in the range from 0 to 1, with strong correlations being represented by higher values.

For each test case examined, the correlation value between the known image database models of the actual pose and the predicted pose was calculated. These values were calculated using the images contained in the known image database since these are pure images with no atmospheric turbulence, diffraction, or photon noise effects. Complete tables of these correlation values can be found in Appendix B. Figure 23 is a cumulative probability distribution of the correlation values for each of the matched filter approaches examined in this thesis. Two key conclusions can be drawn from the cumulative probability distribution. First, the relative benefits of utilizing the Sobel edge map before applying the matched filter are clearly evident since Case 2 and Case 4 both have low occurence rates of low correlation values. Secondly, for the edge map cases, the correlation values associated with wrong pose
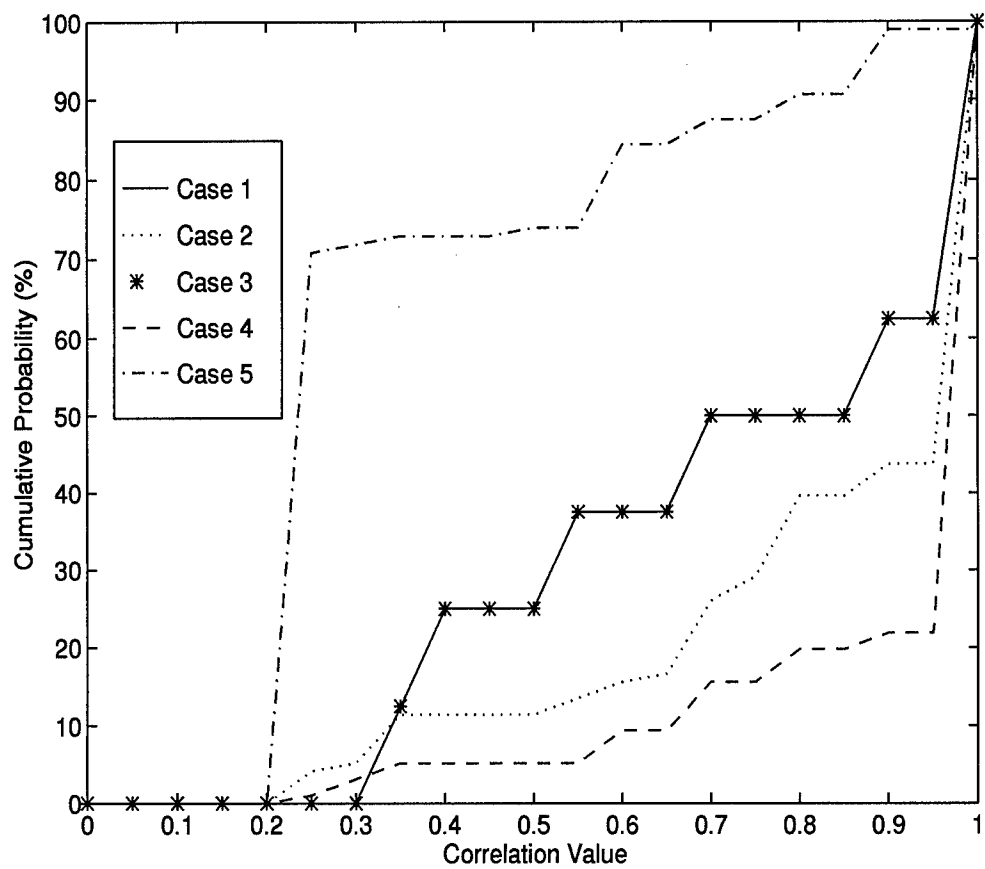
Figure 23. Cumulative Probability Distribution for Correlation Values Achieved With Each Approach to the Matched Filter Pose Estimation Procedure

Calculated Images	Input Images								
	c30n150	c30p0	c30p30	c30p150	c45p0	c45p180	c60n60	c60p0	c60p60
c30n150	7	0	0	0	0	0	0	0	0
c30p0	1	0	0	0	0	0	0	0	0
c30p30	2	0	0	0	0	0	0	0	0
c30p150	2	0	0	0	0	0	0	0	0
c45p0	0	0	0	0	9	0	0	0	0
c45p180	0	0	0	0	3	0	0	0	0
c60n60	0	0	0	0	0	0	0	0	1
c60p0	0	0	0	0	0	0	0	0	3
c60p60	0	0	0	0	0	0	0	0	8

Table 9. Confusion Matrix for Chucksat Using the Case 4 Algorithm

estimations are much higher. It should also be noted that the distributions were identical for Case 1 and Case 3.

Appendix C contains the confusion matrices for each of the three satellites studied with each of the matched filter algorithms. Table 9 is representative of these and demonstrates the confusion between 180 degree rotations about the axis of symmetry. The confusion matrix is structured in a manner such that the actual pose of the target is listed at the top of the table and the matched filter outputs are listed down the left side. The numbers in the matrix represent the number of occurrences of each input/output pair. Values along the diagonal are representative of successful pose estimations. Of particular interest in this confusion matrix are the outputs associated with c30n150 and c45p0. The output c30p30 is a 180 degree rotation about an axis of symmetry. The same is true for the output value of c45p180 for the input target of c45p0.

Matched Filter Algorithm	1.00	≥ 0.90	≥ 0.80
Case 1	22.9 %	37.5 %	50.0 %
Case 2	49.0 %	56.3 %	60.4 %
Case 3	21.9 %	37.5 %	50.0 %
Case 4	72.9 %	78.1 %	80.2 %
Case 5	52.1 %	70.8 %	79.2 %

Table 10. Occurrence Rates of Correlation Values

While these must be categorized as incorrect pose estimations, it should be noted that these errors were often between poses with stronger than a 90 % correlation. The occurrence rates of correlation values are summarized in Table 10. Again, it appears that the matched filter algorithm using the Sobel edge map of the deconvolved image provides the best results. The median filter approach to this method shows a dramatic drop in perfect correlations but shows similar results for correlation values above 0.8 and 0.9. The confusion matrices found in Appendix C again show a relatively high rate of 180 degree errors about the axis of symmetry. This accounts for the large number of wrong predictions with correlation values above 0.90. Figure 24 provides sample images from the known image database for each of the three satellites studied. From these, it is apparent that there is an approximation to symmetry for a 180 degree rotation about the body Z-axes for Chucksat and DMSP. The same is true for 90 degree rotations about the body Z-axis for OCNR.

The acceptance of symmetry errors as correct pose estimations is highly dependent upon the satellite being imaged and the application for which the imagery will be used. Figures 25 through 29 indicate the performance of each of the matched filter algorithms under all twelve seeing conditions, both with and without symmetry errors considered as correct pose estimations.
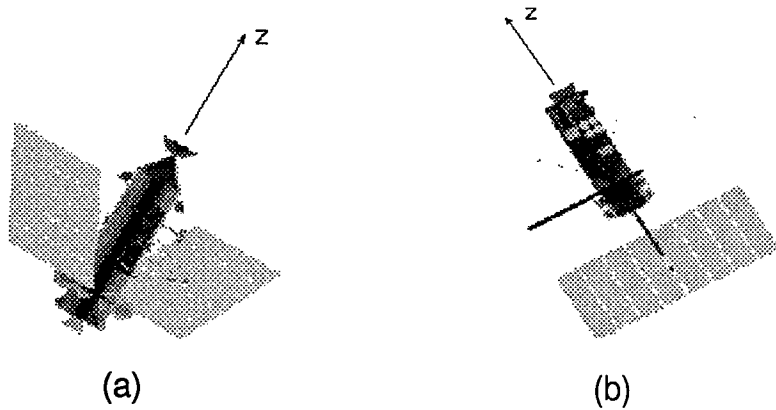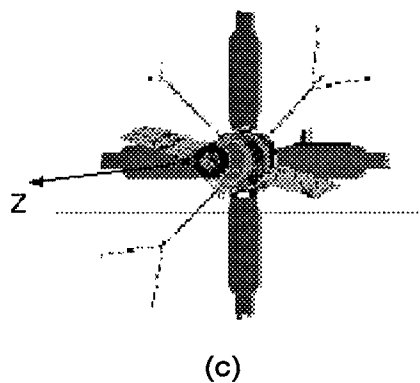
Figure 24.   Sample Images From the Known Image Database Demonstrating Symmetry Qualities of the Satellites Studied: (a)c30n150 (b)d30p90 (c)o45p0
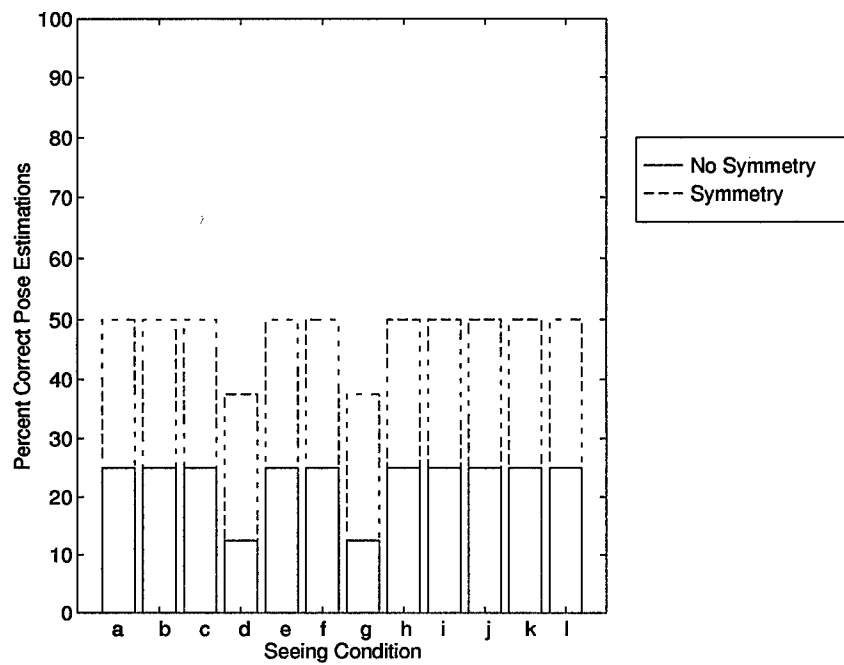
Figure 25. Performance of Matched Filter Algorithms by Seeing Condition, With and Without Symmetry Errors Allowed: Case 1
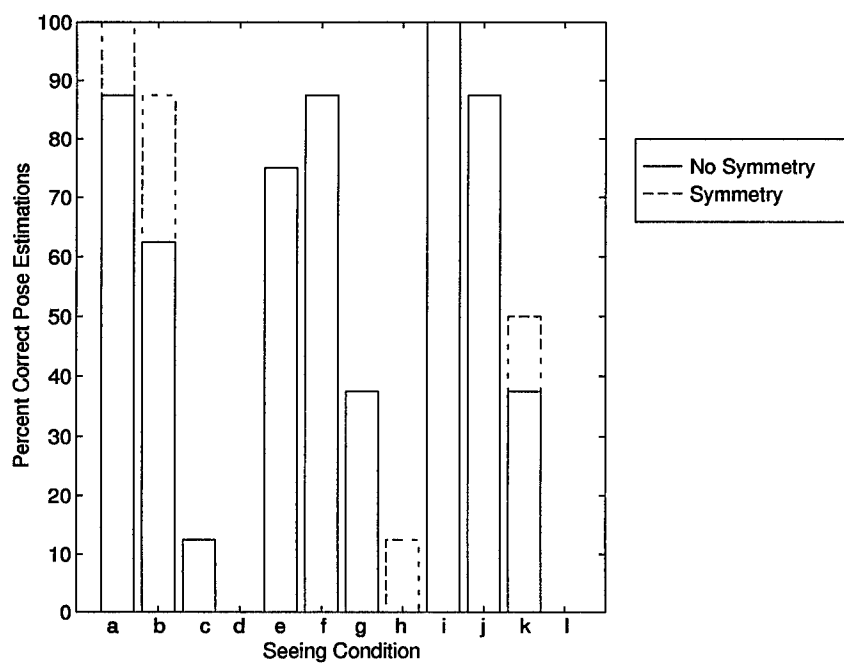
Figure 26. Performance of Matched Filter Algorithms by Seeing Condition, With and Without Symmetry Errors Allowed: Case 2
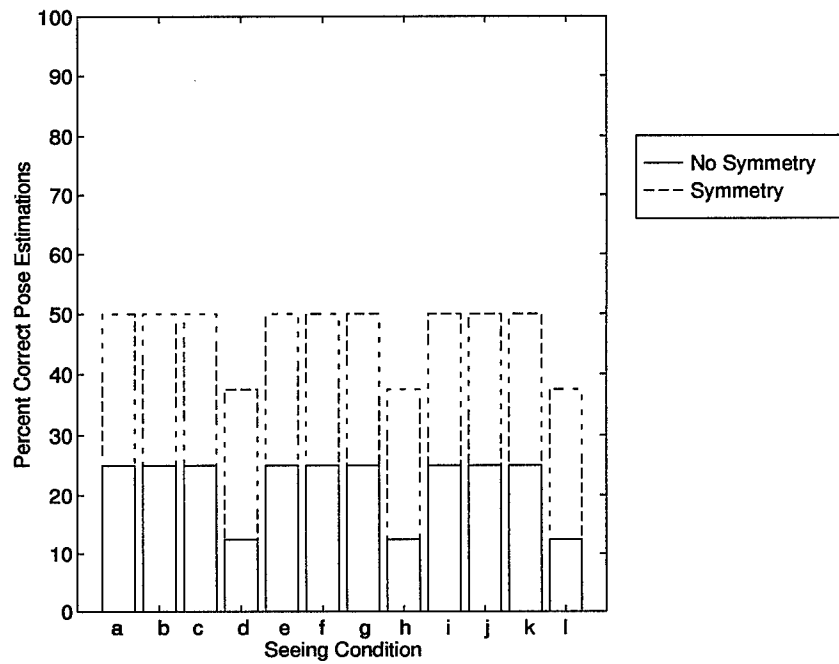
Figure 27. Performance of Matched Filter Algorithms by Seeing Condition, With and Without Symmetry Errors Allowed: Case 3
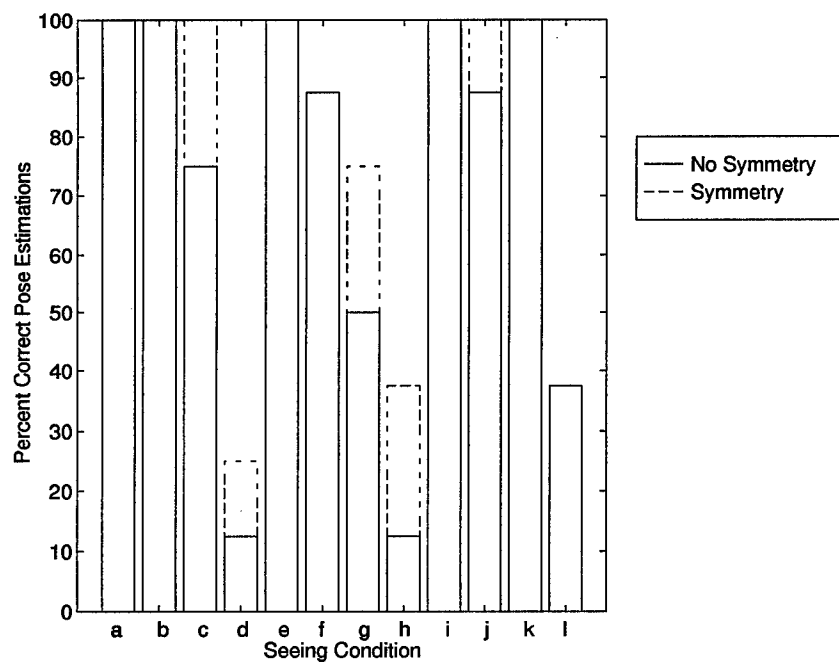
Figure 28. Performance of Matched Filter Algorithms by Seeing Condition, With and Without Symmetry Errors Allowed: Case 4
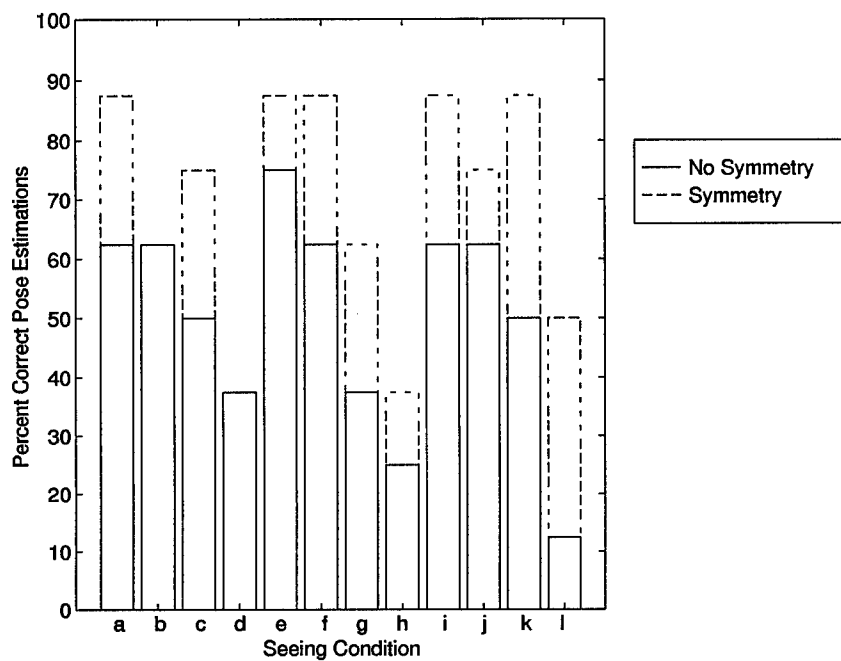
Figure 29. Performance of Matched Filter Algorithms by Seeing Condition, With and Without Symmetry Errors Allowed: Case 5

4.2 Limitations of the Matched Filter for the Satellite Pose Estimation Problem

The analysis above provides excellent insight into the relative effectiveness of the different approaches taken to the utilization of the matched filter for the pose estimation problem. However, it neglects to consider the effects of atmospheric turbulence levels and lighting conditions. This information is essential for the determination of the limits of the matched filter for this problem.

To determine the limitations of the matched filter techniques, it is essential to consider the results at each level of atmospheric turbulence and each light level that is considered in this study. In practice, a wide variety of lighting conditions and atmospheric turbulence levels can exist in numerous combinations. This study considers several discrete combinations that are considered to be representative of those encountered when imaging LEO satellites from ground based observatories.

4.2.1 Dependency on r_o.

The value of Fried's parameter, r_o, plays a significant role in the signal to noise ratio associated with an image. This dependency is demonstrated in Figure 30. Figure 30 represents the radially averaged SNR associated with a point source imaged with the 1.0 meter telescope described in Section 3.3. These plots are for a simulated point source with $M_v = 0$ and r_o values of 7, 10, and 15 cm. An OTF radius of 40 pixels is represented. This figure demonstrates the expected results. As r_o, the equivalent diameter of a diffraction limited telescope, increases there is a significant rise in the signal to noise ratio extending into the higher spatial frequencies. The higher SNR near the OTF cutoff frequency results in a decreased amount of blur in the image. Additionally, the MTF cutoff frequency, as defined in Figure 9, increases. This tends to minimize the loss of edge information during the deconvolution process, again resulting in a sharper image.

The results of this study were categorized by the r_o value for each algorithm to determine the effect on the overall performance of the matched filter when applied to the pose estimation problem. The average percentage of correct pose estimations as
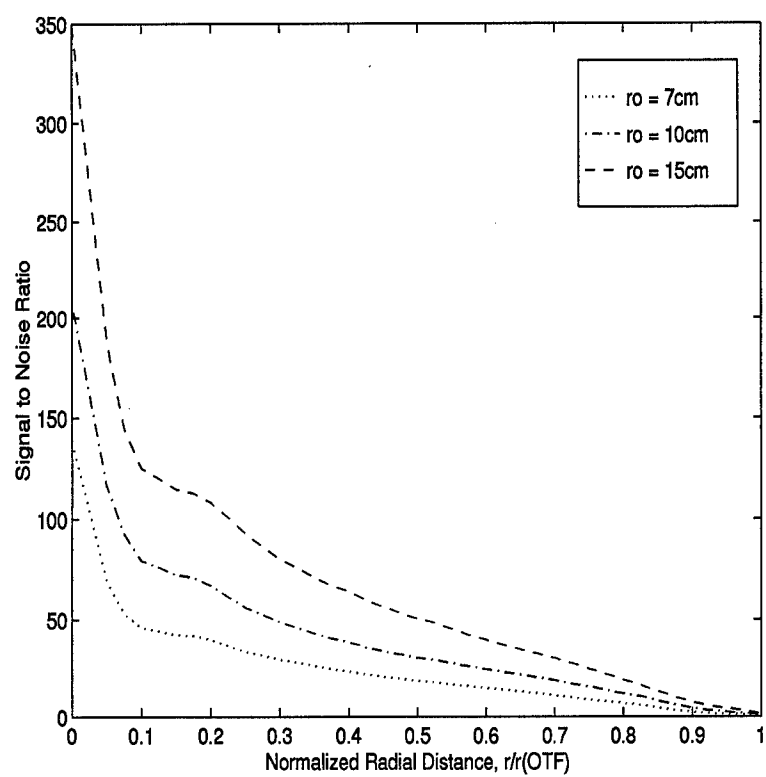
Figure 30. Radially Averaged SNR as a Function of r_o

a function of r_o for each matched filter algorithm is plotted in Figures 31 through 35. Data points with error bars are shown to demonstrate the deviation from the mean with visual magnitude. Separate plots for each algorithm are provided for clarity.

It is apparent that the algorithms which utilize the Sobel edge map, in most instances, provide a higher likelihood of correct pose estimation. Based on the plots for Cases 1 and 3, the performance for the image to image correlation routines is not greatly affected by the visual magnitude of the target. However, significant decreases in performance with increasing visual magnitude are evident in the plots for Cases 2 and 4. The wide ranges of data points for the Sobel algorithms indicates that their performance may be more highly dependent upon visual magnitude than on atmospheric turbulence. The error bars in the plot for Case 5 are much narrower than for the other Sobel approaches. The median filter in Case 5 masks some of the noise effects in the target image. Since SNR has been shown to be proportional to the square root of the photon count incident on the collecting device, these observations seem to lend additional support the hypothesis that the Sobel algorithms are highly dependent upon the visual magnitude of the target. The range of data points in these plots is too diverse to make any definitive statements regarding the effect of r_o on the pose estimation algorithms.

4.2.2 Dependency on Visual Magnitude. As defined by Equation 24 in Chapter II, the visual magnitude of the target is an important contributor to the signal to noise ratio. Figure 36 shows the variation observed at $r_o = 15$ cm of SNR as a function of M_v for a point source measured with a 1.0 meter telescope. The OTF radius is 40 pixels. This figure demonstrates an important contributing factor to the decreased performance of the matched filter in the pose estimation algorithm at low photon flux levels. At the lower visual magnitudes, there is a minimal difference in the SNR. However, the signal to noise ratio is dramatically degraded at $M_v = 12$. This decreased SNR causes the higher spatial frequency information to be buried in the received image. The width of the MTF filter is decreased, resulting in a

68
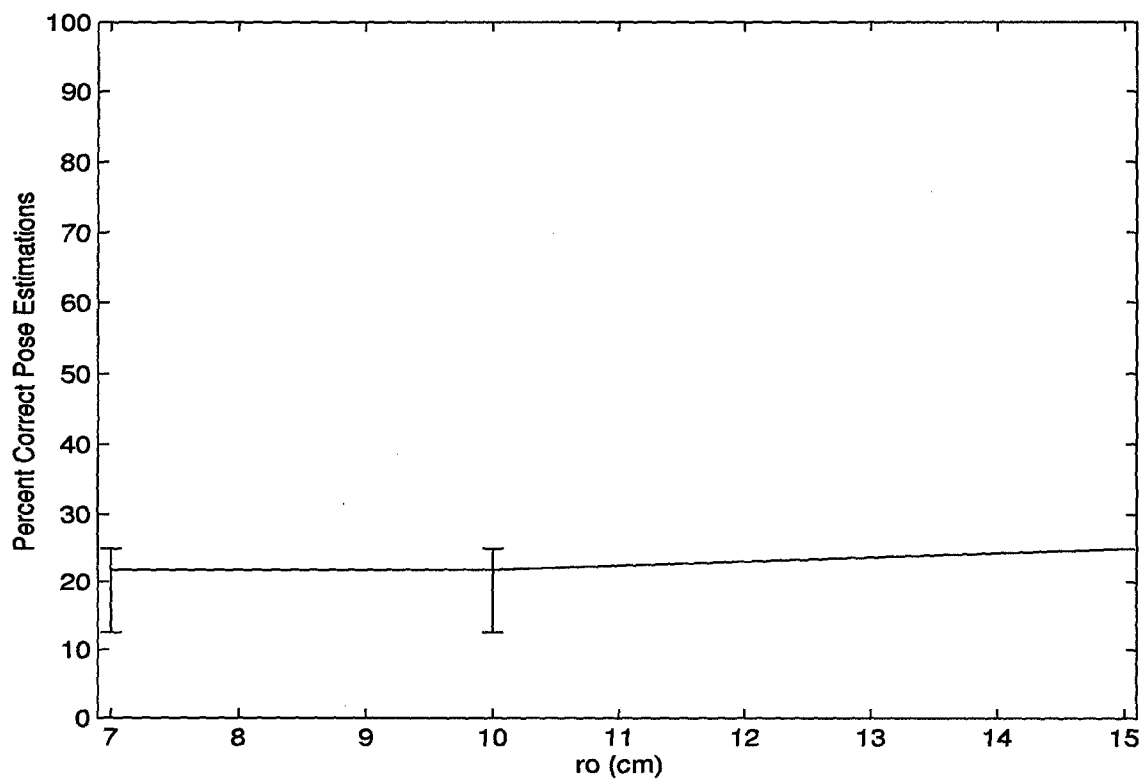
Figure 31. Correct Pose Estimation as a Function of r_o: Case 1
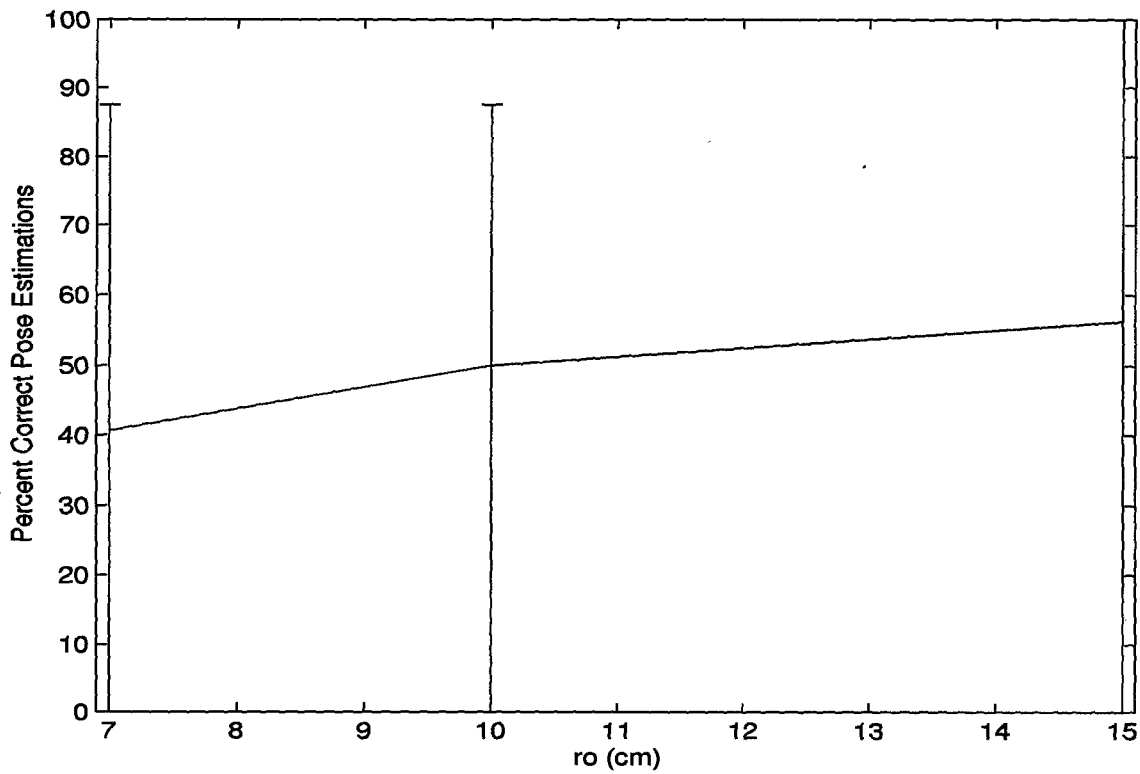
Figure 32. Correct Pose Estimation as a Function of r_o: Case 2

69
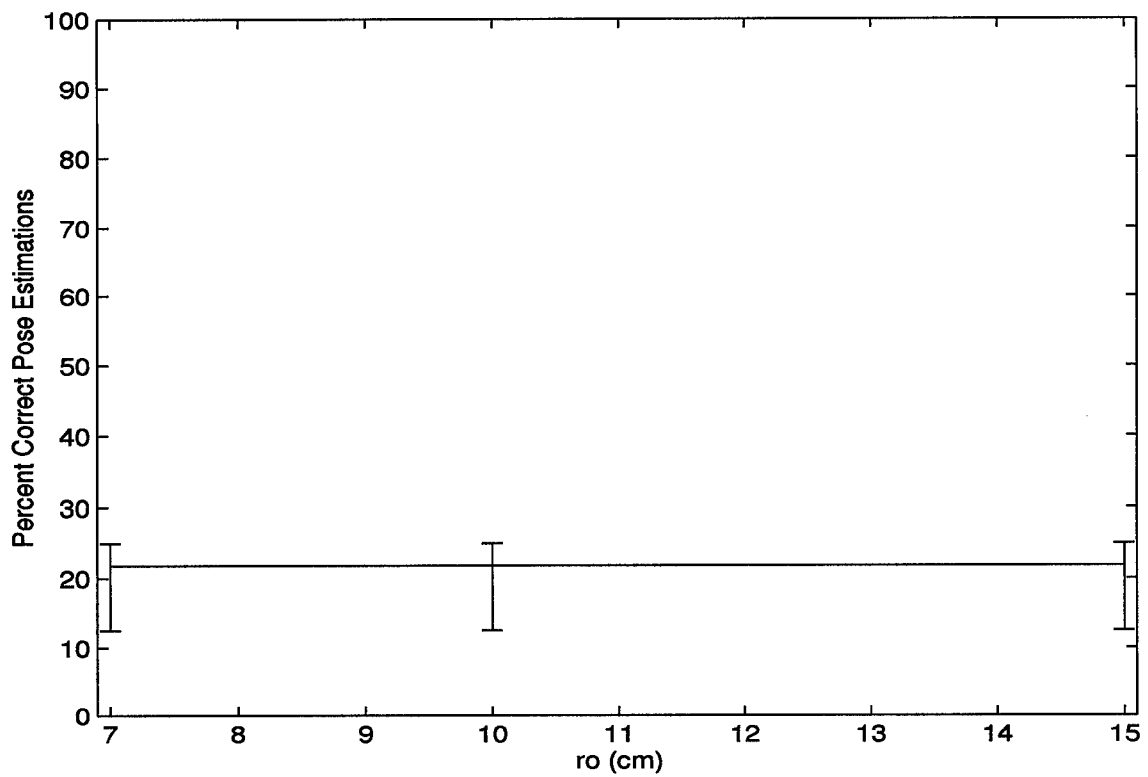
Figure 33. Correct Pose Estimation as a Function of r_o: Case 3
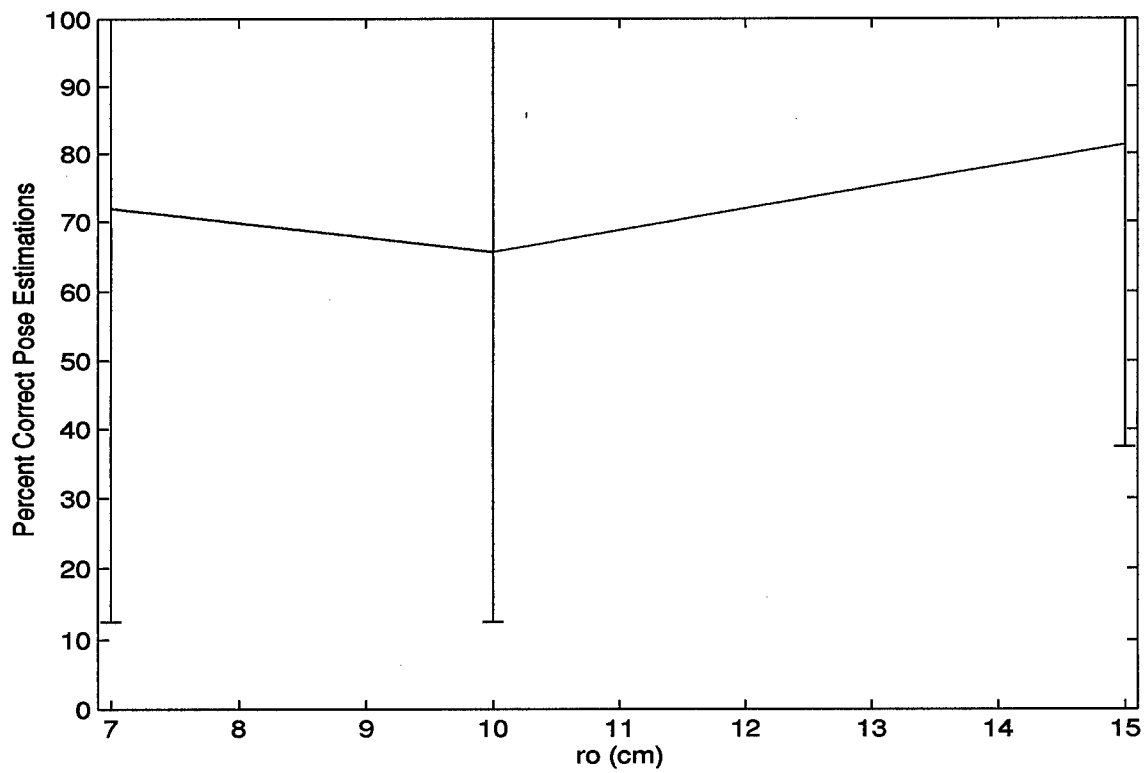
Figure 34. Correct Pose Estimation as a Function of r_o: Case 4
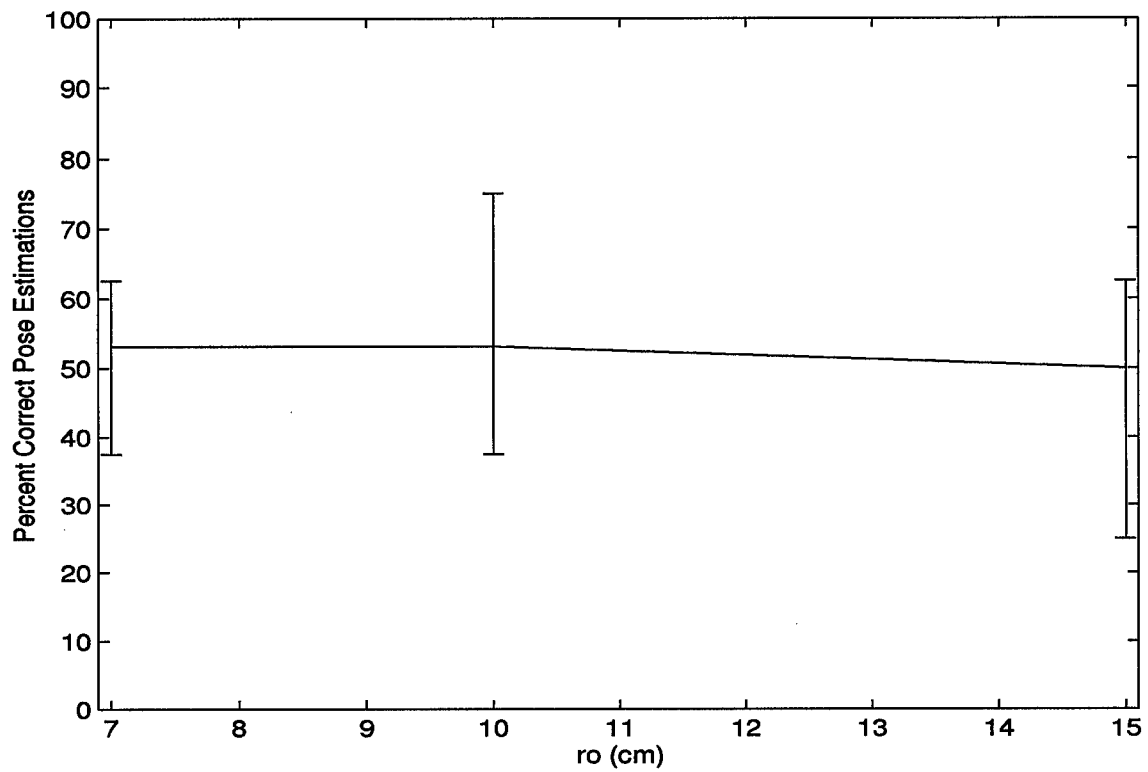
Figure 35. Correct Pose Estimation as a Function of r_o: Case 5
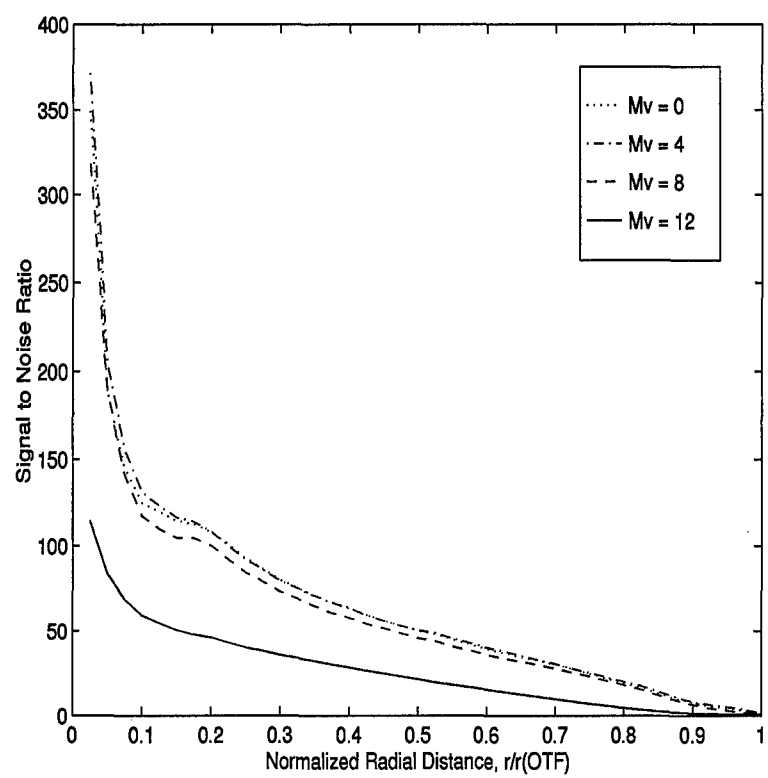
Figure 36. Radially Averaged SNR as a Function of M_v

permanent loss of this information during deconvolution. Visual magnitude is shown to be the key factor in determining the utility of the matched filter for satellite pose estimation. This is best captured in Figures 37 through 41, which show the average occurrence of correct outputs from the matched filter as a function of visual magnitude for each algorithm considered.

It is apparent that visual magnitude is an extremely strong contributor to the effectiveness of the matched filter. The error bars show a trend of slightly improved performance for higher values of r_o. All of the algorithms examined show a dramatic decrease in performance with a decrease in photon flux. As with r_o, the application of the Sobel edge map to the deconvolved image shows the best overall results. It is important to note that the application of the median filter provides a margin of improvement at a visual magnitude of 12. The median filter method resulted in a 33.3 percent rate of correct pose estimations compared to the 20.8 percent rate for the Sobel/Deconvolution approach at this light level.

4.3 Weighted Utilities of the Matched Filter Algorithms

The effects of atmospheric turbulence and light levels on the effectiveness of the matched filter for pose estimation are clearly defined by the previous two sections. This section describes the relative occurrence rates of the visual magnitude and turbulence level combinations considered in this study. Additionally, it describes a method for quantifying the utility of each matched filter algorithm. By combining this information, the weighted utilities associated with each of the five matched filter algorithms are described.

4.3.1 Combined Occurrence Rates for r_o and M_v. To perform a more realistic determination of the utility of the matched filter for the pose estimation problem, the relative occurrence rates of these events must be considered when assessing the relative effectiveness of the algorithms studied. To accomplish this, historical data

73
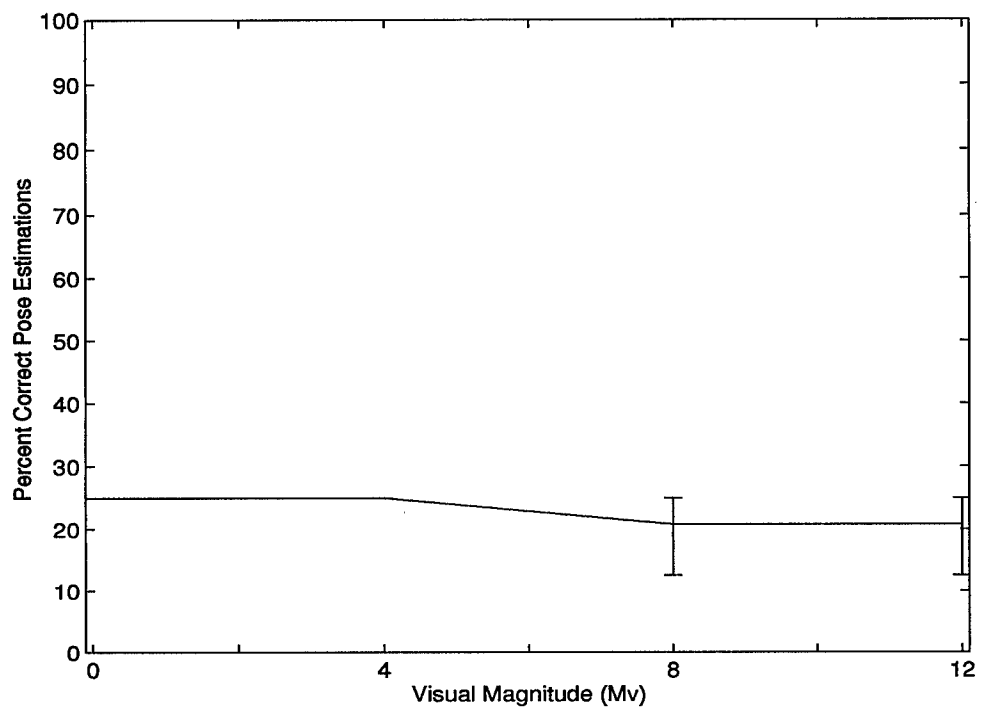
Figure 37. Correct Pose Estimation as a Function of M_v: Case 1
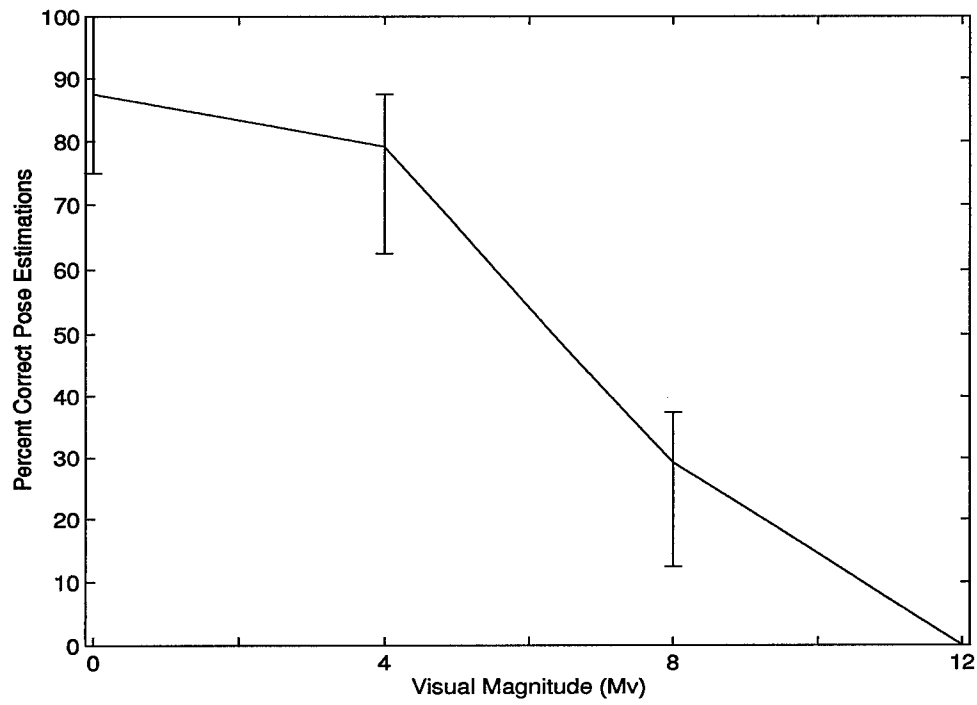
Figure 38. Correct Pose Estimation as a Function of M_v: Case 2

74
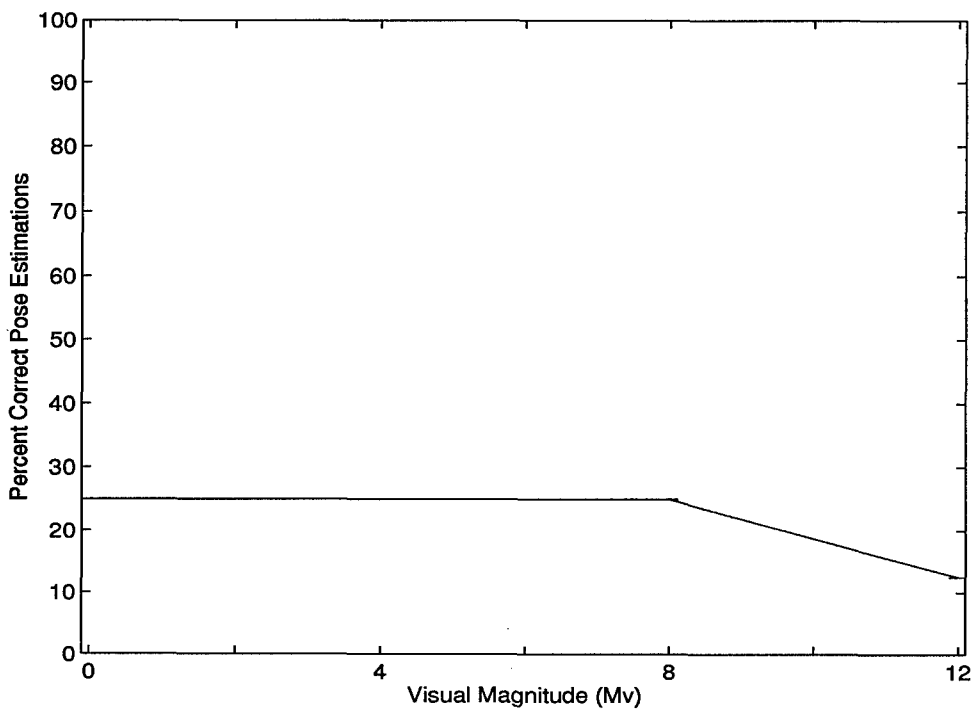
Figure 39. Correct Pose Estimation as a Function of M_v: Case 3
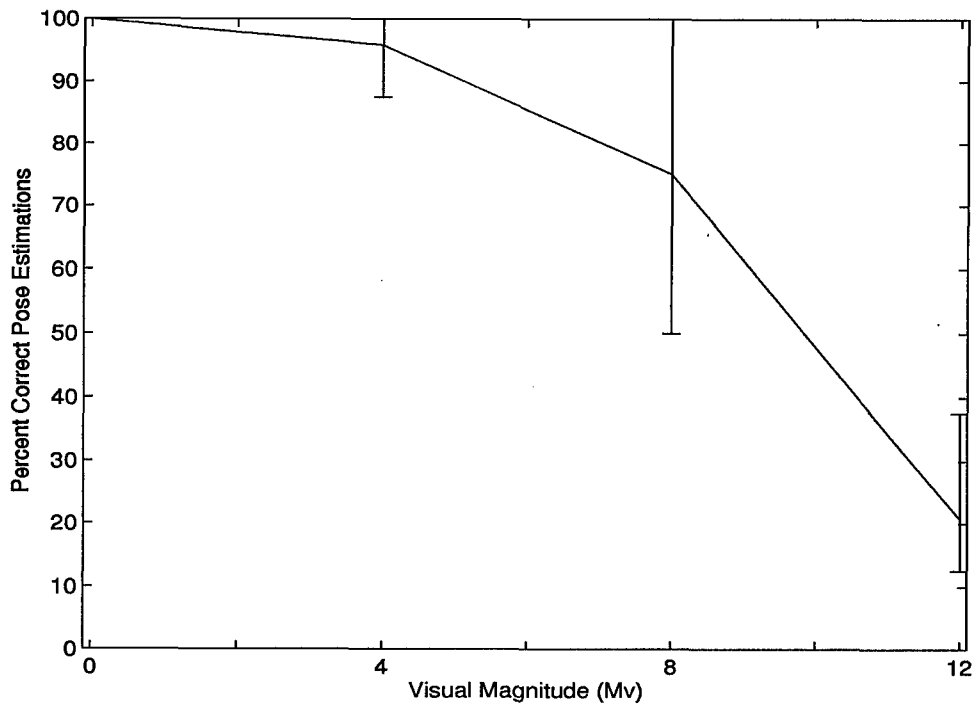
Figure 40. Correct Pose Estimation as a Function of M_v: Case 4

75
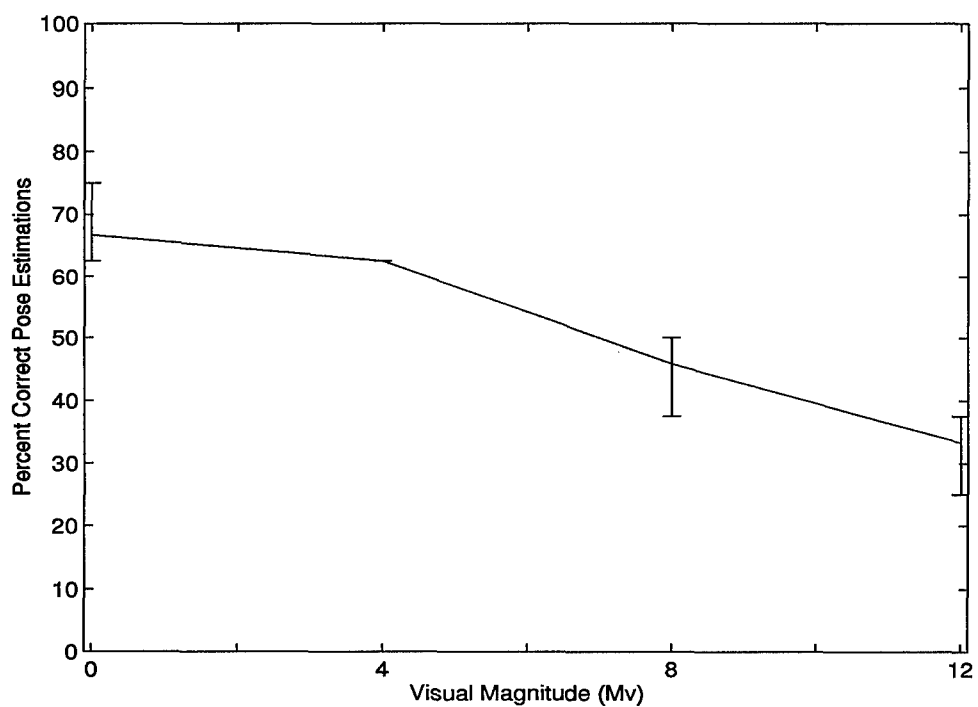
Figure 41. Correct Pose Estimation as a Function of M_v: Case 5

	l	s
r_o	9.79	1.41
M_v	5.37	0.94

Table 11. Parameters Defining the Logistic Probability Distribution for r_o and M_v

was obtained from the Air Force Maui Optical Station (AMOS) regarding both the turbulence levels and visual magnitudes that are encountered when imaging LEO satellites (2). This historical data yielded a probability distribution for both turbulence and light levels. Histograms of this data are shown in Figures 12 and 13 in Section 3.4 of this report.

Using this data, probability distributions for both M_v and r_o were established. These results are based on the output of the Best Fit statistical analysis software package using a Chi-squared test for fit. Both M_v and r_o were found to be sufficiently modeled with the Logistic probability distribution. The Logistic distribution is defined mathematically by Equation 37 (17:289)

$$P_{logistic}(x, l, s) = \frac{e^{((l-x)/s)}}{s(1 + e^{(l-x)/s})^2},$$
(37)

where l and s are the mean of the data and a scaling parameter, respectively. The data from Maui was fit to Logistic probability distributions defined by Table 11. Figure 42 is a graphical representation to the probability distributions for r_o and M_v as defined by Equation 37 and Table 11.

From this information, the probability associated with each of the twelve combinations of M_v and r_o values can be established (18:51). For two independent events, A and B, the probability of their intersection is given by Equation 38.

$$P(A \cap B) = P(A) \cdot P(B)$$
(38)

Based on Equation 38, it is possible to generate the probabilities for each possible combination of r_o and M_v from the independent distributions defined in Equation 37.
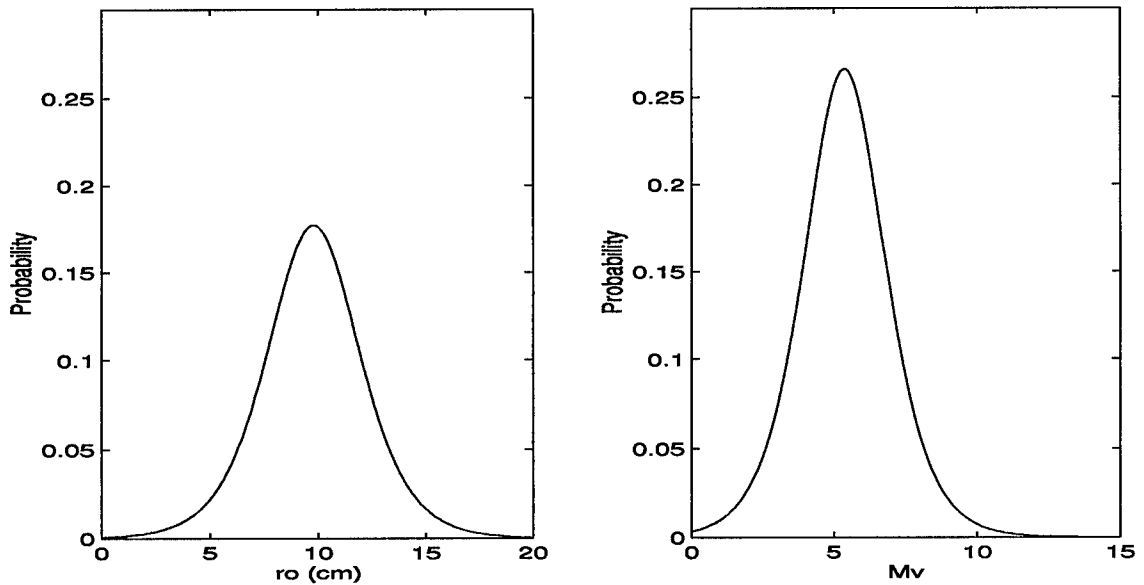
Figure 42. Probability Distributions for r_o and M_v

	$M_v = 0$	$M_v = 4$	$M_v = 8$	$M_v = 12$
$r_o = 7cm$	0.000228	0.012388	0.004408	0.000076
$r_o = 10cm$	0.000528	0.028688	0.010208	0.000176
$r_o = 15cm$	0.000051	0.002771	0.000986	0.000017

Table 12. Probabilities of r_o,M_v Combinations Considered in this Thesis

These probabilities are depicted in Figure 43. The probability associated with each seeing condition considered in this thesis, using the Logistic probability distributions for r_o and M_v, is given in Table 12.

Based on the probabilities in Table 12, it is possible to determine a relative occurrence rate for each seeing condition considered in this study. These relative occurrence rates are linearly proportional to the probability associated with each seeing condition and are defined in a manner such that they sum to unity. The sum of the probabilities in Table 12 is calculated. Each probability in Table 12 is divided by this sum to yield the relative occurrence rates given in Table 13. Note that the values given in this table are rounded.

78
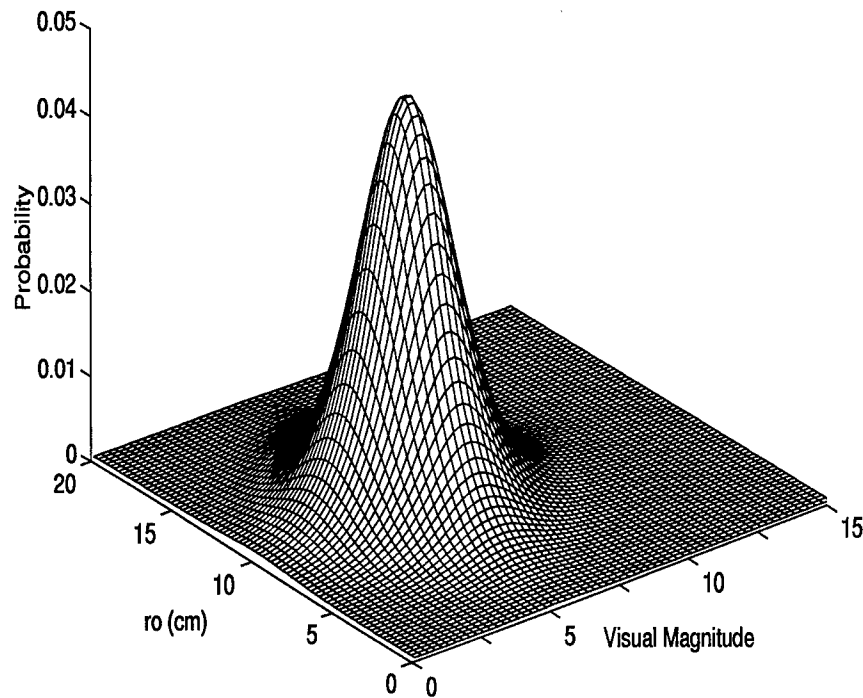
Figure 43. Probabilities of Combinations of r_o and M_v

	$M_v = 0$	$M_v = 4$	$M_v = 8$	$M_v = 12$
$r_o = 7cm$	0.004	0.205	0.073	0.001
$r_o = 10cm$	0.009	0.474	0.169	0.003
$r_o = 15cm$	0.001	0.046	0.015	0.000

Table 13. Relative Occurrence Rates of Seeing Conditions Considered in this Thesis

4.3.2 Determination of Weighted Utilities. Using the information presented above, it is possible to define weighted utilities for each matched filter algorithm considered. In this study, utilities related to the percentage of correct pose estimations and the average correlation between actual and predicted poses for each matched filter algorithm are considered. The weighted utility value is a quantitative means for examining the relative performance of each of the matched filter algorithms. Because it is based on the actual seeing conditions encountered in space surveillance operations at AMOS, it provides an indication of the relative likelihood of correct pose estimations that are possible with each algorithm.

4.3.2.1 Weighted Utility for the Percentage of Correct Pose Estimations. For each algorithm, the percentage of correct pose estimations for each r_o, M_v combination defined in Table 6 was calculated. This information is depicted in Figures 25 through 29. The percentage of correct pose estimations for each combination, *a* through *l*, was multiplied by the corresponding relative occurrence rate from Table 13. This was accomplished for each algorithm, both with and without symmetry errors included as correct pose estimations. For each algorithm, the weighted percentage utility value is the sum of these products. This is described mathematically by

$$U = R_a C_a + R_b C_b + \ldots + R_l C_l, \tag{39}$$

where U represents the weighted utility value, R represents the relative occurrence rate associated with each seeing condition, and C represents the percentage of correct pose estimations under the appropriate seeing condition. The weighted percentage utility values are summarized in Figure 44.

4.3.2.2 Weighted Correlation Utilities. In a similar manner, a weighted average correlation utility value was calculated. The weighted average correlation utility provides a relative measure of the expected strength of correlation between the actual and predicted pose. A high numeric value indicates that errors in pose
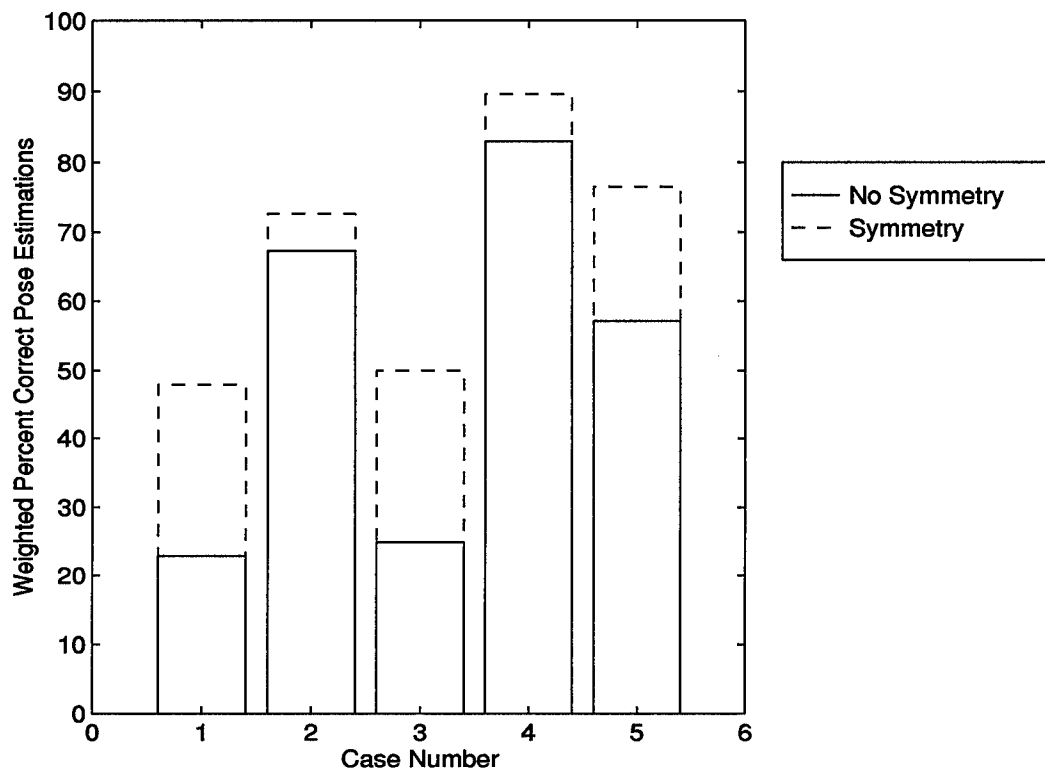
Figure 44. Weighted Percentage Utilities for Each Matched Filter Algorithm
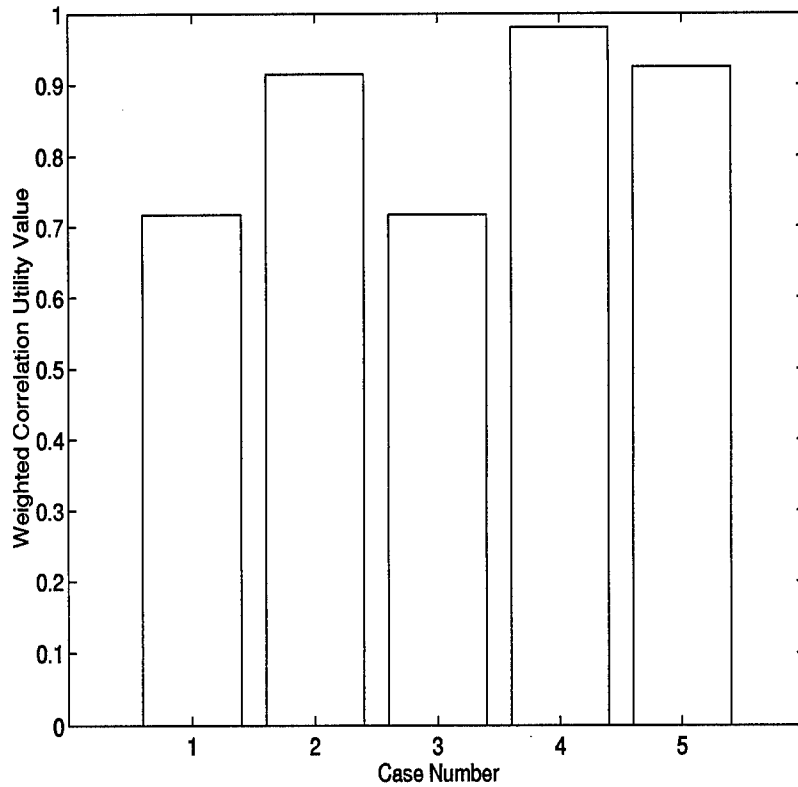
Figure 45. Weighted Correlation Utility Values

estimation will likely be between two poses that have very similar appearances, such as rotations about an axis of symmetry.

For each matched filter algorithm, the mean correlation values from Appendix B for each seeing condition were multiplied by the appropriate relative occurrence rate from Table 13. The sum of these products for each algorithm is the weighted correlation utility value. Mathematically, this is described by Equation 39 with C representing the mean correlation value associated with each seeing condition. The results are given in Figure 45.

4.3.2.3 Results of the Weighted Utility Analysis. The weighted utility functions are not intended to precisely describe the percentage of correct pose esti-

mations that are possible with a given algorithm. This could only be accomplished in the laboratory using techniques such as Monte Carlo simulation. Because of the time involved in creating a large database of aberrated images under the necessary seeing conditions, this approach is not feasible in the time frame allotted for this thesis effort. Instead, the approach used in this study demonstrates the relative effectiveness of each algorithm under actual operational conditions. These weighted utilities, however, will provide a first order approximation to the percentages of correct pose estimations that might be expected when using a Monte Carlo simulation. The results indicate that the application of the Sobel edge map to a deconvolved image before applying the matched filter will yield the most accurate pose estimations under normal operating conditions.

4.4 Summary

This chapter has presented the results of the matched filter algorithms considered in this study. It has shown the overall accuracy of each algorithm under a variety of seeing conditions. Additionally, an analysis of the effects of atmospheric turbulence levels and target visual magnitudes has been presented. The results of this analysis were then used in combination with historical data from the Air Force Maui Optical Station to develop a weighted likelihood of correct pose estimation for each algorithm considered. The following chapter utilizes this information to draw conclusions regarding the utility of the use of the matched filter to the satellite pose estimation problem.

V. Conclusion and Recommendations for Future Research

The main objective of this research effort was to examine the limitations on the use of the matched filter for the satellite pose estimation problem. This objective was motivated by the need to establish a solid foundation for future research in this field. In doing this, it has been possible to examine several derivatives of the basic matched filter algorithm.

Chapter I of this thesis described the problem, presented the current level of knowledge in this arena, defined the scope of this effort, and outlined the approach that was taken. In Chapter II, the relevant theory from the fields of pattern recognition and imaging through turbulence were presented. The methodology applied in this research effort was outlined in Chapter III. Performance results for each matched filter algorithm were presented in detail in Chapter IV. In this chapter, the key accomplishments of this effort are highlighted and conclusions are drawn from this work. Perhaps even more importantly, recommendations for future research in this area are offered.

5.1 Summary of Research Advancements

This thesis represents the first major effort to quantify the utility of a pose estimation algorithm as a function of atmospheric turbulence levels and target visual magnitude. Other approaches, such as neural networks, are presently being studied as a solution to the pose estimation problem. The research presented in this thesis has defined a benchmark to which future research efforts can be compared. Borrowing from the concept "appearance matching" proposed by Murase and Nayer (19:6), this thesis has attempted to include all of the significant variables in the study of satellite pose estimation, rather than focusing solely on geometric correlations.

Additionally, this work has evaluated five different matched filter algorithms under the same range of seeing condition variables. A weighted utility function was

developed to measure the relative performance of each matched filter algorithm. This function accounts for the actual seeing conditions encountered at AMOS. In doing so, this thesis has been able to define an algorithm with a high probability of correct pose estimation under actual operational conditions.

5.2 Summary of Results Obtained

Satellite pose estimation experiments were conducted under a wide range of seeing conditions, utilizing five different matched filter algorithms. The key results obtained are summarized below:

- Visual magnitude is the single most important aspect of seeing conditions when estimating the pose of a LEO satellite. Above visual magnitudes of approximately 8, the accuracy of the pose estimation routine diminishes significantly.

- When utilizing partially compensated adaptive optics, the effects from atmospheric turbulence on the pose estimation routines considered are minimal. r_o was shown to contribute to the pose estimation problem. Slightly better performance is achieved with increases in r_o. The pose estimation routine defined in this thesis is more highly dependent upon visual magnitude.

- For imagery of objects at extremely low light levels, the application of standard image processing techniques such as the median filter before the application of the matched filter can yield some improvement in the results. Significant improvements were noted in this study when the median filter was applied to imagery with $M_v = 12$.

- The use of hybrid imaging techniques such as deconvolution is an essential part of the pose estimation algorithm.

- A significant portion of the erroneous pose estimations encountered were due to symmetry in the target. In general, these errors are more common with increasing visual magnitudes. This indicates that a solution to this problem

may arise as methods are developed to further improve the signal to noise ratio in the target image.

5.3 Conclusions Drawn from Research

Satellite imagery collected by operational facilities is obtained under a wide range of seeing conditions. The utility of a pose estimation algorithm must be weighted to include the entire range of conditions that can realistically be experienced. A high degree of confidence can be achieved for a matched filter algorithm applied to the pose estimation problem. Using deconvolution of partially compensated imagery techniques, a high utility can be achieved when a Sobel edge map of the deconvolved target image is used as the input to the matched filter.

5.4 Recommendations for Future Research

This thesis effort focused on developing an algorithm to determine the pose of a LEO satellite consistently under a wide range of seeing conditions. No attempt was made to determine the degree of precision in pose estimation that can be attained by the matched filter algorithm. Other research efforts, such as that presented by Chang and Hoepner (6:18), indicate accuracies within one degree of error in pose estimation. Other pose estimation techniques in the literature fail to account for variables such as visual magnitude. Future research should consider the precision that can be attained as a function of seeing conditions for the matched filter and other pose estimation routines.

Significant decreases in performance at high visual magnitudes are likely due to the low signal to noise ratio in the target images. Using deconvolution on images with low values of SNR results in a significant loss of high spatial frequency information, resulting in blurred imagery. This introduces a probability of error when using the Sobel edge map of the target image to approximate the Sobel edge map of an image in the known image database.

Some relief from this difficulty may be obtained by applying more sophisticated edge detection techniques, such as those discussed in Section 2.1.2.1 by Law (14) and Qian (12). Future efforts should focus on improving the SNR in the target image. This will yield sharper images, thus providing more accurate edge maps. Improvements in SNR should reduce the number of errors due to satellite symmetry.

As with any database search routine, the matched filter technique for satellite pose estimation is computationally expensive. Gavrila (10:1) has examined a method of speeding up correlation algorithms that utilize databases of edge map images. His research focuses on phase coded filtering techniques which combine multiple patterns in one filter by assigning complex weights of unit magnitude to the individual patterns and summing them in a composite filter. This approach first applies an inexpensive matching technique to determine a likely subset of the known image database that will likely contain the target image. More intensive correlation methods are applied to this subset of the known database. Phase coded matching is subject to many of the same limitations as correlation based techniques, but is much faster. It is shown to be an effective method of reducing the known image database to a size that can be handled by the more common correlation algorithms.

5.5 Summary

Based on the results obtained in this research effort, it is apparent that the matched filter is a viable method for determining the pose of a LEO satellite. The information contained in this thesis clearly outlines the limitations imposed on its effectiveness by the range of seeing conditions that are encountered in an actual operational environment. Further research must be done to define the degree of precision in pose estimation that can be achieved under actual seeing conditions. Improved results can be expected as methods are developed to improve the signal to noise ratio in satellite surveillance imagery. Additionally, efforts should be made to examine ways to speed up the correlation algorithm.

By defining a pose estimation algorithm with proven effectiveness over the range of seeing conditions that are normally encountered in ground based space surveillance operations, this study has made a significant contribution to the field and has successfully provided the framework from which future research can originate. In doing so, the objectives of this research effort have been achieved.

Appendix A.

For each satellite, the name of the satellite in the table represents the pose that was predicted by the matched filter. A * indicates that the matched filter correctly identified the pose of the target. Within this appendix, each matched filter algorithm is referred to by a case number. These case numbers are defined in Table 7.

	$r_o = .07$	$r_o = .10$	$r_o = .15$
$Mv = 0$	*	*	*
$Mv = 4$	*	*	*
$Mv = 8$	*	*	*
$Mv = 12$	*	*	*

Table 14. Case 1 Results, Input c30n150

	$r_o = .07$	$r_o = .10$	$r_o = .15$
$Mv = 0$	c45p180	c45p180	c45p180
$Mv = 4$	c45p180	c45p180	c45p180
$Mv = 8$	c45p180	c45p180	c45p180
$Mv = 12$	c45p180	c45p180	c45p180

Table 15. Case 1 Results, Input c45p0

	$r_o = .07$	$r_o = .10$	$r_o = .15$
$Mv = 0$	*	*	*
$Mv = 4$	*	*	*
$Mv = 8$	*	c60p120	*
$Mv = 12$	c60p120	*	*

Table 16. Case 1 Results, Input c60p60

	$r_o = .07$	$r_o = .10$	$r_o = .15$
$Mv = 0$	d30p90	d30p90	d30p90
$Mv = 4$	d30p90	d30p90	d30p90
$Mv = 8$	d30p90	d30p90	d30p90
$Mv = 12$	d30p90	d30p90	d30p90

Table 17. Case 1 Results, Input d30p120

	$r_o = .07$	$r_o = .10$	$r_o = .15$
$Mv = 0$	d45p90	d45p90	d45p90
$Mv = 4$	d45p90	d45p90	d45p90
$Mv = 8$	d45p90	d45p90	d45p90
$Mv = 12$	d45p90	d45p90	d45p90

Table 18. Case 1 Results, Input d45n30

	$r_o = .07$	$r_o = .10$	$r_o = .15$
$Mv = 0$	d60p90	d60p90	d60p90
$Mv = 4$	d60p90	d60p90	d60p90
$Mv = 8$	d60p90	d60p90	d60p90
$Mv = 12$	d60p90	d60p90	d60p90

Table 19. Case 1 Results, Input d60p180

	$r_o = .07$	$r_o = .10$	$r_o = .15$
$Mv = 0$	o45n60	o45n60	o45n60
$Mv = 4$	o45n60	o45n60	o45n60
$Mv = 8$	o45n60	o45n60	o45n60
$Mv = 12$	o45n60	o45n60	o45n60

Table 20. Case 1 Results, Input o30n60

	$r_o = .07$	$r_o = .10$	$r_o = .15$
$Mv = 0$	o45n90	o45n90	o45n90
$Mv = 4$	o45n90	o45n90	o45n90
$Mv = 8$	o45n90	o45n90	o45n90
$Mv = 12$	o45n90	o45n90	o45n90

Table 21. Case 1 Results, Input o45p90

	$r_o = .07$	$r_o = .10$	$r_o = .15$
$Mv = 0$	c30p30	c30n30	*
$Mv = 4$	c30p30	c30p150	*
$Mv = 8$	c30p150	*	*
$Mv = 12$	c30p0	c30p0	c30p0

Table 22. Case 2 Results, Input c30n150

	$r_o = .07$	$r_o = .10$	$r_o = .15$
$Mv = 0$	*	c30n30	*
$Mv = 4$	*	*	*
$Mv = 8$	c45n150	c45n150	c45n150
$Mv = 12$	c30p0	c30p0	c30p0

Table 23. Case 2 Results, Input c45p0

	$r_o = .07$	$r_o = .10$	$r_o = .15$
$Mv = 0$	*	*	*
$Mv = 4$	c60n60	*	c60n60
$Mv = 8$	c60n150	c60p150	c60n30
$Mv = 12$	c45p180	c45n150	c60n150

Table 24. Case 2 Results, Input c60p60

	$r_o = .07$	$r_o = .10$	$r_o = .15$
$Mv = 0$	*	*	*
$Mv = 4$	*	*	*
$Mv = 8$	*	*	*
$Mv = 12$	d30n120	d30n60	d30n120

Table 25. Case 2 Results, Input d30p120

	$r_o = .07$	$r_o = .10$	$r_o = .15$
$Mv = 0$	*	*	*
$Mv = 4$	*	*	*
$Mv = 8$	d45n60	d45n60	d45n60
$Mv = 12$	d45n60	d45n60	d45n60

Table 26. Case 2 Results, Input d45n30

	$r_o = .07$	$r_o = .10$	$r_o = .15$
$Mv = 0$	*	*	*
$Mv = 4$	*	*	*
$Mv = 8$	d45p120	d30p120	*
$Mv = 12$	d30p120	d30p120	d30p120

Table 27. Case 2 Results, Input d60p180

	$r_o = .07$	$r_o = .10$	$r_o = .15$
$Mv = 0$	*	*	*
$Mv = 4$	*	*	*
$Mv = 8$	o45n60	*	o45n150
$Mv = 12$	o45n150	o45n60	o45n60

Table 28. Case 2 Results, Input o30n60

	$r_o = .07$	$r_o = .10$	$r_o = .15$
$Mv = 0$	*	*	*
$Mv = 4$	o45n90	*	*
$Mv = 8$	o45n150	o45n150	o45n90
$Mv = 12$	o45n150	o45n150	o45n150

Table 29. Case 2 Results, Input o45p90

	$r_o = .07$	$r_o = .10$	$r_o = .15$
$Mv = 0$	*	*	*
$Mv = 4$	*	*	*
$Mv = 8$	*	*	*
$Mv = 12$	*	*	*

Table 30. Case 3 Results, Input c30n150

	$r_o = .07$	$r_o = .10$	$r_o = .15$
$Mv = 0$	c45p180	c45p180	c45p180
$Mv = 4$	c45p180	c45p180	c45p180
$Mv = 8$	c45p180	c45p180	c45p180
$Mv = 12$	c45p180	c45p180	c45p180

Table 31. Case 3 Results, Input c45p0

	$r_o = .07$	$r_o = .10$	$r_o = .15$
$Mv = 0$	*	*	*
$Mv = 4$	*	*	*
$Mv = 8$	*	*	*
$Mv = 12$	c60p120	c60p120	c60p120

Table 32. Case 3 Results, Input c60p60

	$r_o = .07$	$r_o = .10$	$r_o = .15$
$Mv = 0$	d30p90	d30p90	d30p90
$Mv = 4$	d30p90	d30p90	d30p90
$Mv = 8$	d30p90	d30p90	d30p90
$Mv = 12$	d30p90	d30p90	d30p90

Table 33. Case 3 Results, Input d30p120

	$r_o = .07$	$r_o = .10$	$r_o = .15$
$Mv = 0$	d45p90	d45p90	d45p90
$Mv = 4$	d45p90	d45p90	d45p90
$Mv = 8$	d45p90	d45p90	d45p90
$Mv = 12$	d45p90	d45p90	d45p90

Table 34. Case 3 Results, Input d45n30

	$r_o = .07$	$r_o = .10$	$r_o = .15$
$Mv = 0$	d60p90	d60p90	d60p90
$Mv = 4$	d60p90	d60p90	d60p90
$Mv = 8$	d60p90	d60p90	d60p90
$Mv = 12$	d60p90	d60p90	d60p90

Table 35. Case 3 Results, Input d60p180

	$r_o = .07$	$r_o = .10$	$r_o = .15$
$Mv = 0$	o45n60	o45n60	o45n60
$Mv = 4$	o45n60	o45n60	o45n60
$Mv = 8$	o45n60	o45n60	o45n60
$Mv = 12$	o45n60	o45n60	o45n60

Table 36. Case 3 Results, Input o30n60

	$r_o = .07$	$r_o = .10$	$r_o = .15$
$Mv = 0$	o45n90	o45n90	o45n90
$Mv = 4$	o45n90	o45n90	o45n90
$Mv = 8$	o45n90	o45n90	o45n90
$Mv = 12$	o45n90	o45n90	o45n90

Table 37. Case 3 Results, Input o45p90

	$r_o = .07$	$r_o = .10$	$r_o = .15$
$Mv = 0$	*	*	*
$Mv = 4$	*	c30p150	c30p30
$Mv = 8$	*	c30p30	*
$Mv = 12$	c30p150	c30p0	*

Table 38. Case 4 Results, Input c30n150

	$r_o = .07$	$r_o = .10$	$r_o = .15$
$Mv = 0$	*	*	*
$Mv = 4$	*	*	*
$Mv = 8$	c45p180	*	*
$Mv = 12$	c45p180	c45p180	*

Table 39. Case 4 Results, Input c45p0

	$r_o = .07$	$r_o = .10$	$r_o = .15$
$Mv = 0$	*	*	*
$Mv = 4$	*	*	*
$Mv = 8$	*	c60n60	*
$Mv = 12$	c60p0	c60p0	c60p0

Table 40. Case 4 Results, Input c60p60

	$r_o = .07$	$r_o = .10$	$r_o = .15$
$Mv = 0$	*	*	*
$Mv = 4$	*	*	*
$Mv = 8$	*	*	*
$Mv = 12$	*	*	*

Table 41. Case 4 Results, Input d30p120

	$r_o = .07$	$r_o = .10$	$r_o = .15$
$Mv = 0$	*	*	*
$Mv = 4$	*	*	*
$Mv = 8$	*	d45n60	*
$Mv = 12$	d45n60	d45n60	d45n60

Table 42. Case 4 Results, Input d45n30

	$r_o = .07$	$r_o = .10$	$r_o = .15$
$Mv = 0$	*	*	*
$Mv = 4$	*	*	*
$Mv = 8$	*	*	*
$Mv = 12$	d45p120	d45p120	d45p120

Table 43. Case 4 Results, Input d60p180

	$r_o = .07$	$r_o = .10$	$r_o = .15$
$Mv = 0$	*	*	*
$Mv = 4$	*	*	*
$Mv = 8$	*	o30n150	*
$Mv = 12$	o45n150	o45n60	o45n60

Table 44. Case 4 Results, Input o30n60

	$r_o = .07$	$r_o = .10$	$r_o = .15$
$Mv = 0$	*	*	*
$Mv = 4$	*	*	*
$Mv = 8$	o45n90	*	*
$Mv = 12$	o45n150	o45n90	o45p150

Table 45. Case 4 Results, Input o45p90

	$r_o = .07$	$r_o = .10$	$r_o = .15$
$Mv = 0$	c30p30	c30p30	c30p30
$Mv = 4$	c30p150	c30p30	c30p30
$Mv = 8$	*	c30p30	c30p30
$Mv = 12$	*	*	c30p150

Table 46. Case 5 Results, Input c30n150

	$r_o = .07$	$r_o = .10$	$r_o = .15$
$Mv = 0$	*	*	*
$Mv = 4$	*	*	*
$Mv = 8$	c45p180	*	c45p180
$Mv = 12$	*	c45n150	c45p180

Table 47. Case 5 Results, Input c45p0

	$r_o = .07$	$r_o = .10$	$r_o = .15$
$Mv = 0$	c60n60	*	*
$Mv = 4$	c60n60	*	c60n60
$Mv = 8$	c60n60	c60n60	*
$Mv = 12$	c60p150	c60p150	c60n120

Table 48. Case 5 Results, Input c60p60

	$r_o = .07$	$r_o = .10$	$r_o = .15$
$Mv = 0$	*	*	*
$Mv = 4$	*	*	*
$Mv = 8$	*	*	*
$Mv = 12$	*	*	*

Table 49. Case 5 Results, Input d30p120

	$r_o = .07$	$r_o = .10$	$r_o = .15$
$Mv = 0$	*	*	*
$Mv = 4$	*	*	*
$Mv = 8$	*	d45n60	*
$Mv = 12$	d45n60	d45n60	d45n60

Table 50. Case 5 Results, Input d45n30

98

	$r_o = .07$	$r_o = .10$	$r_o = .15$
$Mv = 0$	*	*	*
$Mv = 4$	*	*	*
$Mv = 8$	*	*	*
$Mv = 12$	d45p120	d30p120	d45p120

Table 51. Case 5 Results, Input d60p180

	$r_o = .07$	$r_o = .10$	$r_o = .15$
$Mv = 0$	*	o45n150	o45n150
$Mv = 4$	o45n150	o45n150	o45n150
$Mv = 8$	o45n150	o45n150	o45n150
$Mv = 12$	o45n150	o45n60	o45n150

Table 52. Case 5 Results, Input o30n60

	$r_o = .07$	$r_o = .10$	$r_o = .15$
$Mv = 0$	o45n90	*	o45n90
$Mv = 4$	*	o45n90	*
$Mv = 8$	o45n90	o45n90	o45n90
$Mv = 12$	o45n150	o45n90	o45n90

Table 53. Case 5 Results, Input o45p90

Appendix B.

This appendix contains the correlation values between the actual input images and the pose estimation that resulted from the use of each of the matched filter algorithms. The r_o and M_v combinations are defined in Table 6.

	a	b	c	d	e	f	g	h	i	j	k	l
c30n150	1	1	1	1	1	1	1	1	1	1	1	1
c45p0	0.9893	0.9893	0.9893	0.9893	0.9893	0.9893	0.9893	0.9893	0.9893	0.9893	0.9893	0.9893
c60p60	1	1	1	0.9867	1	1	0.9867	1	1	1	1	1
d30p120	0.5427	0.5427	0.5427	0.5427	0.5427	0.5427	0.5427	0.5427	0.5427	0.5427	0.5427	0.5427
d45n30	0.3593	0.3593	0.3593	0.3593	0.3593	0.3593	0.3593	0.3593	0.3593	0.3593	0.3593	0.3593
d60p180	0.3181	0.3181	0.3181	0.3181	0.3181	0.3181	0.3181	0.3181	0.3181	0.3181	0.3181	0.3181
o30n60	0.6757	0.6757	0.6757	0.6757	0.6757	0.6757	0.6757	0.6757	0.6757	0.6757	0.6757	0.6757
o45p90	0.8553	0.8553	0.8553	0.8553	0.8553	0.8553	0.8553	0.8553	0.8553	0.8553	0.8553	0.8553
MEAN	0.7176	0.7176	0.7176	0.7159	0.7176	0.7176	0.7159	0.7176	0.7176	0.7176	0.71755	0.7176

Table 54. Case 1 Correlation Values

	a	b	c	d	e	f	g	h	i	j	k	l
c30n150	0.9878	0.9878	0.9558	0.7796	0.9660	0.9558	1	0.7796	1	1	1	0.7796
c45p0	1	1	0.7615	0.7098	0.6466	1	0.7615	0.7098	1	1	0.7615	0.7098
c60p60	1	0.9841	0.7561	0.5113	1	1	0.7552	0.5261	1	0.9841	0.7693	0.7561
d30p120	1	1	1	0.8539	1	1	1	0.3109	1	1	1	0.8539
d45n30	1	1	0.6700	0.6700	1	1	0.6700	0.6700	1	1	0.6700	0.6700
d60p180	1	1	0.2506	0.2077	1	1	0.2077	0.2077	1	1	1	0.2077
o30n60	1	1	0.6757	0.5920	1	1	1	0.6757	1	1	0.5920	0.6757
o45p90	1	0.8553	0.3051	0.3051	1	1	0.3051	0.3051	1	1	0.8553	0.3051
MEAN	0.9985	0.9784	0.6719	0.5787	0.9516	0.9945	0.7123	0.5231	1	0.9980	0.8310	0.6197

Table 55. Case 2 Correlation Values

	a	b	c	d	e	f	g	h	i	j	k	l
c30n150	1	1	1	1	1	1	1	1	1	1	1	1
c45p0	0.9893	0.9893	0.9893	0.9893	0.9893	0.9893	0.9893	0.9893	0.9893	0.9893	0.9893	0.9893
c60p60	1	1	1	0.9867	1	1	0.9867	1	1	1	1	0.9867
d30p120	0.5427	0.5427	0.5427	0.5427	0.5427	0.5427	0.5427	0.5427	0.5427	0.5427	0.5427	0.5427
d45n30	0.3593	0.3593	0.3593	0.3593	0.3593	0.3593	0.3593	0.3593	0.3593	0.3593	0.3593	0.3593
d60p180	0.3181	0.3181	0.3181	0.3181	0.3181	0.3181	0.3181	0.3181	0.3181	0.3181	0.3181	0.3181
o30n60	0.6757	0.6757	0.6757	0.6757	0.6757	0.6757	0.6757	0.6757	0.6757	0.6757	0.6757	0.6757
o45p90	0.8553	0.8553	0.8553	0.8553	0.8553	0.8553	0.8553	0.8553	0.8553	0.8553	0.8553	0.8553
MEAN	0.7176	0.7176	0.7176	0.7159	0.7176	0.7176	0.7176	0.7159	0.7176	0.7176	0.7176	0.7159

Table 56. Case 3 Correlation Values

	a	b	c	d	e	f	g	h	i	j	k	l
c30n150	1	1	1	0.7702	1	1	0.9878	0.7796	1	0.9878	1	1
c45p0	1	1	0.9893	0.9893	1	1	1	0.9893	1	1	1	1
c60p60	1	1	1	0.5977	1	1	0.7693	0.5977	1	1	1	0.5977
d30p120	1	1	1	1	1	1	1	1	1	1	1	1
d45n30	1	1	1	0.6700	1	1	0.6700	0.6700	1	1	1	0.6700
d60p180	1	1	1	0.2506	1	1	1	0.2077	1	1	1	0.2506
o30n60	1	1	1	0.5920	1	1	0.7911	0.6757	1	1	1	0.6757
o45p90	1	1	0.8553	0.3051	1	1	1	0.8553	1	1	1	0.3043
MEAN	1	1	0.9806	0.6469	1	1	0.9023	0.7219	1	0.9985	1	0.6873

Table 57. Case 4 Correlation Values

	a	b	c	d	e	f	g	h	i	j	k	l
c30n150	0.9878	0.9878	1	1	0.9878	0.9878	0.9878	1	0.9878	0.9878	0.9878	0.9558
c45p0	1	1	0.9893	1	1	1	1	0.7615	1	1	0.9893	0.9893
c60p60	0.9841	0.9841	0.9841	0.7552	1	1	0.9841	0.7552	1	0.9841	1	0.9937
d30p120	1	1	1	1	1	1	1	1	1	1	1	1
d45n30	1	1	1	0.6700	1	1	0.6700	1	1	1	1	1
d60p180	1	1	1	0.4611	1	1	1	0.2077	1	1	1	0.2506
o30n60	1	0.5920	0.5920	0.5920	0.5920	0.5920	0.5920	0.5920	0.5920	0.5920	0.5920	0.5920
o45p90	0.8553	1	0.8553	0.3051	1	0.8553	0.8553	0.8553	0.8553	1	0.8553	0.8553
MEAN	0.9784	0.9415	0.9276	0.7229	0.9475	0.9294	0.8862	0.7819	0.9294	0.9455	0.9281	0.8296

Table 58. Case 5 Correlation Values

Appendix C. Confusion Matrices

This appendix contains the confusion matrices associated with each satellite. It is separated into cases describing the matched filter algorithms used. These cases are identified in Section 7.

Calculated Images	Input Images				
	c30n150	c45p0	c45p180	c60p60	c60p120
c30n150	12	0	0	0	0
c45p0	0	0	0	0	0
c45p180	0	12	0	0	0
c60p60	0	0	0	10	0
c60p120	0	0	0	2	0

Table 59. Confusion Matrix for Chucksat, Case 1

Calculated Images	Input Images					
	d30p90	d30p120	d45n30	d45p90	d60p90	d60p180
d30p90	0	12	0	0	0	0
d30p120	0	0	0	0	0	0
d45n30	0	0	0	0	0	0
d45p90	0	0	12	0	0	0
d60p90	0	0	0	0	0	12
d60p180	0	0	0	0	0	0

Table 60. Confusion Matrix for DMSP, Case 1

Calculated Images	Input Images					
	o30n150	o30n60	o45n90	o45n60	o45p90	o60n120
o30n150	0	0	0	0	0	12
o30n60	0	0	0	0	0	0
o45n90	0	0	0	0	12	0
o45n60	0	12	0	0	0	0
o45p90	0	0	0	0	0	0
o60n120	0	0	0	0	0	0

Table 61. Confusion Matrix for OCNR, Case 1

Calculated Images	Input Images											
	c30n150	c30n30	c30p0	c30p30	c30p150	c45n150	c45p0	c45p180	c60n150	c60n60	c60n30	c60p60
c30n150	4	0	0	0	0	0	0	0	0	0	0	0
c30n30	1	0	0	0	0	0	1	0	0	0	0	0
c30p0	3	0	0	0	0	0	3	0	0	0	0	0
c30p30	2	0	0	0	0	0	0	0	0	0	0	0
c30p150	2	0	0	0	0	0	0	0	0	0	0	0
c45n150	0	0	0	0	0	0	3	0	0	0	0	1
c45p0	0	0	0	0	0	0	5	0	0	0	0	0
c45p180	0	0	0	0	0	0	0	0	0	0	0	1
c60n150	0	0	0	0	0	0	0	0	0	0	0	3
c60n60	0	0	0	0	0	0	0	0	0	0	0	2
c60n30	0	0	0	0	0	0	0	0	0	0	0	1
c60p60	0	0	0	0	0	0	0	0	0	0	0	4

Table 62. Confusion Matrix for Chucksat, Case 2

Calculated Images	Input Images						
	d30n120	d30n6	d30p120	d45n6	d45n3	d45p120	d60p180
d30n120	0	0	2	0	0	0	0
d30n60	0	0	1	0	0	0	0
d30p120	0	0	9	0	0	0	4
d45n60	0	0	0	0	6	0	0
d45n30	0	0	0	0	6	0	0
d45p120	0	0	0	0	0	0	1
d60p180	0	0	0	0	0	0	7

Table 63. Confusion Matrix for DMSP, Case 2

Calculated Images	Input Images							
	o30n60	o45n15	o45n59	o45n6	o45n3	o45p9	o60n12	o60p6
o30n60	7	0	0	0	0	0	0	0
o45n150	2	0	0	0	0	5	1	0
o45n90	0	0	0	0	0	2	0	0
o45n60	3	0	0	0	0	0	0	0
o45n30	0	0	0	0	0	0	5	0
o45p90	0	0	0	0	0	5	0	0
o60n120	0	0	0	0	0	0	2	0
o60p60	0	0	0	0	0	0	4	0

Table 64. Confusion Matrix for OCNR, Case 2

Calculated Images	Input Images				
	c30n150	c45p0	c45p180	c60p60	c60p120
c30n150	12	0	0	0	0
c45p0	0	0	0	0	0
c45p180	0	12	0	0	0
c60p60	0	0	0	9	0
c60p120	0	0	0	3	0

Table 65. Confusion Matrix for Chucksat, Case 3

Calculated Images	Input Images					
	d30p90	d30p120	d45n30	d45p90	d60p90	d60p180
d30p90	0	12	0	0	0	0
d30p120	0	0	0	0	0	0
d45n30	0	0	0	0	0	0
d45p90	0	0	12	0	0	0
d60p90	0	0	0	0	0	12
d60p180	0	0	0	0	0	0

Table 66. Confusion Matrix for DMSP, Case 3

Calculated Images	Input Images					
	o30n60	o30p150	o45n90	045n60	o45p90	o60n120
o30n60	0	0	0	0	0	0
o30p150	0	0	0	0	0	12
o45n90	0	0	0	0	12	0
o45n60	12	0	0	0	0	0
o45p90	0	0	0	0	0	0
o60n120	0	0	0	0	0	0

Table 67. Confusion Matrix for OCNR, Case 3

Calculated Images	Input Images								
	c30n150	c30p0	c30p30	c30p150	c45p0	c45p180	c60n60	c60p0	c60p60
c30n150	7	0	0	0	0	0	0	0	0
c30p0	1	0	0	0	0	0	0	0	0
c30p30	2	0	0	0	0	0	0	0	0
c30p150	2	0	0	0	0	0	0	0	0
c45p0	0	0	0	0	9	0	0	0	0
c45p180	0	0	0	0	3	0	0	0	0
c60n60	0	0	0	0	0	0	0	0	1
c60p0	0	0	0	0	0	0	0	0	3
c60p60	0	0	0	0	0	0	0	0	8

Table 68. Confusion Matrix for Chucksat, Case 4

Calculated Images	Input Images				
	d30p120	d45n6 0	d45n3 0	d45p120	d60p180
d30p120	12	0	0	0	0
d45n60	0	0	4	0	0
d45n30	0	0	8	0	0
d45p120	0	0	0	0	3
d60p180	0	0	0	0	9

Table 69. Confusion Matrix for DMSP, Case 4

Calculated Images	Input Images									
	o30n150	o30n60	o45n150	o45n90	o45n60	o45n30	o45p90	o45p150	o60n120	o60p60
o30n150	0	1	0	0	0	0	0	0	0	0
o30n60	0	8	0	0	0	0	0	0	0	0
o45n150	0	1	0	0	0	0	1	0	0	0
o45n90	0	0	0	0	0	0	2	0	0	0
o45n60	0	2	0	0	0	0	0	0	0	0
o45n30	0	0	0	0	0	0	0	0	3	0
o45p90	0	0	0	0	0	0	8	0	0	0
o45p150	0	0	0	0	0	0	1	0	0	0
o60n120	0	0	0	0	0	0	0	0	2	0
o60p60	0	0	0	0	0	0	0	0	6	0

Table 70. Confusion Matrix for OCNR, Case 4

Calculated Images	Input Images									
	c30n150	c30p30	c30p150	c45n150	c45p0	c45p180	c60n120	c60n60	c60p60	c60p150
c30n150	3	0	0	0	0	0	0	0	0	0
c30p30	7	0	0	0	0	0	0	0	0	0
c30p150	3	0	0	0	0	0	0	0	0	0
c45n150	0	0	0	0	1	0	0	0	0	0
c45p0	0	0	0	0	8	0	0	0	0	0
c45p180	0	0	0	0	3	0	0	0	0	0
c60n120	0	0	0	0	0	0	0	0	1	0
c60n60	0	0	0	0	0	0	0	0	5	0
c60p60	0	0	0	0	0	0	0	0	4	0
c60p150	0	0	0	0	0	0	0	0	2	0

Table 71. Confusion Matrix for Chucksat, Case 5

Calculated Images	Input Images				
	d30p120	d45n60	d45n30	d45p120	d60p180
d30p120	12	0	0	0	1
d45n60	0	0	4	0	0
d45n30	0	0	8	0	0
d45p120	0	0	0	0	2
d60p180	0	0	0	0	9

Table 72. Confusion Matrix for DMSP, Case 5

Calculated Images	Input Images			
	o30n60	o45n150	o45n90	o45p90
o30n60	1	0	0	0
o45n150	11	0	0	1
o45n90	0	0	0	8
o45p90	0	0	0	3

Table 73. Confusion Matrix for OCNR, Case 5

Bibliography

1. *Adaptive Optics Tutorial, Adaptive Optics Associates, Inc Homepage* http://www.aoainc.com/AOS/AOtutorial.html

2. Air Force Maui Optical Station historical data provided by Mr Jack Albetski, Thermo Trex Corporation, Kihei, Maui, HI, (808)874-1641.

3. *Air Force Maui Optical Station Homepage* http://ulua.mhpcc.af.mil

4. *Applied Optics Group, Imperial College Homepage* http://op.ph.ic.ac.uk

5. R. R. Bate, D. D. Mueller, and J. E. White, *Fundamentals of Astrodynamics* Dover Publications, New York, 1971.

6. C. Y. Chang and R. Hoepner *Sensor Fusion in a Dynamic Model-Based System, Status Report* Texas Instruments Incorporated Defense Systems & Electronics Group, Plano, TX, July 1995.

7. D. Cyganski R. F. Vaz and C. R. Wright *Model Based 3-D Object Pose Estimation From Linear Image Decomposition and Direction of Arrival Analysis* SPIE Vol 1827, Model Based Vision, Boston, 1992.

8. *Documentation for Simulation Programs: OTFSIM3 and HYSIM3*, Air Force Institute of Technology.

9. J. D. Gaskill *Linear Systems, Fourier Transforms, and Optics* John Wiley and Sons, New York, 1978.

10. D. M. Gavrila and L. S. Davis *Fast Correlation Matching in Large (Edge) Image Databases* Computer Vision Laboratory Center for Automation Research, University of Maryland, August 1994.

11. J. W. Goodman, *Introduction to Fourier Optics*, McGraw-Hill, New York, NY 1996.

12. R. J. Qian and T. S. Huang *Optimal Edge Detection in Two Dimensional Images* IEEE Transactions on Image Processing, vol 5, no 7, July 1996.

13. W. J. Larson and J. R. Wertz, *Space Mission Analysis and Design, 2nd Edition* Microcosm, Inc., Ca, 1992.

14. T. Law, H. Itoh, and H. Seki, *Image Filtering, Edge Detection, and Edge Tracing Using Fuzzy Reasoning* IEEE Transactions on Pattern Analysis and Machine INtelligence, vol 18, no 5, May 1996.

15. D. J. Lee *Objective Image Quality Metrics: Applications for Partially Compensated Images of Space Objects* Master's Thesis, Air Force Institute of Technology, 1993.

16. Capt. Scott R. Maethner *Deconvolution from Wavefront Sensing Using Optimal Wavefront Estimators*, Masters Thesis, Air Force Institute of Technology, 1996.

17. *Mathcad User's Guide, Mathcad PLUS 6.0* Mathsoft, Inc., Cambridge, MA, 1995.

18. D. Mendenhall, R. L. Scheaffer, and D. d. Wackerly *Mathematical Statistics with Applications, 4th Edition* Duxbury Press, Belmont, CA, 1990.

19. H. Murase and S. K. Nayer *Visual Learning and Recognition of 3-D Objects from Appearance* International Journal of Computer Vision, vol 14, number 1, January 1995.

20. W. K. Pratt *Digital Image Processing* 2nd edition, John Wiley & Sons, Inc., New York, 1991.

21. M. C. Roggemann and B. Welsh *Imaging Through Turbulence*, CRC Press, New York, NY 1996.

22. M. C. Roggemann *Optical Performance of Fully and Partially Compensated Adaptive Optics Systems Using Least Squares and Minimum Variance Phase Reconstructors* Computers and Electrical Engineering, Vol. 18, No. 6, pp. 451-466, 1992.

23. M. C. Roggemann *Course Notes, Physics 621* Course taught at AFIT, Winter Quarter, 1996.

24. M. C. Roggemann *Limited Degree of Freedom Adaptive Optics and Image Reconstruction* Applied Optics, Vol. 30, No. 29, 10 October 1991.

25. J. C. Russ, *The Image Processing Handbook*, CRC Press, New York, NY 1992.

26. C. M. Thompson and L. Shure, *Image Processing Toolbox for Use with MATLAB*, The MathWorks, Inc., Natick, MA, 1993.

27. J. E. Treleaven *Human Visual System Enhancement of Reconstructed Satellite Images* Master's thesis, Air Force Institute of Technology, 1993.

28. R. Warner *Presentation made by Richard Warner, CEO of Aero Astro Corporation, at AFIT* 18 July 1996.

Vita

Lieutenant Gregory E. Wood ███████████████████████████████████. He graduated from Beavercreek High School in Beavercreek, Ohio in 1988. Wood then attended Purdue University in West Lafayette, Indiana where he received a B.S. in Aeronautical and Astronautical Engineering with a Major in Propulsion and a Minor in Aerodynamics. Upon graduation, he accepted a commission as a Second Lieutenant in the United States Air Force. In June, 1993, Wood was assigned to the 319 Air Refueling Wing, Grand Forks Air Force Base, North Dakota. While serving as an Emergency Actions Officer, he acted as the focal point for the command and control functions for 150 Minuteman III missiles and four squadrons of KC-135 aircraft as the wing transitioned from B-1B's. In May, 1995, he was assigned to the Air Force Institute of Technology, Wright-Patterson Air Force Base, Ohio to pursue a Master of Science degree in Space Operations. Upon completion of that assignment, Lieutenant Wood will be assigned as a Delta II Launch Control Officer at the 1st Space Launch Squadron, Cape Canaveral AFS, Florida.

REPORT DOCUMENTATION PAGE

1. AGENCY USE ONLY (Leave blank)	2. REPORT DATE	3. REPORT TYPE AND DATES COVERED
	November 1996	Master's Thesis

4. TITLE AND SUBTITLE

Estimation of Satellite Orientation From Space Surveillance Imagery Measured With an Adaptive Optics Telescope

5. FUNDING NUMBERS

6. AUTHOR(S)

Gregory E. Wood, 1Lt, USAF

7. PERFORMING ORGANIZATION NAME(S) AND ADDRESS(ES)

Air Force Institute of Technology, WPAFB OH 45433-6583

8. PERFORMING ORGANIZATION REPORT NUMBER

AFIT/GSO/ENP/96D-02

9. SPONSORING/MONITORING AGENCY NAME(S) AND ADDRESS(ES)

Capt Bruce Stribling
PL/OLYY Kihei, Maui, HI 96753

10. SPONSORING/MONITORING AGENCY REPORT NUMBER

11. SUPPLEMENTARY NOTES

12a. DISTRIBUTION/AVAILABILITY STATEMENT

Approved for public release; distribution unlimited

12b. DISTRIBUTION CODE

13. ABSTRACT *(Maximum 200 words)*

The use of the matched filter to automatically estimate the pose of a Low Earth Orbiting satellite from imagery measured with an adaptive optics telescope is explored. This work represents the first effort to solve the satellite pose estimation problem while considering the broad range of atmospheric turbulence levels and target visual magnitudes that are encountered in ground based space surveillance operations. Several algorithms are examined to determine the performance bounds on the matched filter for this application. Results are given over a wide range of seeing conditions and are weighted based on historical data obtained from the Air Force Maui Optical Station to show that, under normal conditions, the matched filter can be expected to yield correct pose estimations in over eighty percent of the cases considered. Additionally, it is shown that a substantial portion of incorrect pose estimations are due to symmetry in the target. A dependable algorithm is defined that will function effectively over a broad range of operational conditions.

14. SUBJECT TERMS

satellite pose, atmospheric turbulence, matched filter, space surveillance, adaptive optics

15. NUMBER OF PAGES

127

16. PRICE CODE

17. SECURITY CLASSIFICATION OF REPORT	18. SECURITY CLASSIFICATION OF THIS PAGE	19. SECURITY CLASSIFICATION OF ABSTRACT	20. LIMITATION OF ABSTRACT
UNCLASSIFIED	UNCLASSIFIED	UNCLASSIFIED	UL